Unsteady aerodynamics in the gust and manoeuvre response of flexible aircraft

Thesis report

D. Westerveld

Technische Universiteit Delft

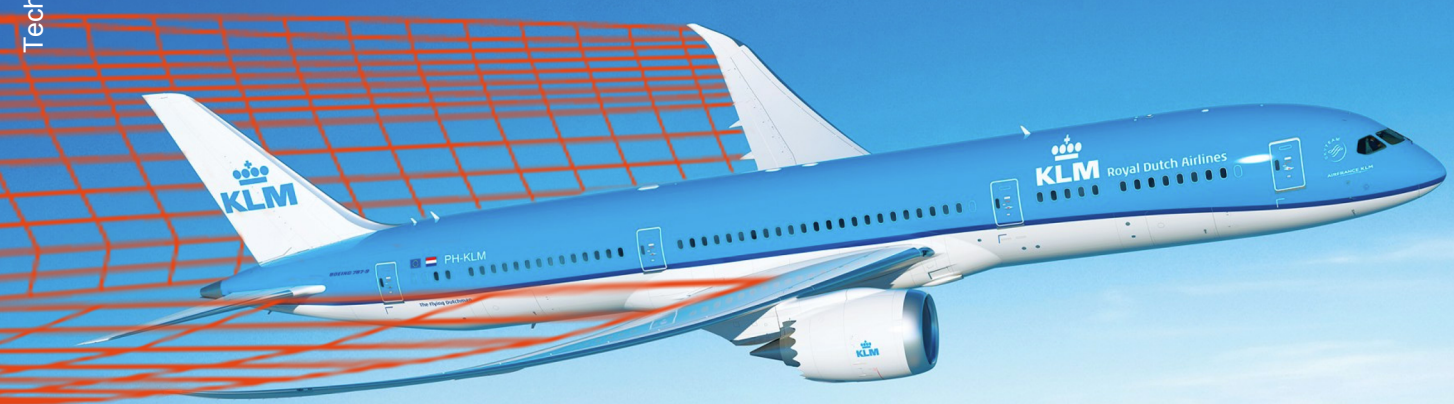

TU Delft

Unsteady aerodynamics in the gust and manoeuvre response of flexible aircraft

Thesis report

by

D. Westerveld

to obtain the degree of Master of Science
at the Delft University of Technology,
to be defended publicly on 7 October 2016, at 13:00.

Student number:	41060332	
Project duration:	September 4, 2015 – October 7, 2016	
Thesis registration number:	089#16#MT#FPP	
Thesis word count:	36706	
Thesis committee:	Prof. dr. ir. L. L. M. Veldhuis,	TU Delft, chairman
	Dr. ir. M. Voskuijl,	TU Delft, supervisor
	Dr. A. Elham,	TU Delft, supervisor
	Dr.-ing. R. Schmehl	TU Delft, external committee member

TU Delft

Summary

In the strive for ever decreasing fuel consumption, aircraft wings have become more slender and, in turn, more flexible. This brings with it a change in aircraft handling qualities, and it can have an effect on the structural design of the wing. It also brings the possibility of harnessing this structural flexibility for beneficial effects like load alleviation control. For optimal results this structural flexibility needs to be taken into account from the start of the aircraft design, which calls for an aeroelastic design framework. In this work part of such a design framework is constructed. The objective of this study is an investigation into the effect of unsteady aerodynamics on the gust response of flexible aircraft. This is realised by implementing an unsteady aerodynamic model, a gust model and a coupling of these models to an aeroelastic flight mechanics tool.

First, the aerodynamic model used as a comparison to the developed unsteady aerodynamic model was discussed. This is a quasi-steady aerodynamic model, based on Theodorsen's work under consideration of zero frequency motion. This model is included in the flight mechanics tool. Next to this, the adaption of the gust model existing in the aeroelastic flight mechanics toolbox was discussed. This adapted gust model is based on the $1 - \cos$ gust model defined in regulations and is able to model gusts in space, meaning that a time-delay effect can be modelled. This time-delay effect implies that the front of the aircraft sees the gust at an earlier time than the rear of the aircraft. With this gust model, the simulation cases used in this work were defined. These cases were defined for a typical short-haul passenger aircraft, flying at cruise altitude. The used gusts ranged from 10 to 200 meters in length. The simulations were performed with the developed unsteady aerodynamic model, and the quasi-steady aerodynamic model as reference.

The unsteady aerodynamic model developed for this work is the unsteady vortex lattice method. This potential flow method allows for modelling time-varying aerodynamics around lifting surfaces, including the movement of the wake behind this lifting surface. The model has been implemented as a MATLAB program, and is verified to work correctly for wings with sweep angles smaller than $30°$. A slight offset in the aerodynamic center is predicted by the model, as well as an underprediction of induced drag. The lift was found to be predicted correctly, including its time-dependent behaviour.

The aerodynamic model has been coupled to a flight mechanics tool, that can simulate flexible aircraft. This flight mechanics tool works by means of a rigid aircraft specifying the flight mechanics motion, and a mode shape representation of the aircraft wings that specify the flexible wing bending and movement. The coupling required some coordinate transformations to make both models consistent with each other. These transformations were shown to be implemented correctly. Next to this, the trim algorithm included in the flight mechanics tool has been adapted to work with the new aerodynamic model. This adaption has been performed by including a trim objective on the unsteady aerodynamics, in the form of the change of bound vortex strength over time. Next to this, the original trim algorithm has been extended by means of a longitudinal autopilot trim function that can fly the aircraft to a steady state.

Several results have been generated in this work. First of all, the original and adapted gust model were compared. It was found that the gust time-delay effect can have a profound effect on the aircraft gust behaviour, especially for short (high frequency) gusts. It was found that the overall load peaks on the aircraft increase in duration, due to being engulfed in the gust for a longer time. Moreover, it was seen that there is a tendency of the aircraft to pitch up at first, once only the front of the aircraft hits the gust. Secondly, the results of trim with both aerodynamic models were compared. It was found that the unsteady aerodynamic model requires less thrust for trimmed flight, and about 10 degrees less elevator deflection. This is attributed to an underprediction of pitching moment in the unsteady aerodynamic model. After this, the gust response simulation have been carried out. The results of these simulations showed a phase shift in the response of the aircraft modelled with unsteady aerodynamics. This is due to the modelling of the time-history of the flow with unsteady aerodynamics. While the overall reactions of the aircraft with unsteady aerodynamics were found to be slower, the aircraft reacted

earlier to a gust. This is due to the gust model that, in combination with the unsteady aerodynamic model, takes into account the total wing geometry. No differences in behaviour other than the phase shift were found between the two aerodynamic models. What was found is larger forces predicted by the unsteady aerodynamic model. Due to uncertainty in the modelling capability of the unsteady aerodynamic model no conclusion could be drawn whether this stemmed from the actual unsteady behaviour, or just a difference in force modelling. Finally, the aircraft behaviour after an elevator impulse has been simulated. This proves that manoeuvre loads can also be simulated with the current work. The elevator impulse simulation showed that the unsteady aerodynamics led to an increase of 18% in the period of the short period motion. This is due to the delay between angle of attack and force change in unsteady aerodynamics.

Overall, it is concluded that the influence of unsteady aerodynamics in the gust response of flexible aircraft is not significant. The relative differences between the models were small. Together with the fact that the computation time of the unsteady aerodynamic model is much larger than the quasi-steady model, it is concluded that unsteady aerodynamics should not be used for modelling the gust response of conventional flexible aircraft. However, results have indicated that unsteady aerodynamics can lead to a response difference for flexible wings, compared to rigid wings. Finally, while not performed in this work, the current model allows for simulating the aircraft in longitudinal and lateral motions with wings of variable structural flexibility. This allows for control law design and modelling with unsteady aerodynamics as a potential application.

Contents

Preface

This report marks the end of my time as a student at Delft University of Technology after six years. During this time I've learned a lot about engineering, aircraft, spacecraft and myself. I'll always look back fondly on my time in Delft.

I first want to thank my supervisors, Mark Voskuijl and Ali Elham. Mark, this is the second time you've been my supervisor and again it was very helpful to have you as supervisor. Thanks for motivating me, and setting me on track after every meeting. Ali, in the original goal of this thesis there was a part dedicated to flutter and optimisation. This part I've dropped over the course of the thesis as it was a bit too much to chew, but I'd like to thank you for sticking with me even after dropping most of your topic. Finally, I would like to thank Leo Veldhuis for being the chair of my committee, and Roland Schmehl for accepting to be my external committee member.

I will also like to thank the people in Kamertje 1. You've made the work over the past year a lot more enjoyable. It was very nice to always have someone to discuss results with, to help people with their work, to have coffee breaks, and drinks during the weekends. The lunch is something I'm going to miss most. Jelle, thanks for proofreading this report!

Finally, these years in Delft would not be possible if it was not for my parents. Thanks for supporting me during all these years. If it wasn't for you, I would not be where I am today.

Daan Westerveld
21 September 2016

Nomenclature

Symbols

Symbol	Description	Units
a	Distance from mid-chord to elastic axis	[m]
a	Aerodynamic influence coefficient	[m/s]
$\mathbf{a}$	Acceleration	[m/s^2]
A	Axial force	[N]
$\bar{A}$	RMS turbulence velocity	[m/s]
AR	Aspect ratio	[-]
b	Span	[m]
b	Semichord	[m]
c	Chord	[m]
$\mathbf{c}$	Control vector	[-]
C	Theodorsen function	[-]
C_{d_i}	Induced drag coefficient (two-dimensional)	[-]
C_{D_i}	Induced drag coefficient	[-]
C_l	Lift coefficient (two-dimensional)	[-]
C_L	Lift coefficient	[-]
C_m	Pitching moment coefficient (two-dimensional)	[-]
C_M	Pitching moment coefficient	[-]
dt	Timestep	[s]
$d\mathbf{l}$	Length of vortex segment	[m]
D	Drag force	[N]
D_i	Induced drag force	[N]
e	Spanwise efficiency factor	[-]
$\mathcal{E}$	Frame of reference	[-]
F_g	Flight load alleviation factor	[-]
$\mathbf{F}$	Force	[N]
$\mathbf{g}$	Grid coordinates	[m]
h	Altitude	[m]
h	Plunge distance	[m]
H	Distance to reach gust peak velocity	[m]
H	Frequency response function	[-]
i	Counter	[-]
i	Incidence angle	[rad]
$\bar{i}$	Wing twist angle	[rad]
j	Chordwise counter	[-]
J	Jacobian matrix	[-]
k	Reduced frequency	[-]
K	Gain	[-]
L	Lift force	[N]
m	Mass	[kg]

M	Mach number	[-]
M	Moment	[Nm]
n_c	Number of chordwise panels	[-]
n_s	Number of spanwise panels	[-]
n_p	Number of panels	[-]
n	Load factor	[-]
$\mathbf{n}$	Normal vector	[-]
N	Normal force	[N]
$\mathbf{o}$	Objective vector	[-]
p	Pressure	[Pa]
p	Roll rate	[rad/s]
P	Limit load	[rad/s]
$\mathbf{q}$	Induced velocity	[m/s]
$\mathbf{q}$	Modal coordinates	[-]
q	Dynamic pressure	[Pa]
q	Pitch rate	[rad/s]
r	Yaw rate	[rad/s]
$\mathbf{r}$	Distance to collocation point	[m]
s	Gust penetration distance	[m]
$\mathbf{s}$	Structural coordinates	[m]
S	Wing area	[m^2]
t	Time	[s]
T	Thrust	[N]
u	Velocity in x direction	[m/s]
$\bar{u}$	Structural deflection	[m]
U_σ	Limit turbulence intensity	[m/s]
v	Velocity in y direction	[m/s]
$\mathbf{V}$	Velocity	[m/s]
w	Velocity in z direction	[m/s]
W	Weight	[N]
W_g	Gust velocity	[m/s]
x	Horizontal distance	[m]
$\mathbf{x}$	Position vector	[m]
y	Sidewards distance	[m]
z	Vertical distance	[m]
Z_{mo}	Maximum operating altitude	[m]

Greek symbols

Symbol	Description	Units
α	Angle of attack	[rad]
β	Prandtl-Glauert correction factor	[-]
β	Sideslip angle	[rad]
δ	Control deflection	[deg]
ϵ	Convergence criterion	[-]
γ	Flightpath angle	[rad]
Γ	Vortex strength	[m^2/s]
η	Fraction of semispan	[-]

θ	Pitch angle	[rad]
λ	Taper ratio	[-]
Λ	Wing sweep	[deg]
ξ	Vorticity	[1/s]
ξ	Aeroelastic twist	[rad]
ρ	Density	[kg/m^3]
τ	Non-dimensional time	[-]
ϕ	Roll angle	[rad]
Φ	Potential function	[m^2/s]
Φ	Wagner function	[-]
ψ	Yaw angle	[rad]
ψ	Küssner function	[-]
ω	Frequency	[rad/s]
Ω	Aircraft orientation matrix	[-]

Subscripts

Symbol	Description
$[\cdot]_a$	Aileron
$[\cdot]_{ac}$	Aircraft
$[\cdot]_{cg}$	Center of gravity
$[\cdot]_{c/4}$	Quarter-chord
$[\cdot]_{ds}$	Design
$[\cdot]_{des}$	Desired
$[\cdot]_e$	Elevator
$[\cdot]_{eff}$	Effective
$[\cdot]_{err}$	Error
$[\cdot]_{ext}$	External
$[\cdot]_G$	Global
$[\cdot]_{loc}$	Local
$[\cdot]_{LE}$	Leading edge
$[\cdot]_{meas}$	Measured
$[\cdot]_{MLW}$	Maximum landing weight
$[\cdot]_{MTO}$	Maximum take-off weight
$[\cdot]_p$	Number of panels
$[\cdot]_r$	Rudder
$[\cdot]_{rw}$	Rigid wing
$[\cdot]_T$	Thrust
$[\cdot]_w$	Wake
$[\cdot]_{wing}$	Wing
$[\cdot]_{ZW}$	Zero-fuel
$[\cdot]_\infty$	Free-stream conditions
$[\cdot]_{\gamma-q}$	Flightpath to pitchrate

List of Figures

List of Tables

1

Introduction and background

Aeroelasticity is older than flight itself. A few days before the Wright brothers' first flight, Samuel Langley tried to become the first man to fly a powered airplane. This attempt resulted in structural failure of the aircraft (see Figure 1.1), which is attributed to torsional divergence. Nine days later the Wright brothers' successful flight used aeroelastic effects to control their aircraft [1].

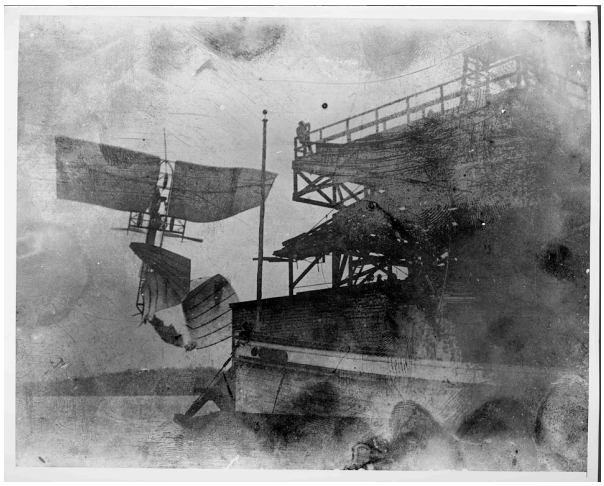

Figure 1.1: Samual Langley's aircraft crashing in the Potomac river. Courtesy of the Smithsonian Institution.

Today aeroelasticity still is a crucial part of aircraft design. In the effort of designing more fuel efficient aircraft there has been a trend towards structurally more flexible aircraft, as seen in Figure 1.2. This is due to increased aspect ratio, new (directional) materials and structural optimisation [2–4]. In turn, this can lead to less separation between the structural and flight dynamics frequencies [5], which can significantly alter the handling qualities of the aircraft [6]. Moreover, such flexible wings might open up possibilities for load alleviation control law design, which can lead to significant drag savings [7].

Not only do aeroelastic effects affect the handling qualities of the aircraft, it also results in a weight increase. This is due to the requirement of avoiding flutter and divergence [8]. Since this structural flexibility has a significant effect on the aircraft, it is important to consider this in the early stages of the design process. This can increase the reliability of this process [2, 9].

For this reason it is desired to have a design framework capable of modelling aircraft taking into account aeroelasticity. At Delft University of Technology, work is ongoing to incorporate conventional flexible aircraft in a preliminary design tool. A schematic of the envisioned framework is shown in Figure 1.3. Using such an integrated approach can lead to more effective aircraft designs, as results indicate that large weight savings (-10% fuel burn) might be achieved when using such a design framework [10].

(a) Boeing 767 (CC-BY Hussein Abdallah) (b) Boeing 787

Figure 1.2: Wing flex during take-off for an older (a, first flight: 1981) and newer (b, first flight: 2009) aircraft.

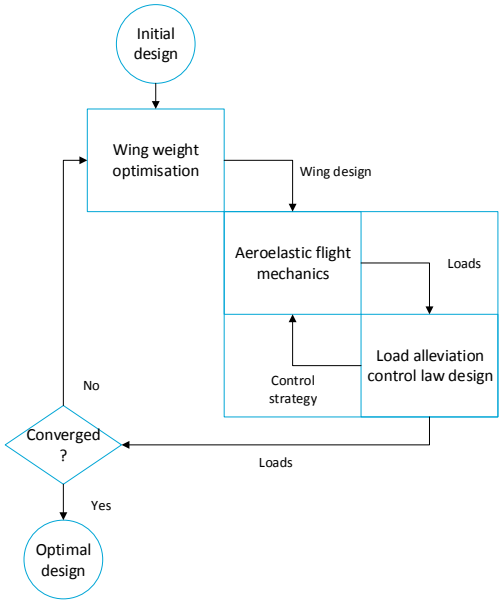

Figure 1.3: The envisioned aeroelastic design framework.

Currently existing in this tool are an aeroelastic wing weight estimation method [11], and an aeroelastic flight mechanics tool [12]. What is not included in these tools is an unsteady aerodynamic model. In order to accurately determine the aerodynamics in a situation where aeroelasticity is important, unsteady, or time-varying, aerodynamics is needed. This is because steady aerodynamic models cannot capture time-dependent effects which are encountered during rapid manoeuvring, after gusts or when flutter analysis is required [13–15]. The current work seeks to add to such a design process by implementing an unsteady aerodynamic model. This implementation is limited to the coupling between this aerodynamic model and the flight mechanics tool due to time constraints.

With such an aerodynamic model, it becomes possible to calculate the loads acting on the aircraft wing and, in conjunction with a flight dynamics model, it can be used to determine the aircraft response after a certain input (e.g. a gust). As gusts can be some of the critical load cases in aircraft design, it is important to be capable of modelling this load case [16]. It is because of this importance that gust response modelling is chosen as a case study for the work that is performed in this thesis.

A short introduction into the previously mentioned topics will be presented in the following sections, starting with unsteady aerodynamics in Section 1.1. This is followed by an introduction into flight mechanics and in particular aeroelastic flight mechanics, as explained in Section 1.2. With an aerodynamic

model and a flight mechanics model it is possible to predict the loads acting on an aircraft, which is the topic of Section 1.3. Once loads can be predicted, this knowledge can be used to alter these loads using control systems. With flexible aircraft, this is called aeroservoelasticity and is introduced in Section 1.4. Having the background knowledge, the objective of this thesis is discussed in Section 1.5, after which an outline of the report is given in Section 1.6.

1.1. Unsteady aerodynamics

Unsteady aerodynamics deal with time-varying aerodynamic phenomena. These phenomena are important when dealing with accelerating surfaces and air, which is the case in deflecting wings, gusts or turbulence fields. The work on unsteady aerodynamics started in the beginning of the 20th century. In 1925, Wagner studied the growth of wake vorticity and lift of an airfoil subject to a sudden acceleration [17], resulting in the Wagner function $\Phi(\tau)$, with $\tau = t\frac{2V}{c}$ the non-dimensional time. This is one of the classical analytical equations in the field of unsteady aerodynamics. Two other important equations are due to Küssner and Theodorsen. Küssner's function $\psi(\tau)$ describes the lift of an airfoil flying into a sharp-edged gust [18]. Theodorsen described the lift on an airfoil in oscillating motion, resulting in the Theodorsen function $C(k)$ [19]. This description is purely a function of the reduced frequency k, a non-dimensionalised frequency parameter ($k = \frac{\omega c}{2V}$). The reduced frequency is an important parameter in unsteady aerodynamics, as it determines the unsteadiness of the flow. If $k > \mathcal{O}(0.01)$ the flow needs to be modelled as unsteady for accurate results [20].

For conceptual and preliminary design purposes, the Wagner, Theodorsen and Küssner functions are still in use [21]. However, due to the increasing computational power there is a shift towards numerical methods. For unsteady aerodynamics this is done using strip theory [22], mostly using the theory of Peters et al. [23, 24]. While strip theory is a computationally efficient method, it has a disadvantage in that it does not predict three-dimensional effects such as wing tip vortices correctly [25].

Potential flow methods such as the Doublet Lattice Method (DLM) [26] and the Unsteady Vortex Lattice Method (UVLM) [16] are also in use. The DLM is the de-facto standard, and is posed in the frequency domain, and assumes a flat wake trailing the lifting surface. It is also limited to small deflections of the lifting surface. This method is the industry standard for modelling unsteady aerodynamics in preliminary design [21, 22]. The UVLM is posed in time domain, and in contrast with the DLM it allows for the wake to convect with the local velocity. Moreover, the UVLM is capable of modelling lifting surfaces with large deflections. The UVLM has seen use in biological aerodynamics (e.g. [27, 28]), and it is increasingly used in aircraft aerodynamics as well [21, 29, 30].

Next to potential methods, also full scale Computational Fluid Dynamics (CFD) methods have been used in unsteady aerodynamics [31, 32]. While these methods can accurately predict unsteady aerodynamics around arbitrary surfaces, it is still too time-consuming for the preliminary design stages. Therefore these methods are given no further attention in the current work. The attention in work is focussed on potential methods, which do not include viscous effects. While these can be important for high frequency motion, the computational time associated with modelling viscosity it too high for the preliminary design phase.

1.2. Flight mechanics

Flight mechanics, as the name implies, deals with the mechanics of flight. This is a very broad subject, as it can include almost all aspects of the aircraft such as aerodynamics, propulsion, structures etc. With information on these aspects (i.e. the aircraft design), one is able to evaluate the flight mechanics of the aircraft.

This is performed using equations of motion, which describe the motion of the aircraft due to the forces acting upon it. Depending on the case of interest, these equations can be simple (such as straight, level flight where $L = W$ and $T = D$), to complicated (e.g. thrust under an angle, accelerating flight). No matter how complicated, the equations of motion are always an expression of Newton's second law $\mathbf{F} = m\mathbf{a}$.

In the current work the scope is limited to the flight dynamics of the aircraft, meaning the rotations of the aircraft and its movement with respect to the ground. This is done with the aircraft being excited by external forces such as a gust or control input. To solve for flight dynamics, equations of the moments around the aircraft center of gravity are required, while Newton's second law is used to determine the overall flightpath of the aircraft.

In general there are six equations of motion required to calculate the mechanics of the aircraft. As an aircraft can translate and rotate about each of its three axes, there are six degrees of freedom. In setting up these equations of motion, it is convenient to define multiple reference frames as some forces or velocities are defined in specific reference frames [33]. For this reason it is customary to define different reference frames in flight mechanics calculations. The most often used reference frames are described in the following [34]:

- **Earth fixed frame** The Earth fixed frame is, in most flight mechanics application, the inertial frame (assuming a non-rotating, flat Earth). This frame is used to specify the aircraft position with respect to the ground. It thus defines the flightpath of the aircraft. It is a right-handed system with the z-axis positive downwards.
- **Vehicle carried Earth frame** This frame is a frame parallel to the Earth fixed frame, but translates with the aircraft itself. It is attached to the aircraft center of gravity. In this way one can express the orientation of the aircraft, in terms of pitch, roll and yaw. Again, the z-axis is positive downwards.
- **Body frame** The body axis system is attached to the aircraft center of gravity, with the x-axis pointing out of the nose of the aircraft. The y-axis points out of the right wing, implying a downward z-axis.
- **Airpath frame** This frame is again attached to the aircraft center of gravity, with the x-axis pointing in the direction of the velocity vector $\mathbf{V}$. This is the frame in which the aerodynamic forces will be defined.

In general the aircraft flight mechanics are calculated for rigid aircraft. However, with aircraft becoming more structurally flexible, research is being done into flight mechanics of flexible aircraft. This is called aeroelastic flight mechanics, and is explored in more detail in Subsection 1.2.1.

1.2.1. Aeroelastic flight mechanics

As the increasing structural flexibility of newer aircraft affects the handling qualities, the design of control systems may become more complex [6]. Moreover, current aircraft like the Airbus A320 and A330 are using load alleviation control systems [7]. Care has to be taken with the design of such systems as a coupling between a structurally flexible wing and control systems can have a negative impact of both handling qualities and loads acting on the wing [5]. This indicates that an integrated approach of aeroelasticity, flight mechanics and control systems is needed in the preliminary design stages. In other words, the movement of the aircraft structure needs to be taken into account in setting up the equations of motion.

This fact has been recognised for some time, but a lack of computational power prevented any integrated approach from existing [35]. In the 1960s Milne [36] presented an analytical treatment of aeroelastic flight mechanics, making use of the so-called mean axes assumption. This assumption makes the linear and angular momenta of the relative motion of the aircraft with respect to the body-axis zero at each moment in time. In this way the rigid and elastic motion of the aircraft are effectively decoupled.

Further work in this field resulted in two modelling approaches; the unified model and the coupling of specialised solvers for the different disciplines. In the unified approach the flight mechanics equations of motion are augmented with elastic motion, both with and without interpolation between structures and aerodynamics [6, 37, 38]. In these unified models, generally unsteady aerodynamics are used in the form of strip theory [38], the UVLM [39], or a vortex lattice method with an empirical lag state [40]. Other researchers derived unified models from first principles using Lagrange's method [41]. These methods are derived using the mean-axes assumption, but it has been stated by Meirovitch and Tuzcu [35] that most researchers that use this mean-axes assumption do not enforce the constraints needed for this approach (Cavagna et al. later pointed out that rigid and deformable modes were still coupled through

aerodynamics, meaning that the mean-axes assumption is too limiting [31].). For this reason Meirovitch and Tuzcu derived a unified model with a reference frame attached to the undeformed aircraft, making it not use the mean-axes assumption.

The other approach; coupling specialised solvers can be, among others, used with multi-body dynamics [31, 42]. A disadvantage of these models is that they can be very time-consuming and thus not suitable for the preliminary design stage. A remedy for this is using low(er)-fidelity tools in such a multi-body dynamics system, which is what has been done at Delft University of Technology [12]. This model can describe the aircraft flight mechanics for aircraft with flexible wings, while also flight dynamics parameters such as short periods and control effectiveness can be modelled. At present, this model includes quasi-steady aerodynamics in the form of strip theory. This leaves room for improvement when one wants to model very flexible aircraft, or rapid manoeuvring [13]. It can therefore be identified that an unsteady aerodynamic model that is compatible with this multi-body formulation is needed.

1.3. Load prediction

For proper design of control systems and wing structure, the design framework should be capable of accurately predicting the loads on the aircraft. Naturally, these loads stem from the aerodynamic model but the structural loads are ultimately of interest, such as root bending moment and shear force. A way to show the largest forces encountered during the lifespan of an aircraft is to use a flight envelope. This is further discussed in Subsection 1.3.1. Next to the manoeuvring loads shown in the flight envelope, loads can also occur from turbulence. In this work there is focussed on a particular form; gusts. This is elaborated upon in Subsection 1.3.2.

Finally, apart from these flight loads, also ground loads are of interest such as landing impact. In this case the aerodynamics are of less importance, and a further look into these loads is thus not done in the current writing. It should be noted that these loads can be simulated well using multibody dynamics.

1.3.1. Flight envelope

Before a discussion on the flight envelope can be held, the aircraft load factor needs to be explained. The load factor is defined as $n = L/W$ (for small angles of attack). In steady horizontal flight $n = 1$, but during manoeuvres the load factor can increase or decrease. It is a measure for the amount of load (and its direction) an aircraft encounters. The maximum permissible load factors can be shown in a V-n diagram, also called the manoeuvre flight envelope. An example of such a diagram is shown in Figure 1.4. In this diagram the combinations of aircraft speed and load factor that an aircraft needs to be designed for is shown. The flight envelope shows static loading, and is only shown for completeness' sake.

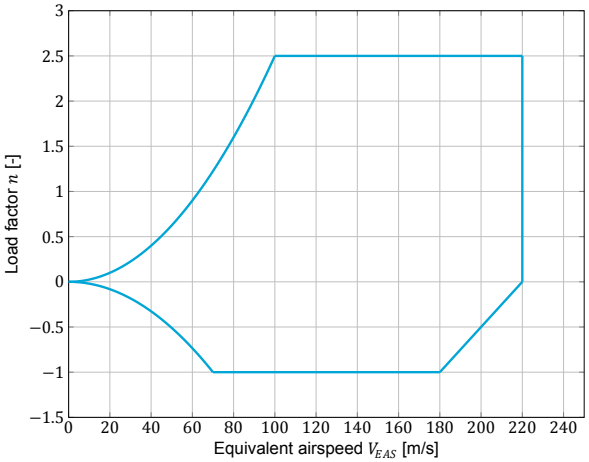

Figure 1.4: A generic manoeuvre flight envelope.

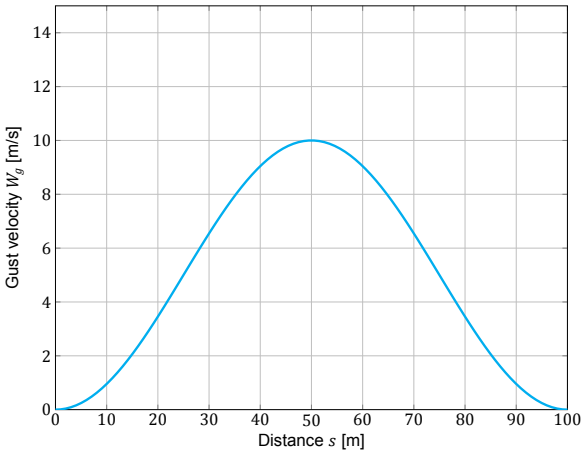

Figure 1.5: $1 - \cos$ gust shape.

This diagram is constructed based on regulations, such as those in [43]. These regulations specify the corners points of the diagram, which in turn are the critical cases. It is for these critical cases that the aircraft needs to be designed. In this diagram, gust loads can also be plotted.

1.3.2. Gusts and turbulence

While some critical load cases can be determined using the manoeuvre flight envelope, not all are captured. A very important set of of loads encountered during the aircraft life-time are loads due to turbulence. Turbulence can be defined as '*movement of the air, through which the aircraft passes*' [15]. The vertical portion of this movement changes the effective angle of attack of the aircraft and, in turn, changes the loads acting upon the aircraft. For strong gusts, these loads may change drastically.

The importance of correctly taking into account turbulence has been shown in history. A well-known example of this is the NASA Helios, as shown in Figure 1.6. The NASA Helios was a solar-powered high-altitude, long-endurance aircraft with very flexible wings. An encounter with atmospheric turbulence led to '*the aircraft becoming unstable in a very divergent pitch mode*' which '*caused the wing leading edge secondary structure on the outer wing panels to fail and the solar cells and skin on the upper surface of the wing to rip off*' [44].

(a) Before (b) After

Figure 1.6: The NASA Helios before (a) and after (b) encountering a gust. Images courtesy of NASA.

If one wants design an aircraft capable of withstanding such gusts, one needs to be able to model the loads generated by a gust. In literature two distinct categories are used to model gusts; discrete and continuous gusts [15].

Discrete gusts

Discrete gusts are normally modelled using the so-called $1-\cos$ gust, defined in regulations by Equation 1.1 [43].

$$W_g = \begin{cases} \frac{W_{g_{ds}}}{2}\left(1-\cos\frac{\pi s}{H}\right) & 0 \leq s \leq 2H \\ 0 & s > 2H \end{cases} \tag{1.1}$$

Here $W_{g_{ds}}$ is the design gust velocity, s the distance penetrated into the gust and H the distance for the gust to reach peak velocity. Values of H between 9 m and 107 m need to be taken into account. The $1-\cos$ gust is shown in Figure 1.5. From this shape it is seen that the different parts of the aircraft will see a different gust velocity.

From the gust shape it is seen that the time behaviour of the gust on the aircraft needs to be taken into account. This time behaviour implies that time-varying aerodynamics are needed to model the gust behaviour (and, in fact, required by regulations [43]). However, for long enough gust distances H, the wing root bending moment magnitude is sufficiently captured by quasi-steady or even steady

aerodynamics [13]. What is lacking in this research is a handle on when exactly unsteady aerodynamics will be necessary to model the aircraft response after discrete gusts. Fidkowski et al. [45] show the effect of unsteady aerodynamics on the bending loads due to gusts, from which it is again seen that unsteady aerodynamics start to matter at shorter gust distances. The unsteady aerodynamics in this case were modelled using an empirical lag state. It was found that for gusts with $H > 30$ ft a quasi-steady aerodynamic assumption is valid. However, this was performed using a Boeing 737-400 like aircraft, which has less flexible wings compared to modern aircraft. It thus remains to be seen if this handle on gust distance still holds.

Continuous gusts

Next to discrete gusts, a continuous gust can be taken into account. While not considered further in this work, it is discussed for completeness. Whereas discrete gusts are modelled in the time-domain, continuous gusts are generally modelled in the frequency domain using power spectral density (PSD) techniques [15]. Two PSD functions used for atmospheric turbulence are due to Dryden and Von Kármán [46].

From regulations one assumes the direction of the continuous gust to be one-dimensional, and acting normal to the aircraft direction of travel [43]. This must be done for both lateral and longitudinal gusts. The limit load acting on the aircraft can be defined by [43]:

$$P_L = P_{L-1g} \pm U_\sigma \bar{A} \tag{1.2}$$

In this equation P_L is the limit load on the aircraft, with P_{L-1g} the limit load at a steady 1-g condition. The second term in the equation models the load due to continuous gusts and consists of U_σ, being the limit turbulence intensity in true airspeed and $\bar{A}$ the root-mean-square turbulence velocity. $\bar{A}$ is determined using the PSD functions $\Phi_l(\Omega)$, coupled to a frequency response function $H(\Omega)$ that maps the turbulence loads to aircraft structural loads. Mathematically this can be expressed as:

$$\bar{A} = \sqrt{\int_0^\infty |H(\Omega)|^2 \Phi_l(\Omega)\, d\Omega} \tag{1.3}$$

1.4. Aeroservoelasticity

Aeroservoelasticity is the coupling between aeroelasticity and the control system. This coupling can lead to unwanted interactions, such as controllers that induce poorly damped structural modes [47]. The coupling can also be harnessed for beneficial effects such as active flutter suppression or load alleviation [48].

As the name implies, load alleviation is a system that uses control surfaces to reduce the load acting on a wing during manoeuvres and gusts. Not only can this help in structural optimisation, also the passenger comfort can be increased. These systems typically require sensors to measure the load acting on the aircraft, and need actuators capable of reacting to the used control laws. Moreover, active load alleviation systems are subject to certification [43, K25.1]

In general, a distinction is made between manoeuvre load alleviation (MLA) and gust load alleviation (GLA). The MLA responds to manoeuvres initiated by the pilot. It will use the control surfaces to concentrate the lift more inboard and thus reduce the wing root bending moment during manoeuvres [10]. This reduced bending moment allows for a lighter wing design. This brings with it another problem, and that is the fact that gust loads might become critical due to this lighter wing. Therefore, to realise the full benefits of MLA it should be coupled with GLA [10].

In order to properly design such load alleviation systems it is important to take aircraft flexibility into account, as shown by Fidkowski et al. [45]. The same study indicated that unsteady aerodynamics might not be necessary in gust response, but other authors state otherwise [13]. It is therefore of

interest to see whether unsteady aerodynamics are necessary or not for these control systems. This however is left for future work, due to time constraints.

While the benefits of load alleviation systems have been known for quite some time and have been applied to existing aircraft, such systems have scarcely been used in conceptual design tools. Xu [7] worked on a method incorporating MLA and GLA with a physics-based approach in a conceptual design optimisation tool, but did not include unsteady aerodynamics. Haghighat et al. [49] performed optimisations including active load alleviation systems, but also did not take into account unsteady aerodynamics. Nam et al. [50] did include unsteady aerodynamics, but restricted themselves to optimisation for GLA and flutter suppression.

Of course, these control systems must be designed such that the unwanted interactions do not take place. Moreover, the handling qualities of the aircraft, defined as 'those qualities or characteristics of an aircraft that govern the ease and precision with which a pilot is able to perform the tasks required in support of an aircraft role' [51], must remain to acceptable standards. From this, and the work performed previously there is a gap for a complete design optimisation methodology taking into account aeroservoelasticity, handling qualities and other aeroelastic phenomena (e.g. flutter, wing jig shape etc.). The current work aims to add to the modelling capabilities present at the TU Delft, such that in the future such optimisations might become possible.

1.5. Thesis objective

From the background information it is found that there is a need for an aeroelastic aircraft design framework capable of modelling and optimising the wing structure, flight mechanics and control laws. An important part of such a framework is unsteady aerodynamic modelling. The current work aims to add the capability of modelling unsteady aerodynamics to such a design framework. Because of time constraints the focus will be on the coupling between the aerodynamic model and the flight mechanics parts of the design framework. This aerodynamic modelling will be performed with a time-domain method, as the flight mechanics toolbox is specified in time-domain as well making this directly compatible. As a case study for this coupling the gust response of flexible aircraft is investigated using these tools.

The aerodynamic model will be constructed using the unsteady vortex lattice method as explained in Chapter 3. With this choice of aerodynamic model a research objective can be defined for this work, keeping in mind that it should work with the envisioned design framework for conventional aircraft (requiring it to have a low computational time). The objective is defined as follows:

Develop a fast and accurate aerodynamic model for subsonic, conventional aircraft capable of modelling unsteady aerodynamic forces and moments in an aeroelastic flight mechanics environment, by means of the unsteady vortex lattice method.

To realise this objective, several sub-objectives are defined. If each of these sub-objectives is met, the main objective of the work will also be achieved. The sub-objectives are defined as follows:

- *Develop a fast and accurate unsteady aerodynamic model by means of the unsteady vortex lattice method.*
- *Couple the aerodynamic model with the aeroelastic flight mechanics toolbox.*

Once this objective has been met, the work can be used for research. In the current work this research will be performed on the gust response of flexible aircraft. Because of this, another objective must be met. This objective has to do with a gust model, and is defined as:

- *Develop a discrete gust model that can model a gust acting on staggered parts of the aircraft at a different time, by means of a* $1 - \cos$ *gust model.*

Achieving this objective will make it possible to investigate the effect of gusts on aircraft. To quantify the effect, several research questions are posed which are to be answered:

- What is the difference between unsteady and quasi-steady aerodynamics on the gust response of a structurally flexible aircraft?

- Do the loads differ in magnitude?
- Do the maxima in loads occur at different times?
- At what gust length do unsteady aerodynamic effects become relevant?

In the end, this information should give insight into when unsteady aerodynamics becomes necessary when modelling the flight mechanics of structurally flexible aircraft.

1.6. Thesis outline

Now it is clear what this thesis entails, it is possible to set up the structure of the thesis report. First the simulation cases will be explained in Chapter 2. In this chapter also the aerodynamic model to which the unsteady aerodynamic model will be compared is explained, and an overview of the used gust model is given. With the simulation cases defined, the necessary tools are identified. First, an unsteady aerodynamic model is required. This will be explained, verified and validated in Chapter 3. This unsteady aerodynamic model needs to be coupled with an aeroelastic flight mechanics toolbox. The details on this coupling are discussed in Chapter 4. With all tools present, simulations can performed. The results of thse simulations are shown and analysed in Chapter 5. Finally, Chapter 6 will conclude the report and give recommendations on future work.

2

Simulation cases

Before a discussion on the conducted work is presented, the test cases that will be used to answer the research question are defined in this chapter. Doing this gives a clear overview on what is needed to answer this question. However, before the test cases are discussed a short introduction into two other topics is given.

As alluded to in Chapter 1, an unsteady aerodynamic model will be constructed in this work. To compare results made with this model, a quasi-steady aerodynamic model will be used as a baseline. This model is currently implemented in the aeroelastic flight mechanics toolbox (called PHALANX) present at TU Delft, and will be discussed in Section 2.1. Also included in this toolbox is a discrete gust model. This discrete gust model will be adapted and changed to be better suited for the current work. The model, and its adaption are explained in Section 2.2.

With this the cases used for simulation can be defined. This includes defining an aircraft, its flight condition and gust properties. These are all discussed in Section 2.3. Finally, Section 2.4 will summarise the chapter, and show how the information in this chapter will be used for the subsequent chapters.

2.1. Quasi-steady aerodynamics

As a comparison to the unsteady aerodynamics, a quasi-steady (QS) aerodynamic model present in the flight mechanics toolbox will be used. The QS model is based on Theodorsen's work [19], which describes the lift of an airfoil in oscillating motion. For this, Theodorsen developed the Theodorsen function $C(k)$. This function models changes in phase and amplitude resulting from the oscillating motion [15]. In essence, the Theodorsen function is the Fourier transform of the Wagner function $\Phi(\tau)$.

The lift of an oscillating airfoil, as described by Theodorsen is shown in Equation 2.1.

$$L = \pi\rho b^2 \left[\ddot{h} + V\dot{\xi} - ba\ddot{\xi}\right] + 2\pi\rho VbC(k)\left[\dot{h} + Vb\left(\tfrac{1}{2} - a\right)\xi\dot{\xi}\right] \tag{2.1}$$

In this equation b is the semichord $c/2$, and a is the distance between the mid-chord and the elastic axis in terms of semi-chord. ξ is the aeroelastic twist deflection (or local angle of attack) and h the plunging distance. Equation 2.1 consists of two terms. The first term describes the non-circulatory lift, meaning the forces generated by movement of the lifting surface. This occurs since a mass of air is accelerated by the lifting surface as it moves, creating a reaction force on the airfoil [15]. The second term in the equation relates to circulatory forces, which are forces generated by vorticity in the flow. In this term $C(k)$ is used to make lift a function of frequency, such that it becomes an unsteady aerodynamic force.

To make this model quasi-steady, the assumption of zero frequency k is made. This results in a Theodorsen function of $C(0) = 1$. This quasi-steady model is used in the form of a look-up table of

the aerodynamic coefficients in terms of angle of attack. To follow Theodorsen's theory, the so-called effective angle of attack α_{eff} will be used. This effective angle of attack needs to be measured at the three-quarter chord point [67]. The effective angle of attack can be calculated by using the second term in brackets in Equation 2.1, as the first bracketed term contains acceleration effects ($\dot{h}$ and $\ddot{\xi}$) that have a small influence on the results [12]. Noting that $\dot{\xi}$ results in a plunging motion at the three-quarter chord point ($\dot{h}_{\dot{\xi}}$), one can write down the effective angle of attack as:

$$\alpha_{eff} = \arctan\left(\frac{\dot{h} + \dot{h}_{\dot{\xi}}}{u}\right) + \alpha_{rw} \tag{2.2}$$

$\dot{h}_{\dot{\xi}}$ can be written as $b\left(\frac{1}{2} - a\right)\cos\xi\dot{\xi}$ (recognise the resemblance to Equation 2.1) [12], and knowing that α can be calculated from the rigid wing velocity, the final effective angle of attack calculation can be written as:

$$\alpha_{eff} = \arctan\left(\frac{w_{rw}}{u_{rw}}\right) + \xi + \arctan\left(\frac{b\left(\frac{1}{2} - a\right)\cos\xi\dot{\xi}}{u_{rw}}\right) \tag{2.3}$$

Here w_{rw} and u_{rw} are the rigid wing z and x velocities respectively. The second term in this equation accounts for the change in angle of attack if a wing section rotates. The final term includes the effect of the movement itself.

As seen from Equation 2.3 there is no time-history included in the model, but there is a dependency on the wing movement. This is what makes the model quasi-steady. Moreover, this model is a strip model meaning that only two-dimensional effects are modelled. Therefore, no tip vortices can be modelled with this type of aerodynamic theory.

2.2. Gust analysis

If one wants to see the effect of a gust on the loads acting on an aircraft, a gust model is needed. While shortly explained in Section 1.3, this section will provide some more information on the model used (Subsection 2.2.1), and the implementation of the model (Subsection 2.2.2).

2.2.1. Gust model

The gust model used in this work is that the model specified by the European Aviation Safety Agency (EASA) [43]. This gust is a discrete gust and is modelled using a cosine term. It is described by Equation 1.1, repeated here for clarity:

$$W_g = \begin{cases} \frac{W_{g_{ds}}}{2}\left(1 - \cos\frac{\pi s}{H}\right) & 0 \leq s \leq 2H \\ 0 & s > 2H \end{cases} \tag{2.4}$$

The design gust velocity $W_{g_{ds}}$ is defined as:

$$W_{g_{ds}} = W_{ref} F_g \left(\frac{H}{350}\right)^{1/6} \tag{2.5}$$

Here W_{ref} is the reference gust velocity, which depends on the aircraft flight speed and on the altitude. At sea-level this is 56 ft/s Equivalent Airspeed (EAS), both positive and negative, and can be decreased with increasing altitude as shown in Figure 2.1. F_g is the flight load alleviation factor which is dependent on the aircraft weight and its maximum operating altitude, and is defined as:

$$F_g = \frac{1}{2}\left(F_{gz} + F_{gm}\right) \tag{2.6}$$

$$F_{gz} = 1 - \frac{Z_{mo}}{76200} \tag{2.7}$$

$$F_{gm} = \sqrt{\frac{W_{ZF}}{W_{MTO}} \tan\left(\frac{\pi}{4}\frac{W_{MLW}}{W_{MTO}}\right)} \tag{2.8}$$

Where Z_{mo} is the maximum operating altitude in meters, W_{ZW} the maximum zero fuel weight, W_{MTO} the maximum take-off weight and W_{MLW} the maximum landing weight.

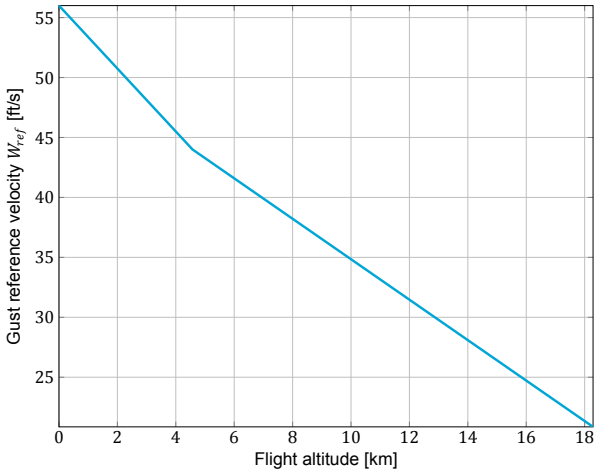

Figure 2.1: The gust reference velocity W_{ref} as a function of altitude h, if the aircraft velocity lies between V_B and V_C. At the dive velocity V_D the gust reference speed is half of the shown value. This is the absolute velocity and in simulation should be taken both as positive and negative [43].

According to the regulations [43] the gust penetration distance H needs to be taken between 30 ft and 350 ft, with sufficient steps in between. This means that to quantify the total gust loads acting on an aircraft a large amount of gust simulations need to be performed. This is because the gust velocity (i.e., its strength) is dependent on the gust length. Moreover, the frequency of the gust itself might play a role in the aircraft response, especially in the case of flexible wings.

2.2.2. Gust implementation

Since this work relates to unsteady, or time-varying responses of aircraft to gusts it is imperative to model the gust in such a way that it takes time for its effect to reach each part of the aircraft. For example, when flying into a gust the wings will be affected earlier than the horizontal tail. This is not yet present in the flight mechanics toolbox, as it models gusts without this time delay effect. This means that all parts staggered on the aircraft receive the same gust velocity, regardless of their actual position with the $1 - \cos$ gust shape. Any flight dynamics effects that stem from having different gust velocities acting on different parts of the aircraft at the same time cannot be modelled.

This so-called time delay effect has been performed in literature, for example in [68]. To include this time delay effect in this work, the gust is implemented as a gust field in space at a certain gust start location $(x, y, z)_{gs}$. The gust has a length of $2H$, as well as a certain height in order to limit the influence of the gust on the wake movement. At each timestep in the simulation, the coordinates of all aircraft parts that are subject to the gust (being the wing, empennage, fuselage and the wake) are passed to the gust function (Equation 2.4). Using the difference between the location of the aircraft parts and the gust starting position, the gust penetration distance s can be calculated for a part i using $s_i = x_i - x_{gs}$. This directly leads to a gust velocity as the gust velocity W_g is related to s through Equation 2.4.

There is a difference in this implementation for the quasi-steady aerodynamic model versus the unsteady aerodynamic model. Naturally, the quasi-steady model does not include a wake so no effect of the gust on the wake deformation can be calculated in the quasi-steady model. Another difference is the manner in which the wing is modelled. The quasi-steady aerodynamic model solves for a complete wing section, so the gust velocity instantaneously acts on the entire section. With the unsteady aerodynamic implementation (UVLM), the wing is modelled with several chordwise sections such that also the travel time of the gust over the wing itself is taken into account.

An illustration of this implementation is shown in Figure 2.2. This shows the gust velocity versus time of the leading edge at the root, the trailing edge at the root (having $c_r = 5$ [m]), and the horizontal tail (modelled as a point). The tail is positioned 30 m behind the wing root leading edge. The aircraft is flying at a hypothetical speed of 20 m/s, while the gust semilength is set to $H = 70$ [m].

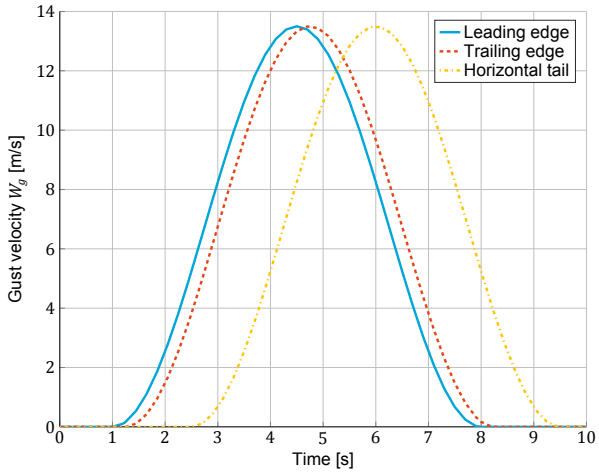

Figure 2.2: Gust velocity versus time for different positions on the aircraft. Shown are the wing root leading edge, wing root trailing edge and the horizontal tail. The trailing edge is positioned 5 m behind the leading edge, while the tail is position 30 m behind the leading edge. The gust semilength is $H = 70$ m, and the aircraft is flying at a hypothetical speed of 20 m/s.

The effects on the aircraft dynamics due to this time-delay effect are shown in Chapter 5.

2.3. Simulation cases

Now that all the tools required to answer the research question are present, it is time to establish the simulation cases that will be used to answer said question. First of all, an aircraft needs to be chosen. This is done in Subsection 2.3.1. Secondly the flight parameters such as altitude and flight speed need to be decided upon. This can be found in Subsection 2.3.2. Finally a choice of several gust profiles is to be made, which will be done in Subsection 2.3.3. The combination of these are summarised, while also the chosen output will be explained. This is performed in Subsection 2.3.4. Note that the unsteady aerodynamic model will be referred to as UVLM.

2.3.1. Aircraft choice

The aircraft that is chosen to be simulated is modelled after an Airbus A320, which is a typical short-to-medium haul aircraft. While comparable, it is not the same as the actual A320 as this model is missing the wing kink. However, the data on this wing was available to the author and has thus been chosen as simulation model. The data from this wing comes from Kalthof [12] and the main parameters are presented here for clarity. For more information the reader is referred to [12].

The control surfaces of the aircraft are modelled using the pre-existing method (i.e., based on aerodynamic coefficient look-up tables, see Chapter 4) there is some data associated with these as well. This aerodynamic data is generated by DATCOM [55]. In this, it is assumed that the tail surfaces have a NACA 0009 airfoil. The aerodynamic data stemming from DATCOM is also used for the wing in the

UVLM. It is used to define the maximum sectional coefficients of the wing (C_l, C_d and C_m) in order to limit the UVLM results. Because the UVLM is a potential flow method, it cannot model non-linear effects such as stall and thus the maximum coefficients need to be bounded. The limits are shown in Table 2.1, and in DATCOM occur at an angle of attack $\alpha = 22°$. Moreover, lower limits on these values are also included. The minimum value of C_d is C_{d_0} and is also appended to the induced drag calculation in the UVLM, such that also zero-lift drag is used to predict the drag force.

The structural data for this aircraft, being the mode shapes, is constructed using a finite-elements analysis with NASTRAN. This data can be found in [12]. To summarise, Table 2.1 shows the main wing parameters, while Figure 2.3 presents a top view of this wing.

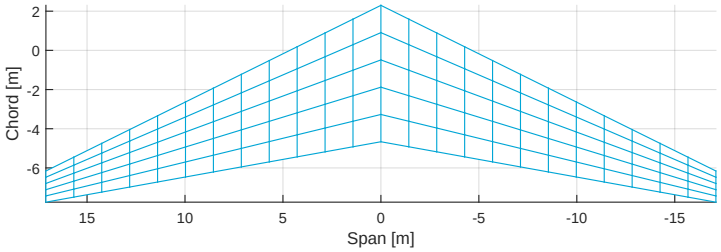

Figure 2.3: Top view of the A320-like wing.

Table 2.1: Main parameters of the Airbus A320-like wing. Taken from [12].

Parameter	Value	Unit	Parameter	Value	Unit
Semispan $b/2$	17.1	[m]	Wing incidence angle i	6	[deg]
Root chord c_r	7	[m]	Wing twist angle ϵ	2	[deg]
Taper ratio λ	0.229	[-]	Location of e.a.	0.33	[% of chord]
Leading-edge sweep Λ_{LE}	25	[deg]	Location of a.c.	0.253	[% of chord]
Dihedral angle Γ	5.1	[deg]	Location of c.g.	0.43	[% of chord]
Maximum C_l	1.725	[-]	Minimum C_l	-0.792	[-]
Maximum C_m	0.2169	[-]	Minimum C_m	0,1356	[-]
Maximum C_d	0.26	[-]	Minimum C_d	0.014	[-]

2.3.2. Flight parameters

Gusts are most critical during the approach phase of the aircraft, due to the aircraft having a lighter wing (more fuel burned) and stronger gust velocities. However, due to structural data available to the author this work will look at an aircraft flying at cruise condition. Since only a comparison between different aerodynamic models is desired, this is acceptable.

As a typical passenger aircraft is considered, the chosen cruise altitude is $h_{cr} = 11$ km. For the flight velocity, it is chosen to use a velocity lower than the actual cruise velocity of an A320. This is because the UVLM does not have transonic capabilities, other than a Prandtl-Glauert correction. To stay within the model limits, the chosen speed is therefore $V_\infty = 150$ m/s, or around $M = 0.5$ at this cruise altitude.

The aircraft is filled with maximum fuel as this is the data available to the author. This means that each wing carries 9313 kg of fuel. No flaps are deflected for the simulation, and naturally the landing gear is retracted.

2.3.3. Gust profiles

In choosing the gust profiles that are to be considered one parameter can be altered; the gust semi-length H. For H it is chosen to use the bounds as set by regulations, while adding a gust distance of $H = 5$ meters (16.4 ft) in order to have a gust profile where unsteady aerodynamics are expected to be important for correct results. In total 5 gust profiles will be used, as shown in Table 2.3.

The two other variables for the gust profile (F_g and W_{ref}) are fixed by the choice of aircraft and the flight parameters respectively. Since the aircraft under consideration will fly at a cruise altitude of 11 km, the gust reference velocity will be $W_{ref} = 10.106$ m/s (following [43]).

To determine F_g information on the weight and maximum operating altitude of the aircraft is required. As an Airbus A320-like wing is taken, these values will be taken from the Airbus A320-200 [69]. As the maximum operating altitude is not known for an Airbus A320-200, this will be taken as 3000 ft higher than the cruise altitude of 37000 ft.

Table 2.2: Weights of the Airbus A320-200, which are used for the A320-like aircraft under consideration. Data from [69].

Parameter	Value
Z_{mo} [km]	12.192
W_{ZF} [kg]	60500
W_{MLW} [kg]	64500
W_{MTO} [kg]	73500

This results in a load alleviation factor of $F_g = 0.8318$. Combining this with the gust reference velocity and the gust semi-distance H, results in the following design velocities of the gusts:

Table 2.3: Gust semi-distance and corresponding gust design velocity.

Parameter	Value				
H [m]	5	30.4	55.9	81.3	106.7
$W_{g_{ds}}$ [m/s]	5.05	6.80	7.50	8.03	8.40

2.3.4. Output from the cases

In summary, the chosen simulation cases are combined in Table 2.4. Naturally, these cases will be run for each aircraft (i.e., rigid and flexible wings) and aerodynamic model.

Table 2.4: The chosen gust profiles.

Case	1	2	3	4	5
Gust semi-distance H [m]	5	30.4	55.9	81.3	106.7
Flight speed V_∞ [m/s]	150	150	150	150	150
Altitude h [km]	11	11	11	11	11

From these cases it is desired to know the output as a function of time as shown in Table 2.5. Using these values it is possible to analyse the forces acting on the aircraft (using the moments and load factor) and the aircraft response after encountering a gust (using its flight dynamics properties of translation and angular velocity). Next, the overall flight path parameters of altitude and flight velocity provide information on the overall aircraft response. Finally, the wing tip movement is used to compare the effect of the different aerodynamic models on the wing deflection.

It should be noted that in the present work there will only be looked at the longitudinal response. As the gust profiles used will be symmetric, the aircraft response expected to be only in the longitudinal

Table 2.5: The desired output of the simulations. All variables will be a function of time t.

Variable	Name
M_{wr}	Wing root bending moment [Nm]
d_{wt}	Wing tip deflection [m]
n	Load factor [-]
u	Velocity in x-direction [m/s]
w	Velocity in z-direction [m/s]
θ	Pitch angle [deg]
q	Pitch rate [deg/s]
h	Altitude [m]
V	Flight speed [m/s]

plane. Under this assumption fewer degrees of freedom of the aircraft have to be modelled, saving computational time. The degrees of freedom will only be the longitudinal velocity u, the vertical velocity w and the aircraft pitch angle θ. Naturally, with a flexible wing the modal velocities of the wing are added as degrees of freedom.

2.4. Summary

This chapter served as a further introduction to the report. First, the theory behind the existing aerodynamic model of the flight mechanics toolbox was explained. This aerodynamic model will be used as a comparison to the unsteady aerodynamic model discussed in Chapter 3. Secondly, the gust model that will be used to simulate the gust response was explained. This gust model is an adaption of the gust model existing in the flight mechanics toolbox, and adds a time-delay effect in the modelling. This means that different parts of the aircraft see different gust velocities, depending on their position in the $1 - \cos$ gust shape. This gust model works with both the existing aerodynamic model, and the unsteady aerodynamic model to be constructed in this work. The effects of this adaption are shown in Chapter 5.

Next, this chapter showed the simulation cases that will be used to model the gust response. These simulation cases are all for an Airbus A320-like wing, flying at cruise altitude. The simulations will be performed for 5 different gust lengths, and will be done with a rigid and a flexible wing. Moreover, both the original quasi-steady aerodynamic model of the flight mechanics toolbox and the unsteady aerodynamic model of this work are used to simulate the gust response. This allows for a proper comparison between steady and unsteady aerodynamics. The results of these simulations are shown in Chapter 5.

Finally, from this chapter it can be shown what is still required in order to get to a point where simulations can be performed. First, an unsteady aerodynamic model needs to be constructed. This model then needs to be connected to the aeroelastic flight mechanics toolbox, such that aircraft flight mechanics can be taken into account. This is the topic of the next chapters.

3

Aerodynamic model

As mentioned in the introduction, unsteady aerodynamics deals with time-varying aerodynamic phenomena. In order to analyse these time-varying phenomena an unsteady aerodynamic model is required. An important part of such an unsteady aerodynamic model is the influence of the wake on the wing. The wake is the air trailing the lifting surface, and it can have a complex structure, such as the one seen in Figure 3.1.

Figure 3.1: A Kármán vortex street behind a circular cylinder. This shows the complex wake structures that can occur in aerodynamic flow, which is an important consideration in unsteady aerodynamics [52].

Because of the preliminary design nature of the tools to be used, potential flow theory will be used to model the aerodynamics. Potential flow is further explained in Section 3.1. Several potential flow methods exist, but only one will be used in this work, which is the unsteady vortex lattice method (UVLM). The theory behind this model is explained in Section 3.2. The implementation of this model is verified and validated in Section 3.3. Finally, this chapter is summarised and concluded in Section 3.4.

3.1. Potential flow

Potential flow is a very useful flow type for rapid aerodynamic calculations. This section describes the theory behind potential flow, after which some of its limitation are discussed. Finally, a choice of potential method to use in the current work is made.

3.1.1. Theory

In order to use potential flow, some assumptions have to be made [53]:

- Inviscid flow
- Irrotational flow, $\xi = 0$
- Incompressible flow, $\rho = \text{const}$

Using these assumptions, the continuity equation (Equation 3.1) can be simplified to Equation 3.2.

$$\frac{\partial \rho}{\partial t} + \nabla \cdot \rho \mathbf{V} = 0 \tag{3.1}$$

$$\nabla \cdot \mathbf{V} = 0 \tag{3.2}$$

Using the irrotational flow assumption, written mathematically as $\boldsymbol{\xi} = \nabla \times \mathbf{V} = 0$ and using the vector identity $\nabla \times (\nabla \Phi) = 0$ it follows that a scalar function can be defined such that:

$$\mathbf{V} = \nabla \Phi \tag{3.3}$$

Substituting Equation 3.3 into Equation 3.2 gives Laplace's equation:

$$\nabla^2 \Phi = 0 \tag{3.4}$$

This is a very important equation in physics [53] and makes for quick aerodynamic analysis. The flow field can be described completely using the velocity potential Φ. This reduces the equations required from three (all velocity components, because of incompressible flow) to only one, making it an efficient manner of describing a flowfield.

However, Equation 3.4 does not show any time-dependence which is necessary for unsteady aerodynamics. This time-dependence is introduced through the boundary conditions that are used when solving the equation. The first of these boundary conditions states that far away from the body, the velocity perturbations due to this body should vanish:

$$\lim_{x \to \infty} \mathbf{V} = \mathbf{V}_\infty \tag{3.5}$$

The basic solutions to Equation 3.4 (such as a doublet or vortex, see [54] for more information) all adhere to this boundary condition, as their strength decays with distance.

The second boundary condition deals with the shape of the object submerged in the flow. As air cannot move through a solid body, the flow velocity is tangent to this body at the body interface. Using the normal vector of the body $\mathbf{n}$, this boundary condition can be written as:

$$\mathbf{V} \cdot \mathbf{n} = 0 \tag{3.6}$$

The final boundary condition is the so-called Kutta-Joukowski condition, which states that the flow must leave the trailing edge of the body in a smooth manner. It will fix the flow to have its rear stagnation point at the trailing edge, which is how actual (viscous) flow behaves.

If Equation 3.4 is solved using these boundary conditions one can find the velocity components of the flowfield as well as the pressure. In an unsteady case this pressure can be calculated from the unsteady Bernoulli equation:

$$\frac{p_\infty - p}{\rho} = \frac{(\Delta \Phi)^2}{2} + \frac{\partial \Phi}{\partial t} \tag{3.7}$$

3.1.2. Limitations

Assuming incompressible flow means that the model is not valid for flow velocities larger than $M = 0.3$. However, this thesis deals with transonic passenger aircraft which fly outside of the incompressible regime. In order to mitigate this problem, the Prandtl-Glauert correction will be used which holds till $M < 0.7$. This correction is defined as:

$$\beta = \sqrt{1 - M_\infty^2} \tag{3.8}$$

Another limitation of potential theory stems from the assumption of inviscid flow. This implies that viscous drag is not modelled, but for accurate load prediction this is necessary. For this reason the induced drag calculation stemming from the potential flow method will be amended with an estimate of the viscous drag over the lifting surface. In this work this is added by means of a C_{D_0} increment found using DATCOM [55]. This can also be implemented using engineering methods such as those found in Roskam [56], or Torenbeek [57] such that the model itself can account for different shapes and geometries at runtime.

Next to this, there is a limitation on calculating the effect of the wake. In real life, the wake will dissipate and its influence over time decreases. While this can be modelled [27], it is not done in the current work. As the aircraft under consideration are flying relatively fast, it will quickly move away from previous wake points. Since the influence of the wake is based on the inverse of the distance to it, this will model dissipation in a sense. Due to computational efficiency, the wake will also be truncated for most applications (this is a user setting). The standard setting used in this work is 4 times the wing span, as literature indicates this to be sufficient [58, 59], while tests by the author showed the same. Due to the flight velocity of the aircraft under consideration, this is considered a reasonable assumption [60] but one should be aware of this lack of wake dissipation modelling.

3.1.3. Models

Several potential methods are in use to model unsteady aerodynamics. The two most used are the doublet lattice method (DLM) [26] and the unsteady vortex lattice method (UVLM) [54]. As mentioned in Section 1.1 the DLM is specified in frequency domain, whereas the UVLM is posed in time domain. Moreover, the UVLM does allow for a force-free wake, as well as arbitrary motion of the lifting surface and deflection of said surface [16].

Next to potential flow, it would be possible to use full-fledged CFD methods but these are too time-consuming in the conceptual design stages. Two-dimensional strip theory is also a possibility but this lacks the ability to accurately model three-dimensional effects such as tip vortices [21].

Summarising, it is chosen to use the UVLM for the unsteady aerodynamic model in this thesis for the following reasons:

- It is a potential flow method, making it suitable for conceptual design stage calculations in computational time.
- The UVLM is defined in time-domain, which makes it directly compatible with the aeroelastic flight mechanics toolbox as this is also posed in time-domain.
- The UVLM allows for large structural deflections and is not restricted to small out-of-plane motion, making it suitable for modelling very flexible aircraft.

3.2. Unsteady Vortex Lattice Method

The potential flow method used for this thesis is the Unsteady Vortex Lattice Method (UVLM). The implementation in this thesis follows the work of Katz and Plotkin [54], Murua [16], and Stanford and Beran [29]. A flowchart of the steps explained in the following sections can be found in Figure A.1.

In this method a lifting surface is discretised using vortex rings (see Figure 3.2); a rectilinear element consisting of four constant strength vortex segments. These vortex rings are placed on n_c chordwise sections and n_s spanwise sections, making for a total number of sections of $n_p = n_c n_s$. Each of the

vortex rings is shifted in chordwise direction by 25% of the local chord. This is to ensure that the two-dimensional Kutta condition is satisfied [54]. In the middle of each of these vortex rings a collocation point is placed at which the non-penetrating boundary condition will be evaluated.

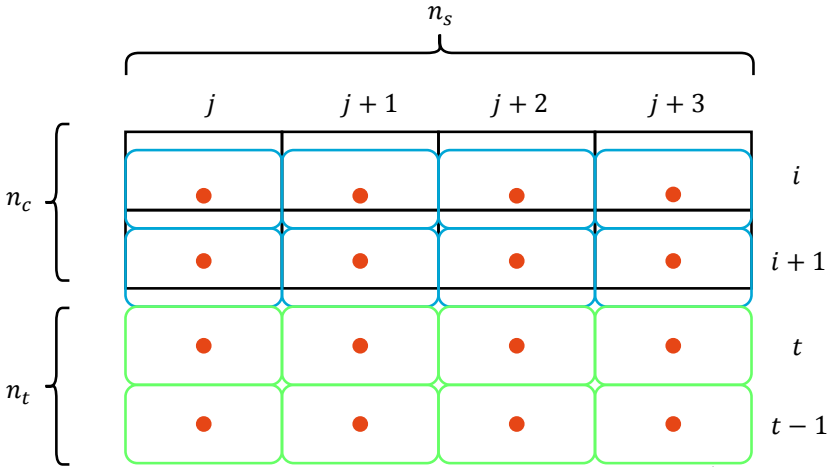

Figure 3.2: The used wing discretisation scheme, showing the wing sections (black, rectangular), vortex rings (blue, rounded), collocation points (orange, dots) and wake vortex rings (green, rounded and depicted by n_t).

Not only the lifting surface is discretised, but also the wake trailing it. The shape and movement of this wake is calculated in the UVLM based on the vortex strength in the flowfield. At each timestep t^n a set of n_s wake vortex rings is shed from the lifting surface, based on the position of the wing at timestep t^{n-1}, as also shown in Figure 3.2. The shed wake vortex rings acquire the vortex strength of the trailing edge vortex rings:

$$\Gamma_W^n = \Gamma_{TE}^{n-1} \tag{3.9}$$

In the subsequent timesteps the vortex strength of the already shed wake vortex rings stays constant, as per the Helmholtz theorem ($\mathrm{d}\Gamma/\mathrm{d}t = 0$).

3.2.1. Reference frames

Because the UVLM simulates a lifting surface flying in time-domain, following an arbitrary flightpath, the proper use of reference frames becomes important. For this work three different reference frames are used. First, there is the Earth attached inertial frame $\mathcal{E}_i$ in which the flightpath is specified. In this work the Earth is assumed flat, and non-rotating. Secondly, a body-carried Earth frame $\mathcal{E}_{Eb}$ is used, which moves locally with the lifting surface but has its orientation equal to $\mathcal{E}_i$. Finally there is the body frame $\mathcal{E}_b$ which shares its origin with $\mathcal{E}_{Eb}$, but is rotated with the body orientation Ω and the global (or rigid aircraft) angle of attack α_G as shown in Equation 3.10. The positioning and orientation of these frames relative to each other can be seen in Figure 3.3.

$$\mathcal{E}_b = \Omega[\alpha_G]_y \mathcal{E}_{Eb} \tag{3.10}$$

3.2.2. Calculation of the flowfield

In order to calculate the properties of the flowfield over the lifting surface, one needs to solve for the vortex strength present in this flowfield. The first step is to calculate the influence that each vortex ring has on the flowfield using the so-called Aerodynamic Influence Coefficients (AIC). This can be done by calculating the influence of each vortex segment in the vortex ring, on the collocation points.

Using the Biot-Savart law, as shown in Equation 3.11, one can calculate the influence that a vortex segment has on a certain point in space.

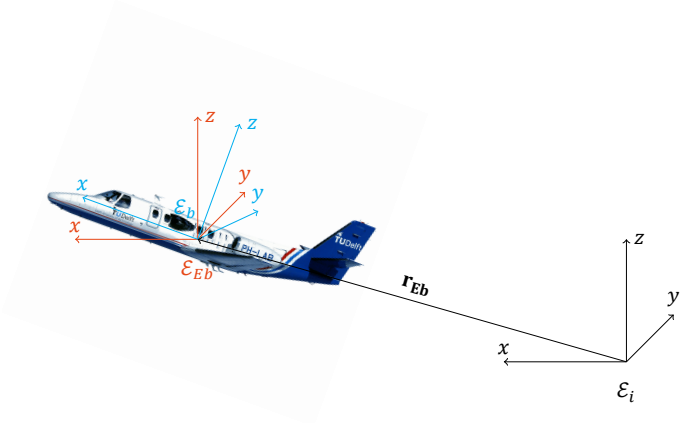

Figure 3.3: The positioning and orientation of the used frames of reference.

$$\mathbf{q} = \frac{\Gamma}{4\pi} \frac{d\mathbf{l} \times \mathbf{r}}{r^3} \tag{3.11}$$

If one has a vortex line pointing from A to B, one can rewrite Equation 3.11 to calculate the induced velocity at some point P as follows:

$$\mathbf{q}_{A,B} = \frac{\Gamma}{4\pi} \frac{\mathbf{r}_A \times \mathbf{r}_B}{|\mathbf{r}_A \times \mathbf{r}_B|^2} \mathbf{r}_{A-B} \cdot \left(\frac{\mathbf{r}_A}{r_A} - \frac{\mathbf{r}_B}{r_B} \right) \tag{3.12}$$

Here $\mathbf{r}_A$ is the vector from A to P, and $\mathbf{r}_B$ the vector from B to P. It should be noted that when P lies on the vortex segment, a singularity will occur [54]. This should be handled accordingly in the implementation, which in this work is performed by replacing any NaN results by 0. In MATLAB this method is easier to implement than to check beforehand whether a calculation is performed on a vortex line.

Since a vortex ring consists of four vortex segments, one has to apply Equation 3.12 four times to calculate the influence of one vortex ring. Performing this calculation for each vortex ring and each collocation point with $\Gamma = 1$, and multiplying with the normal vector n (expressed in the body frame $\mathcal{E}_b$) the aerodynamic influence of each ring is obtained, called $a_{i,j}$. Combining these in a matrix yields the AICs, where the counter n_p is the amount of collocation points and p the collocation point at point (i, j).

$$AIC = \begin{bmatrix} a_{1,1} & \dots & a_{1,n_p} \\ \vdots & \ddots & \vdots \\ a_{n_p,1} & \dots & a_{n_p,n_p} \end{bmatrix} \quad \text{with } a_{i,j} = \mathbf{q}_{i,j} \cdot \mathbf{n}_p \tag{3.13}$$

Now the influence of each vortex ring is known, but the actual vorticity strength is not known. To calculate this strength, one more piece of information is needed which comes from the non-penetrating boundary condition (Equation 3.6). From this it is known that there should be zero normal velocity on each collocation point. While the velocities due to the lifting surface vortex rings are not yet known (as the vorticity strength is still unknown), some velocities are already known. This is the flight velocity $\mathbf{V}_\infty$, the velocity due to the wake $\mathbf{V}_w$, the local deflection velocity of a panel $\mathbf{V}_{deflect}$ and any external velocities $\mathbf{V}_{ext}$ (such as gusts). This also needs to be multiplied with the normal vector of the vortex ring under consideration, such that the velocities point in the correct direction. In this work this is performed in the body frame $\mathcal{E}_b$. The boundary condition can be written in vector form, which will be useful in determining the vorticity strength of each panel:

$$RHS = \begin{bmatrix} -\left(\mathbf{V}_\infty + \mathbf{V}_w + \mathbf{V}_{deflect} + \mathbf{V}_{ext}\right)_1 \cdot \mathbf{n}_1 \\ \vdots \\ -\left(\mathbf{V}_\infty + \mathbf{V}_w + \mathbf{V}_{deflect} + \mathbf{V}_{ext}\right)_{n_p} \cdot \mathbf{n}_{n_p} \end{bmatrix} \tag{3.14}$$

Now that the influence of each ring is known, as well as the velocities acting upon each ring it becomes straightforward to determine the induced velocities that the rings should provide in order to have tangential flow at each ring:

$$\begin{bmatrix} a_{1,1} & \dots & a_{1,n_p} \\ \vdots & \ddots & \vdots \\ a_{n_p,1} & \dots & a_{n_p,n_p} \end{bmatrix} \begin{bmatrix} \Gamma_1 \\ \vdots \\ \Gamma_{n_p} \end{bmatrix} = \begin{bmatrix} -\left(\mathbf{V}_\infty + \mathbf{V}_w + \mathbf{V}_{deflect} + \mathbf{V}_{ext}\right)_1 \cdot \mathbf{n}_1 \\ \vdots \\ -\left(\mathbf{V}_\infty + \mathbf{V}_w + \mathbf{V}_{deflect} + \mathbf{V}_{ext}\right)_{n_p} \cdot \mathbf{n}_{n_p} \end{bmatrix} \tag{3.15}$$

Re-ordering this equation, and giving the matrices a symbol yields the following equation that needs to be solved:

$$\Gamma = AIC^{-1}RHS \tag{3.16}$$

Now that the vorticity of the lifting surface is known, the calculation of the wake influence can be performed. Subsequently, the information of the flowfield can be used to calculate the aerodynamic forces acting upon the lifting surface.

The wake

As mentioned, at each timestep the wake gets a row of new vortex rings, positioned at the previous position of the trailing edge of the lifting surface. Per the Helmholtz theorem this wake gets the vortex strength of the trailing edge panels at the previous timestep. Because of this, the induced velocity on the lifting surface from the wake can be calculated directly from Equation 3.11.

Next to an influence on the lifting surface, the wake has an influence on itself. Also the lifting surface has an influence on the wake. Both parts induce a velocity on the wake, causing it too move (e.g., tip vortices or a starting vortex). Again, using the Biot-Savart law (Equation 3.11) it is possible to calculate the induced velocity at the wake vortex ring corner points for both the influence of the wing on the wake (bw), and the influence of the wake on itself (ww). Also the effect of external disturbances can be added to these induced velocities:

$$\mathbf{V}_w = \mathbf{V}_{bw} + \mathbf{V}_{ww} + \mathbf{V}_{ext} \tag{3.17}$$

Together with the timestep dt, it is possible to update the position of the wake vortex ring corner points using a simple integration:

$$\mathbf{x}_w^{n+1} = \mathbf{x}_w^n + \mathbf{V}_w^n dt \tag{3.18}$$

This movement then changes the wake influence in the next timestep. One should keep in mind that the wake vortex ring corner points connecting to the trailing edge of the lifting surface are not moved with $\mathbf{V}_w$, in order to have the wake attach to the lifting surface. In this way there are no discontinuities between the lifting surface and its wake.

3.2.3. Calculation of the aerodynamic forces and moments

Following the calculation of the vorticity on the lifting surface, the forces and pitching moment can be calculated. This can be calculated from the unsteady Bernoulli equation, rewritten to yield the lift of each panel at a timestep [29]:

$$\Delta L_{i,j} = \rho \Delta b_{i,j} \left[\|\mathbf{V}_{i,j}\| \left(\Gamma_{i,j} - \Gamma_{i-1,j}\right) + \Delta c_{i,j} \frac{\partial}{\partial t} \left(\frac{\Gamma_{i,j} + \Gamma_{i-1,j}}{2} \right) \right] \cos \alpha_{i,j} \tag{3.19}$$

Here Δc and Δb are the chord- and spanwise lengths of each panel, $\mathbf{V}$ is the velocity of each panel and α is the local panel angle of attack. At the leading edge ($i = 1$), the $i - 1$ terms drop out as there are no panels in front of the leading edge. This lift acts along the local panel lift direction, and thus has to be transformed to the $\mathcal{E}_{eb}$ frame. This is performed by dividing the local lift force by $\cos\left(\alpha_{loc} - \alpha_G\right)_{i,j}$, with α_{loc} being the local panel angle of attack and α_G the global angle of attack.

If the induced drag is calculated from the pressure distribution (i.e. similarly to the lift), it will be overestimated due to the fact that the UVLM neglects the existence of leading-edge suction [54]. Therefore a different calculation is used, as shown in Equation 3.20. In this equation the induced velocities of only the streamwise vortex lines (i.e., those that are parallel to the x-axis) are used.

$$D_{i_{i,j}} = \rho \Delta b_{i,j} \left[\left(w_{ind} + w_{wake}\right)_{i,j} \left(\Gamma_{i,j} - \Gamma_{i-1,j}\right) + \frac{\partial \Gamma_{i,j}}{\partial t} \Delta c_{i,j} \sin \alpha_{i,j} \right] \tag{3.20}$$

In this equation w_{ind} and w_{wake} are the induced downwash stemming from the wing and the wake, respectively. Again, at the leading edge ($i = 1$), the $i - 1$ terms drop out. This induced drag term also acts along the local panel drag direction, and is converted to the global drag direction in the same manner as the lift.

Finally, from the lift and induced drag a pitching moment around a certain chordwise point can be calculated. This requires the normal (N) and tangential (A) force on each vortex ring to be known. These forces can be calculated from the local lift and induced drag forces by dividing these forces by $\cos \alpha_{loc}$. Together with the distance of the force attachment point to the pitching moment reference point (normally the aerodynamic center), one can calculate the moment using the following relation (where an upwards moment is assumed positive):

$$M_{i,j} = A_{i,j} z_{i,j} - N_{i,j} x_{i,j} \tag{3.21}$$

Here $x_{i,j}$ and $z_{i,j}$ are the distances between the force attachment point and the moment reference point. Based on literature, it is assumed that the forces are acting on the leading edge of the vortex ring [16]. This is because this yields agreement with analytical values.

These forces can be converted to their respective coefficients for the complete lifting surface by the following definitions:

$$C_L = \frac{\sum L_{i,j}}{\frac{1}{2}\rho V_\infty^2 S} \tag{3.22}$$

$$C_{D_i} = \frac{\sum D_{i_{i,j}}}{\frac{1}{2}\rho V_\infty^2 S} \tag{3.23}$$

$$C_M = \frac{\sum M_{i,j}}{\frac{1}{2}\rho V_\infty^2 S \bar{c}} \tag{3.24}$$

3.3. Verification and validation

In order to show that the UVLM works as intended, the model should be validated. The validation is performed using a set of validation functions and data.

As a first step, a grid convergence study is carried out. This should yield information on the minimum amount of grid points required to get a converged result. This is shown in Subsection 3.3.1. In Subsection 3.3.2 the computation time of the UVLM is analysed. After this, there will be looked at the steady-state behaviour of the model as shown in Subsection 3.3.3. Finally, the unsteady behaviour of the model will be verified and validated in Subsection 3.3.4.

3.3.1. Grid convergence

Figure 3.4 shows steady-state values of C_L and C_D plotted against combinations of different grid size (i.e., combinations of n_s and n_c). It is seen that there is not much effect of the number of chordwise panels on the value of C_L. The effect of the amount of spanwise panels on this parameter is much larger, as it is seen that around 20 spanwise panels gives a converged value for C_L (a converged value in this case means no more change in C_L with increasing grid size, and in this case is $C_L = 0.3882$). At 20 spanwise sections, the error in C_L is less than 1%, even with only 5 chordwise panels.

The induced drag coefficient shows a different trend, with it being more sensitive to the number of chordwise panels n_c. It is seen that with $n_s > 10$ only a change in n_c changes the results, with around 25 chordwise panels for a converged value of C_{D_i}. With $n_c = 10$, the error in C_{D_i} is 9.5%.

Based on these results it is chosen to use $n_s = 24$ and $n_c = 10$ panels for the simulations. Having $n_c = 10$ saves a large amount of computational time compared to a larger value (see also Subsection 3.3.2). These properties are deemed more important than a fully converged value for C_{D_i} as this is much smaller than C_L.

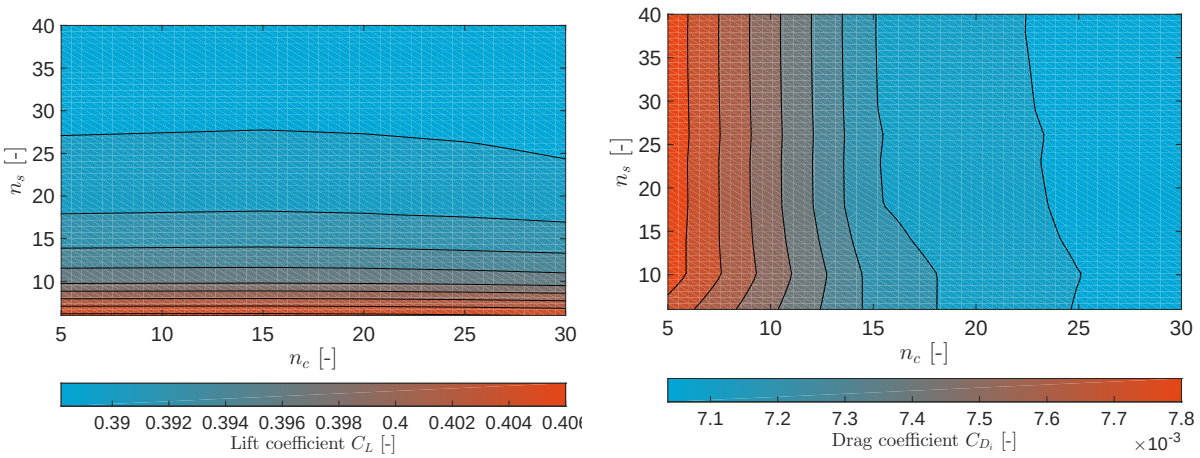

(a) C_L (b) C_{D_i}

Figure 3.4: The grid convergence of a planar, rectangular wing of $\mathcal{AR} = 7$. Two variables (C_L and C_{D_i}) are shown as a function of both n_c and n_s. Simulation time used is $t = 20$ [s], with $n_t = 40$.

3.3.2. Computation time

As the research objective is to make a rapid aerodynamic model, an analysis on the computation time needs to be performed. This analysis is performed by running the model with a varying amount of timesteps. This directly relates to the wakesize, as no wake cut-off is used. The results of this analysis are shown in Table 3.1. Note that these results are made on a 2009 Intel Core2Duo processor with a clockfrequency of 2.53 GHz, and the analysis is for a wing with $n_s = 12$ and $n_c = 7$. An analysis of the effect of both n_s and n_c is also made, as shown in Table 3.2 and Table 3.3 respectively.

Table 3.1: Computation times for different amounts of timesteps. A larger amount of timesteps implies a larger wake. $n_c = 7$ and $n_s = 12$.

Timesteps [-]	5	25	50	75	100	150
Computation time [min]	0.01	0.3	1.8	5.8	15.0	48.0

Table 3.2: Computation times for different amounts of spanwise panels. $n_c = 5$ and $n_t = 50$.

n_s [-]	2	5	10	25
Computation time [min]	0.4	0.5	1.8	10.9

The results have been used to fit exponential functions to have a means of estimating the calculation time. These functions yield the calculation time in seconds:

$$t_{calc}(n_t) = 11.61 \cdot n_t^{0.3331} - 4.575 \tag{3.25}$$
$$t_{calc}(n_s) = 1.306 \cdot n_s^{0.4633} - 1.424 \tag{3.26}$$
$$t_{calc}(n_c) = 50.29 \cdot n_c^{0.4224} - 56.08 \tag{3.27}$$

This shows that increasing the amount of spanwise panels leads to the largest increase in computation time, all else staying equal. It was found that a calculation, with $n_s = 24$, $n_c = 5$ and $n_t = 40$ takes 3.4 minutes to calculate, for a simulation time of $t = 5$ seconds. It should be noted that a change in the amount of timesteps directly leads to a different wake size if the simulation time is kept constant (as the size of one wake block is $V_\infty \mathrm{d}t$). This is thus a factor that should be considered in choosing the amount of timesteps used.

3.3.3. Steady flow

First the steady-state behaviour of the model is discussed, in other words the point where the unsteady effects of the aerodynamics have disappeared. Figure 3.5 shows the model getting closer to the results of a flat plate airfoil, with increasing aspect ratio. This is as expected, as an aspect ratio of $\mathit{AR} = \infty$ should yield the two-dimensional result of $C_l = 2\pi\alpha$. Figure 3.6 shows the spanwise distribution of lift for wings of different taper. The distributions match the expected shapes.

The verification of the induced drag calculation is shown in Figure 3.7. Here the lift-drag polar for planar wings of different aspect ratio is compared to the theoretical induced drag result of $C_{D_i} = C_L^2/\pi\mathit{AR}$. It is seen that increasing aspect ratio decreases the induced drag, as expected. It is also seen that the induced drag stemming from the model is slightly higher than the theoretical result. This can be explained by the fact that the wing modelled here is compared to one with a spanwise efficiency of $e = 1$.

Figure 3.8 shows the pitching moment coefficient with angle of attack for planar wings of different aspect ratio. This is shown for different moment reference locations and is compared to the quarter-chord pitching moment of a NACA 0006 airfoil from [61]. This airfoil was modelled in the UVLM with a flat plate wing of $\mathit{AR} = 100$. It is seen that the UVLM predicts the quarter-chord moment quite different from the experimental results. If, however, the moment reference point is changed slightly (with $0.02c$ forwards), the results match almost exactly except for $\alpha = 10°$. Here the experimental results show the effect of viscosity, which is not modelled in the UVLM. From this it can be deducted that the aerodynamic center location (expected at $x/c = 0.25$ in this case) is wrongly predicted. It is however predicted to be located very close to the expected position. This could be due to the choice of force attachment point, which was set at the leading edge of the vortex rings based on literature.

In Figure 3.9 the effect of sweep angle Λ and aspect ratio AR for planar wings is shown, and compared to experimental results taken from [54]. It can be seen that with increasing sweep angle, the results

Table 3.3: Computation times for different amounts of spanwise panels. $n_s = 10$ and $n_t = 50$.

n_c [-]	2	5	10	25
Computation time [min]	1.4	1.6	1.9	3.1

deviate further from the validation data. For $\Lambda < 30°$ the UVLM yields results that are within limits, but not for larger sweep angles. This implies that the model cannot be used with such large ($> 30°$) sweep angles. As the error in C_{L_α} increases with increasing sweep, a trend has been found to calculate the error in lift curve slope:

$$err_{C_{L_\alpha}} = 0.01884 \cdot \Lambda - 0.05153 \tag{3.28}$$

Finally, Figure 3.10 shows the lift curve slope versus aspect ratio. It can be seen that the results match the experimental results, thus validating the steady-state behaviour of the model.

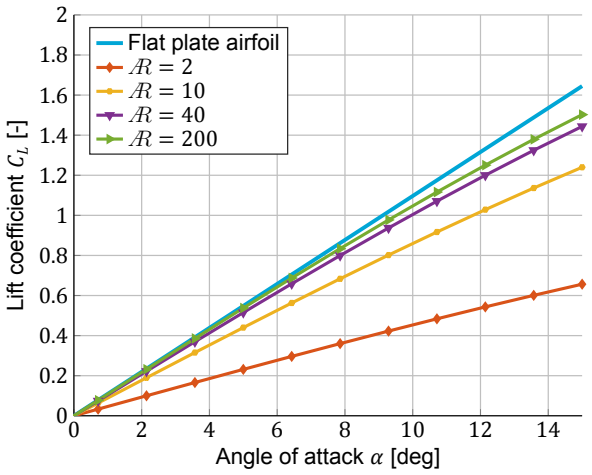

Figure 3.5: C_L versus angle of attack for a planar wing of different aspect ratios, compared to the theoretical lift curve slope of 2π [rad^{-1}].

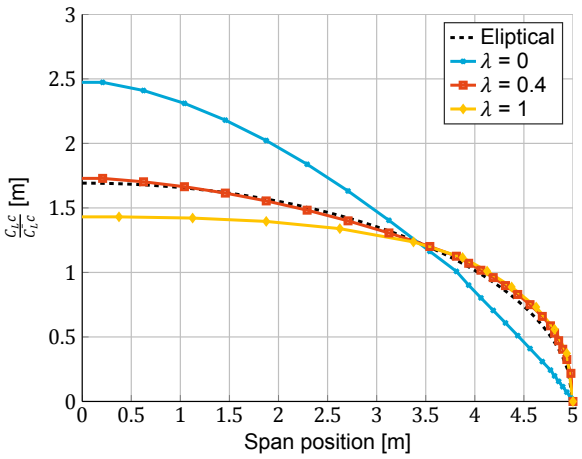

Figure 3.6: A comparison of spanwise lift distributions over planar wings of different taper ratios λ.

3.3.4. Unsteady flow

In order to perform the verification and validation of the unsteady behaviour of the UVLM several cases are investigated. First the time-dependent behaviour of C_L after an impulsive start of planar wings of different aspect ratio (Figure 3.11) is analysed. This is compared to results of [54]. As can be seen, the results match very close to the values from Katz and Plotkin.

Figure 3.12 shows a similar graph but now with the induced drag coefficient C_{D_i}. Again the results are compared to [54]. The induced drag does not match those of Katz and Plotkin exactly, as the drag is increasingly underpredicted with increasing aspect ratio. This is deemed acceptable for the current work, as drag is much smaller than lift. However, this is something that should be looked at for further work and it should be kept in mind during usage of the model.

Another validation case is a comparison with the Wagner function [17], which models the lift over time after a sudden acceleration of an airfoil. Wagner's function and the present model are compared in Figure 3.13, where the model has been run with an aspect ratio of $\mathcal{AR} = 140$ to simulate a two-dimensional behaviour. It is seen that the UVLM models the Wagner function quite closely, such that it can be said that it models accelerations of an aircraft sufficiently.

Finally, Figure 3.14 shows a comparison to experimental results as performed by Halfman [62]. Here the magnitude of complex lift - being equivalent to $L/2qb$ [27] - is shown for a purely plunging airfoil.

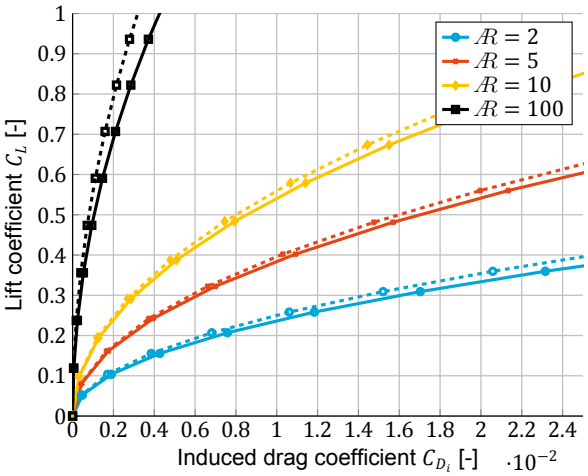

Figure 3.7: Lift-drag polar for planar wings of different aspect ratio, compared to the theoretical induced drag value of $C_L^2/\pi\mathcal{AR}$ (dotted).

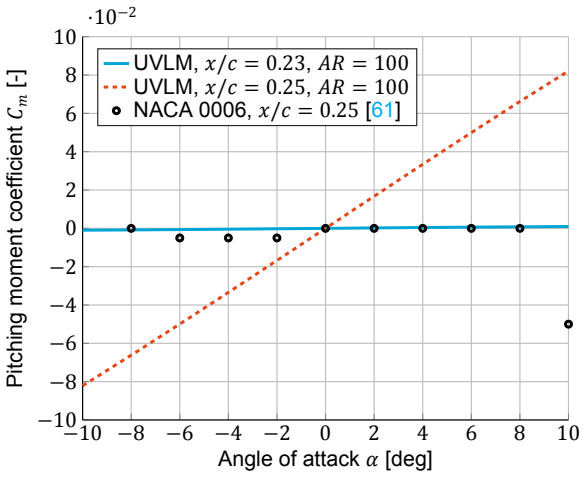

Figure 3.8: Pitching moment coefficient as a function of angle of attack for planar wings of different aspect ratio at different reference points. Calculation compared to quarter-chord pitching moment NACA 0006 airfoil data from [61].

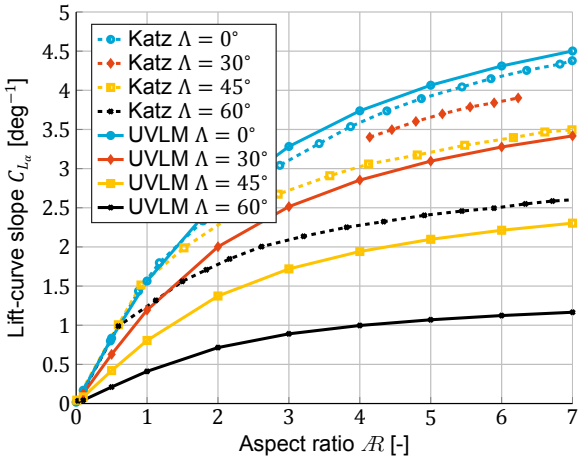

Figure 3.9: Comparison of C_{L_α} versus $\mathcal{AR}$ for planar wings of different sweep angle Λ. The UVLM is compared to experimental results taken from [54].

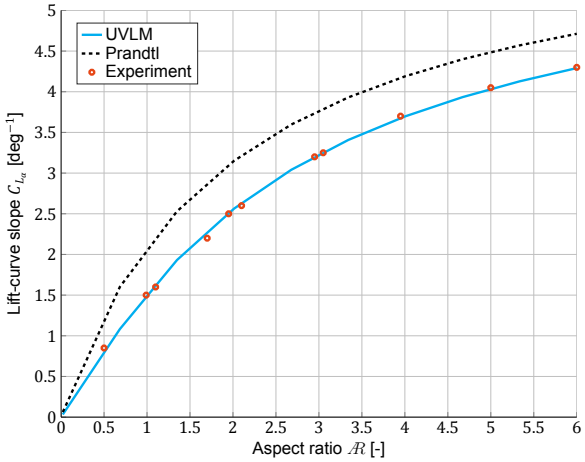

Figure 3.10: The lift-curve slope for a straight, planar wing of different aspect ratios compared to an analytical approximation by Prandtl, and to experimental results [53, pp. 462].

This airfoil in simulated in the UVLM by using a planar wing of $\mathcal{AR} = 100$, at zero angle of attack. It can be seen that the values of the UVLM are close to those of Halfman, validating the unsteady behaviour of the model.

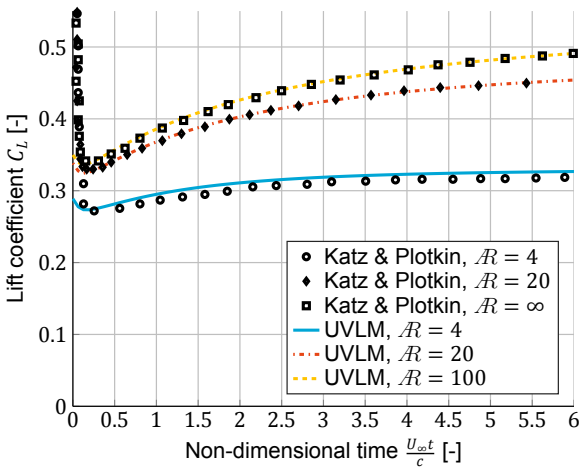

Figure 3.11: The value of C_L over (non-dimensionalised) time for planar wings of different aspect ratio under an angle of attack of $\alpha = 5°$. Results are compared to data from [54].

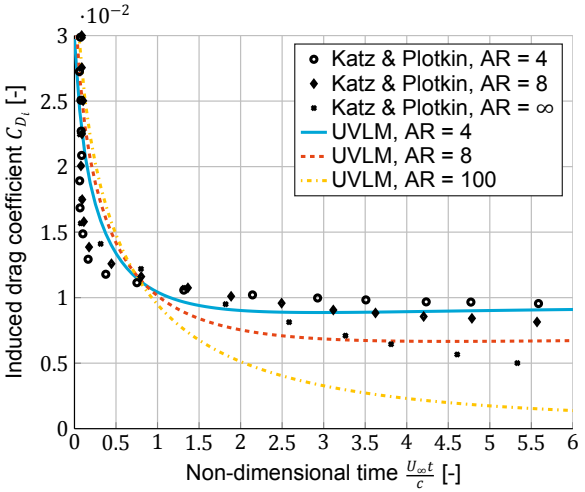

Figure 3.12: The value of C_{D_i} over (non-dimensionalised) time for planar wings of different aspect ratio under an angle of attack of $\alpha = 5°$. Results are compared to data from [54].

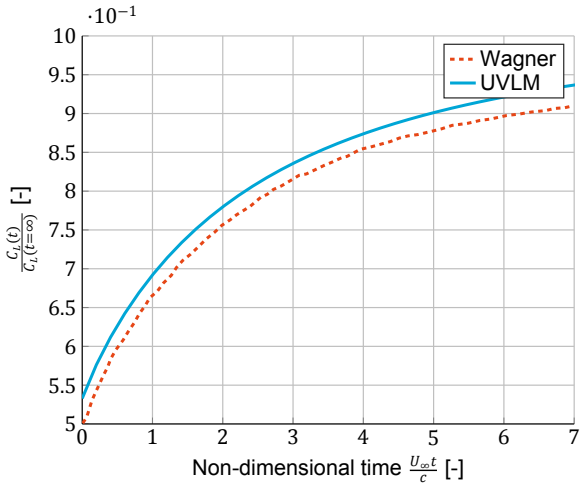

Figure 3.13: The value of $C_L(t)/C_L(t = \infty)$ over (non-dimensionalised) time for a planar wing under an angle of attack of $\alpha = 5°$. Results are compared to the Wagner function [17, 54].

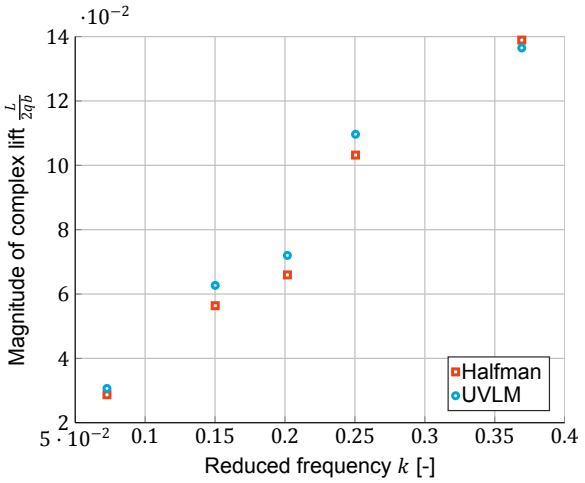

Figure 3.14: The magnitude of complex lift (equivalent to $L/2qb$) at different reduced frequencies for a purely plunging airfoil ($\mathcal{R} = 100$ in simulation) at zero angle of attack. Results are compared to those of Halfman [62].

3.4. Summary

In this chapter the theory behind the unsteady vortex lattice method has been explained. A more detailed overview and user manual of the model can be found in Appendix A. This model allows for modelling arbitrary motion of wings, and also the motion of the wake trailing these wings.

During the verification and validation of the model it was found that there is good agreement with reference results, but only within certain modelling limits. These limitations are summarised here, and should be taken into account during usage of the model.

First of all, the unsteady induced drag prediction was found not to be accurate for wings with $\mathcal{R} > 8$ and even for wings of $\mathcal{R} < 8$ there is an error with respect to reference data. This is accepted however, as induced drag is of little importance in flight mechanics applications, and the trends are predicted correctly. Secondly, it was found that the model has limitations with regards to sweep angle. While trends are again predicted correctly, it was found that for sweep angles larger than 30° the model cannot be used. For wings with a sweep of 30° an error of about 20% is observed with respect to the lift curve slope. The model thus underpredicts the amount of lift generated for swept wings. As the current work

will look at aircraft that rarely have sweep angles larger than 30° again this is accepted. Thirdly, it was found that the aerodynamic center prediction is slightly off compared to experimental results. The UVLM predicts its location to be slightly more forward, which should be kept in mind during calculations. Finally, it was found that in the unsteady case the model is quite sensitive to the amount of timesteps that are used. While this can be expected - with higher frequency motions a smaller timestep is required - the relation between the frequency of the motion and the timestep is not always clear making it hard to put a handle on this.

In summary, the model works for the types of wings under consideration in the present work, with some offset on the pitching moment. It is therefore decided to use the model as is, however adaptions and extensions to the program are required if one wants to analyse less standard wings and will thus be left as a recommendation for future work.

Finally, Appendix D shows some examples of the wake behind wings performing various motions.

4

Aeroelastic flight mechanics

With a validated unsteady aerodynamic model work can be started on connecting this aerodynamic model to the aeroelastic flight mechanics toolbox. This model is called PHALANX, but will be referred to as FMT in this chapter. Some information on this FMT is given in Section 4.1. Naturally some steps need to be taken in order to make this connection happen, as will be explained in Section 4.2. With the addition of the unsteady aerodynamics, the trim routine included in the FMT should be adjusted in order to provide a starting point for subsequent simulation. This trim procedure will be elaborated upon in Section 4.3. After the connection between these two programs it should be verified to work correctly, as will be done in Section 4.4. The chapter is summarised in Section 4.5.

4.1. Aeroelastic flight mechanics toolbox

The FMT is a Simulink/Simmechanics program that can model the flight mechanics of an aircraft with flexible wings [12]. This section will detail on how the aircraft is modelled in the toolbox (Subsection 4.1.1). Moreover, Subsection 4.1.2 will explain the structural model used for modelling the flexible wings.

4.1.1. Aircraft model

The aircraft is modelled in the FMT as a combination of a fuselage, the wings, the horizontal tail and the vertical tail. The lifting surfaces are all connected to the fuselage. The fuselage is the part in which the position of the aircraft is tracked with respect to the ground. In order to simulate the proper aircraft movement, the parts making up the aircraft are all subject to forces and have an inertia. The aerodynamic forces acting on the model are (in the original implementation) determined by look-up tables. Other forces such as the engine force, and weights are either specified by user input or are calculated from geometry.

For the fuselage, the mass, inertia and drag force are modelled using different methods. Raymer [63] is used for the fuselage mass estimation, while DATCOM [55] is used for inertia estimation. Finally, the drag estimation is based on Roskam [56]. The geometric parameters of the fuselage (such as length and diameter) are user input.

Attached to this fuselage are the wings, and the attachment point is specified by the user. The wings are modelled with a rigid wing basis, where the effect of the wing forces on the overall aircraft are specified (see Figure 4.1). This rigid wing can rotate and translate based on the flight dynamics of the aircraft. In other words, it follows the movement of the aircraft itself. Next to this rigid wing is a flexible wing, that moves with respect to the rigid wing basis. This flexible wing models the actual (deflected) shape of the wing and is modelled using several two-dimensional sections, each having no mass. These sections are connected to each other, such that they cannot move completely independently from each other. The sections can move in vertical, horizontal and pitch direction which changes the actual

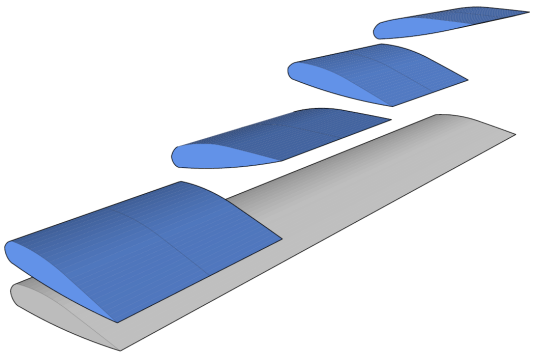

Figure 4.1: An illustration of the rigid wing basis, with the flexible massless bodies. Taken from [12].

wing geometry. Based on this flexible wing geometry the forces and moments acting upon the wing are calculated (either using quasi-steady aerodynamics, or the UVLM) and these forces and moments are fed into a state-space calculation to determine the translations and rotations of these flexible sections. These forces are also transferred to the rigid wing, in order to determine the wing root forces and moments. In this way the forces and moments of the wing are also passed to the aircraft.

Also attached to the the rigid wing are the engines, wing control surfaces, landing gear and flaps. These objects introduce their weights, and also aerodynamic forces (for the control surfaces and flaps) or thrust. The thrust of the engine is modelled with a control setting, meaning a percentage of maximum thrust is used. The effect of the aileron and flaps are modelled using aerodynamic look-up tables.

Next to the wings there is an empennage attached to the fuselage. This empennage consists of a vertical tail, and the horizontal tail. The position of this tail is specified by the user, and they are not modelled as flexible bodies. Instead they are modelled as rigid bodies having a mass and aerodynamic forces. These aerodynamic forces are again determined using look-up tables. Also attached to these tails are the elevator, and rudder that are used to control the aircraft.

While the current work implements a new aerodynamic model for the FMT, this is only done to the massless wing sections. This means that the original implementation of look-up tables for the empennage and control surfaces are still used. These forces are therefore superimposed on the UVLM results, in order to provide aircraft control.

4.1.2. Structural model

The movement of the massless bodies with which the wings are modelled depend on the aerodynamic forces and moments, as well as the structural properties of the wings under consideration. The structural model in the FMT is based on the principle of modal superpositioning. The main assumption behind this principle is that the structural deflections can be modelled as a linear combination of a limited set of structural vibration mode shapes [64]. An example of such vibration modes are shown in Figure 4.2.

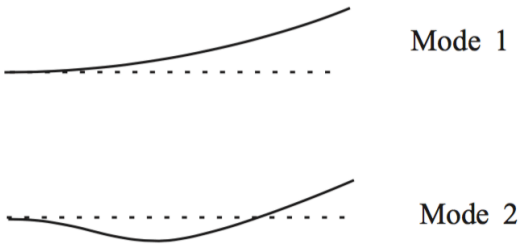

Figure 4.2: An example of mode shapes of a two dimensional system. Taken from [15].

Using this representation for the structural deflection of the wing reduces the amount of degrees of freedom of such a representation. This is because only the amplitudes of the mode shapes are required, instead of the actual deflection of each structural node. The main equation behind the modal approach is Equation 4.1 [65]:

$$\mathbf{s} = \Phi\mathbf{q} \tag{4.1}$$

Here $\mathbf{s}$ are the physical coordinates of the structural representation, while $\mathbf{q}$ are the modal coordinates (i.e., the amplitudes of the mode shapes). Φ determines the relation between these two sets of coordinates. It is a matrix where each column describes the relation between a mode shape and the degrees of freedom of the model.

The structural modes are an input in the program, as the FMT is not able to calculate these. The structural modes thus need to be known beforehand. These modes can be calculated using finite element software such as NASTRAN, or using other structural modelling tools such as EMWET [66]. In the current work, 6 mode shapes are used to model the structural behaviour of the wing.

4.1.3. Outputs of the FMT

Naturally results need to be obtained after a simulation using the FMT. Several results are of interest and are therefore given by the FMT. First, the aircraft flightpath during the simulation. This includes its position, velocity and acceleration over time in all degrees of freedom under consideration. Secondly, information on the wing shape during the simulation is of interest. This includes the deflections of the wing, in all degrees of freedom. Finally, one likes to know the wing root bending moment of both wings during the simulation. Table 4.1 shows a summary of the output variables of the model.

Table 4.1: Output of the FMT

Flight mechanics	Structures	Forces
Position (x, y, z)	Wing vertical deflection $\bar{u}_v$	Left wing root bending moment M_{left}
Velocity (u, v, w)	Wing horizontal deflection $\bar{u}_h$	Right wing root bending moment M_{right}
Acceleration $(\dot{u}, \dot{v}, \dot{w})$	Wing twist angle $\bar{i}_\theta$	Load factor n
Orientation (ϕ, θ, ψ)		
Angular velocity (p, q, r)		
Angular acceleration $(\dot{p}, \dot{q}, \dot{r})$		
True airspeed V_∞		

4.2. Connecting the unsteady aerodynamics

To connect the UVLM and the FMT both programs need a way of communicating with each other. The FMT needs to provide the UVLM with information of the aircraft position, orientation and motion (POM) whereas the UVLM needs to provide the aerodynamic forces and moments acting on the wing to the FMT.

This communication is handled by Simulink/SimMechanics, as that provides an interface to use MATLAB functions inside the existing SimMechanics FMT model. Some changes to the SimMechanics model need to be made for this connection, as explained in Subsection 4.2.1. Furthermore the FMT and the UVLM are not directly compatible, and need some input/output conversion. This is explained in Subsection 4.2.2 for the input to the UVLM and Subsection 4.2.3 for the output of the UVLM.

4.2.1. Changes to the SimMechanics model

The UVLM is added to the FMT as a subsystem, using the original MATLAB code. In this subsystem the UVLM MATLAB code itself is included, as well certain inputs to the UVLM code. A schematic of this subsystem is shown in Figure B.1. A more detailed overview of the exact Simulink blocks used are found in Appendix B.

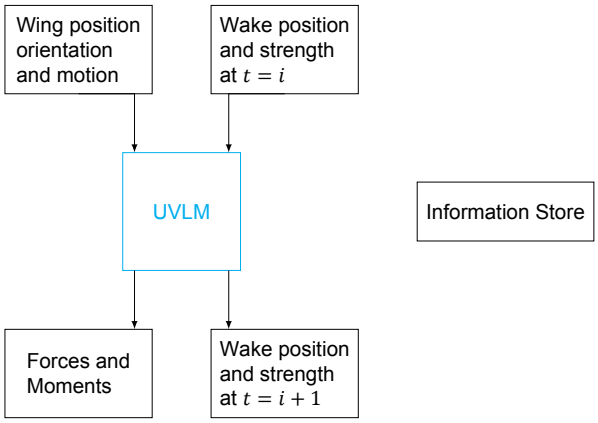

Figure 4.3: A schematic overview of the UVLM subsystem as included in the flight mechanics toolbox.

The main part of the subsystem is the UVLM code itself. As input to this code the wing position, orientation and motion (POM) is required, as well as the wake position and strength at the current time-step. There is an information store block that saves the wake position and strength. Some other values are stored here as well, such as the aircraft orientation at the previous time-step, and a flag that keeps track on whether the wake has reached a steady state. These values are also passed to the UVLM code. The UVLM code outputs the aerodynamic forces and moment, which are subsequently send to their respective wing sections in the Simulink model. Furthermore, the UVLM yields an updated wake position and strength which are stored in memory for use in the next time-step.

Next to these inputs and outputs, the UVLM receives some other parameters internally. These parameters include atmospheric parameters such as speed of sound, density and pressure. The overall (rigid) aircraft position and orientation is also given to the UVLM, as well as information on the wing geometry and information on the gusts. Finally, simulation parameters such as the number of time-steps is provided to the UVLM.

The number of time-steps in the simulation is known beforehand, as the model is solved using a fixed-step ordinary differential equation solver in the form of an Euler solver. This is different to the FMT without unsteady aerodynamics, which uses a variable time solver. The reason for this change is due to the pre-allocated wake, which requires the number of time-steps to be known. Moreover, as the UVLM is integrated using the Euler integration scheme, this is chosen for the complete model as well. It should be noted that using the Euler integration scheme in Simulink yields an update step, while the UVLM has this update step included in the code itself. This is the reason for the counter variable that is saved, as that is used to make sure the wake is not updated with already updated wake positions. If this is not done the wake position would be updated twice in each timestep, making for an unstable and nonphysical calculation.

To summarise the steps taken to run the FMT with the UVLM, a flowchart is made. This flowchart can be seen in Figure 4.4.

4.2.2. FMT to UVLM

Naturally, the FMT and the UVLM are not directly compatible with each other. Certain calculations are required in order to go from the wing section definition of the FMT to an aerodynamic grid in the UVLM. Such calculations are needed for both the aerodynamic grid, and the velocity of the wing sections.

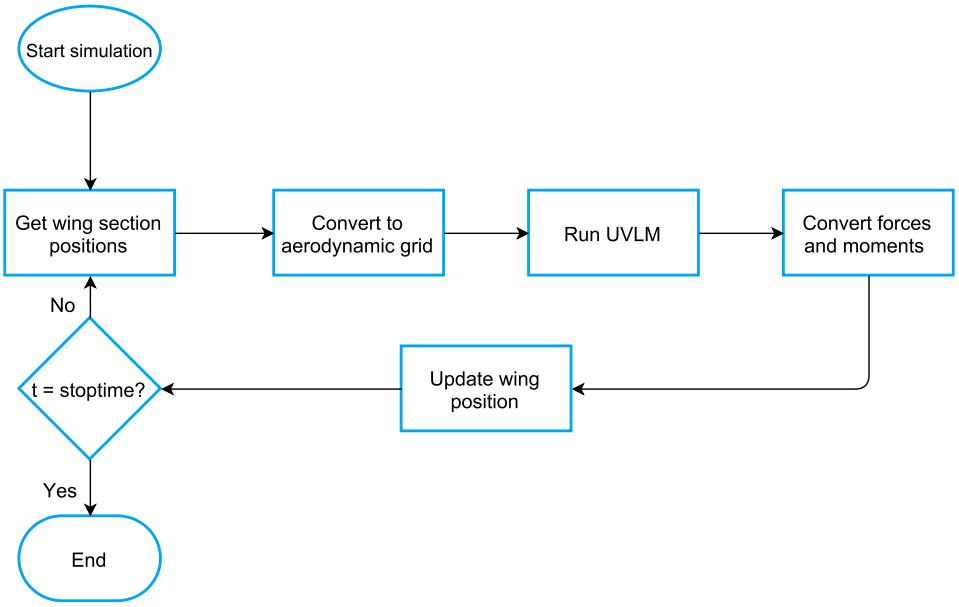

Figure 4.4: A flowchart of the steps taken to run the flight mechanics toolbox with the unsteady vortex lattice method. A simulation is started, after which the wing data from the flight mechannics toolbox is used to build an aerodynamic grid. The aerodynamic model then calculates forces and moments, which are used to move the wing in the flight mechanics toolbox.

Grid

First of all, the position of the wing sections in the FMT - which are points in space - need to be converted to a wing definition. An illustration of the problem is shown in Figure 4.5, for only two wing sections.

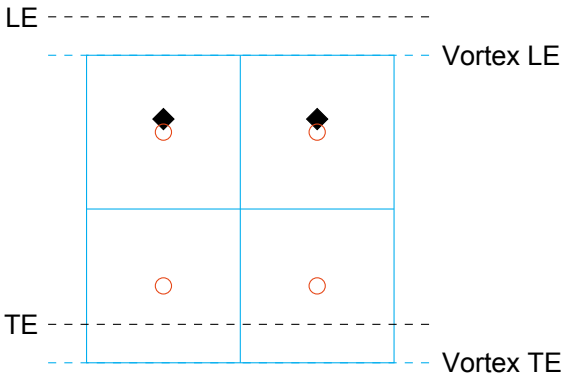

Figure 4.5: An illustration of the relation between the FMT nodes (black diamonds) and the aerodynamic grid. Pictured is the vortex grid (blue, rectangular) with the collocation nodes (orange, circles). From the known positions of the FMT nodes, all corner points and collocation points can be calculated.

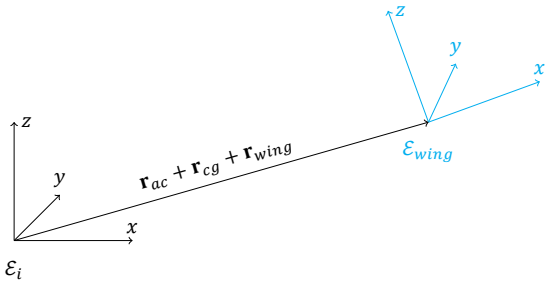

Figure 4.6: An illustration of the inertial and wing reference frame, and their respective orientations.

The FMT nodes are depicted by the black diamonds, and for clarity only the vortex grid is shown. The collocation points (orange circles) are also shown. The following explains how to convert from the known positions of the FMT nodes, to the vortex grid and collocation points.

The first step is the definition of several reference frames. The first frame is the inertial frame $\mathcal{E}_i$, with location $(x, y, z) = (0, 0, 0)$ and orientation parallel to the ground. This frame is used to describe the aircraft movement, and for the UVLM it has its z-axis positive upwards (it is thus rotated $180°$ compared to the FMT inertial frame). While the inertial frame is used to define the flightpath and calculate the movement of the wake, the aerodynamic calculations take place in the local wing frame $\mathcal{E}_{wing}$. The origin of this wing grid is located at the wing reference point (this is the location where the wing leading

edge would cross the symmetry plane). In order to translate from the inertial frame to the wing frame, some vectors are used. First $\mathbf{r}_{ac}$ is used to specify the position of the aircraft reference point with respect to the inertial frame origin. $\mathbf{r}_{cg}$ denotes the distance from the aircraft reference point to the aircraft center of gravity, and $\mathbf{r}_{wing}$ denotes the distance from the center of gravity to the wing reference point. The origin of the wing frame $\mathcal{E}_{wing}$ with respect to the inertial frame is thus denoted by $\mathbf{r}_{ac} + \mathbf{r}_{cg} + \mathbf{r}_{wing}$. Next to this translation, the frame is rotated with respect to the inertial frame with the aircraft orientation Ω. These frames are illustrated in Figure 4.6.

With the references frames defined, the grid construction can be explained. The first step is to take out the aircraft body rotation Ω from the wing section positions $\mathbf{g}_i$. This makes the calculation of the leading edge (LE) and trailing edge (TE) easier as this is now defined along the inertial x-axis. To do this, the coordinates are rotated around the aircraft center of gravity:

$$\begin{aligned} \mathbf{g}_{cg} &= \mathbf{g}_i - (\mathbf{r}_{ac} + \mathbf{r}_{cg}) \\ \mathbf{g}_{cg,rot} &= \Omega^{-1}\mathbf{g}_{cg} \\ \mathbf{g}_{i,rot} &= \mathbf{g}_{cg,rot} + (\mathbf{r}_{ac} + \mathbf{r}_{cg}) \end{aligned} \tag{4.2}$$

With this rotation taken out, the position of the LE and TE are calculated. The wing section positions from the FMT are defined at the elastic axis location, and for each section it is known what the elastic axis position on the wing chord is. Together with knowledge on the wing section inner and outer chord length, the chordwise LE and TE positions of each section can be obtained in a straightforward manner:

$$\mathbf{x}_{LE} = \mathbf{x}_{EA} + \frac{c_r + c_t}{2}\left(\frac{\mathbf{x}}{\mathbf{c}}\right)_{EA} \tag{4.3}$$

$$\mathbf{x}_{TE} = \mathbf{x}_{EA} + \frac{c_r + c_t}{2}\left[1 - \left(\frac{\mathbf{x}}{\mathbf{c}}\right)_{EA}\right] \tag{4.4}$$

Since the wing can be under an incidence angle, and the wing sections themselves can have a rotation (due to flexible wing deflection), the y and z coordinates of the LE and TE need to be found using another rotation, using the same manner as Equation 4.2. Now the rotation matrix used is $[\alpha]_i[\Omega]_{sec}$, which is the wing fixed rotation and the flexible wing section rotation, respectively.

Now that the positions of the LE and TE are known, the aerodynamic grid can be constructed. As the FMT wing sections are located in the middle of the vortex rings, some calculations are still needed. First, the span position y of the aerodynamic grid points are calculated by adding the local semispan $b_{loc}/2$ to the span positions (except at the wing tips). From these span positions, a linear interpolation is performed to find the LE and TE chordwise positions. Another interpolation is used to find the associated z coordinates. At this point the LE and TE positions of the aerodynamic grid corners are known. Another interpolation in x-direction is then used to find the inner grid coordinates (i.e. the chordwise sections).

To move to the vortex grid, all sections are shifted backwards with $0.25c_{loc}$, where c_{loc} is the local chord. Since the y-coordinates of the vortex grid are equal to those of the wing grid, only the associated z-coordinates need to be calculated, which is done with a linear interpolation. Next to the vortex grid, also the collocation points (orange circles in Figure 4.5) need to be calculated. As these are located in the middle of the vortex rings it is possible to use the y position of the FMT wing sections. A linear interpolation is then performed to find the x and z coordinates of the collocation points.

Now we have all grids in global space, but without the rigid aircraft orientation. To get the inertial grids (expressed in $\mathcal{E}_i$), the previously mentioned grids are rotated with Ω. For the calculation grids, which are expressed in $\mathcal{E}_{wing}$, the orientation is as required, but the position is not yet finalised. It needs to be expressed with respect to the wing reference position, and is thus translated with $(\mathbf{r}_{ac} + \mathbf{r}_{cg} + \mathbf{r}_{wing})$. To move between the two grids, the following mathematical expression can be used:

$$\mathbf{g}_{wing} = \Omega^{-1}\alpha_y^{-1}\left(\mathbf{g}_i - (\mathbf{r}_{ac} + \mathbf{r}_{cg})\right) + \mathbf{r}_{cg} - \mathbf{r}_{wing} \tag{4.5}$$

Finally, this conversion is summarised in a flowchart, shown in Figure 4.7.

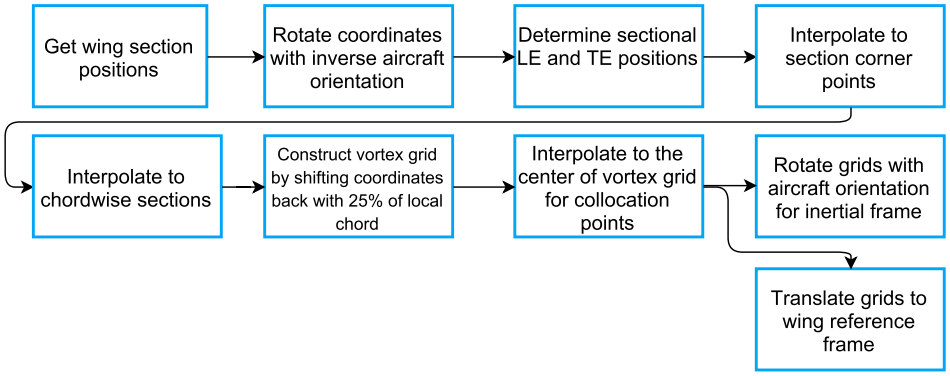

Figure 4.7: Flowchart showing the procedure to convert FMT node positions to UVLM grids.

Velocity

Next to converting the FMT wing position to aerodynamic grid positions, the velocity of the collocation points of the aerodynamic grid need to be known at each timestep. The velocities of the FMT wing sections is measured (again at the elastic axis location). Using this information, together with the location vector calculated previously it is possible to interpolate the velocity to each collocation point:

$$\mathbf{V}_{col} = \mathbf{V}_{FMT} - \mathbf{V}_{\infty} + \omega \mathbf{r}_{col} \tag{4.6}$$

where $\mathbf{V}_{FMT}$ is the velocity of the wing section, ω the rotational velocity at the elastic axis of the wing section and $\mathbf{r}_{col}$ the position vector of each collocation point to the elastic axis of the section. The velocity is expressed without the rigid aircraft velocities, and is converted to the UVLM frame of reference (i.e., having its z-axis upwards positive). The gust velocity on the wing is added at a later stage, as this is not a wing deflection velocity.

4.2.3. UVLM to FMT

Next to converting information from the FMT to fit the UVLM, the other way is also necessary. All forces and moments of the sections should be expressed at the aerodynamic center location. Moreover the forces are expressed in the aerodynamic frame of reference [12]. In order to position the forces at this location the pitching moment with respect to the aerodynamic center needs to be calculated. As the aerodynamic center location of each wing section is known, this can be performed in a straightforward manner by means of Equation 3.21. It should be kept in mind that this calculation will show a small offset with respect to the aerodynamic center position.

With the forces known, two more operations need to be performed. First, the forces and moments calculated by the UVLM are bound by maximum sectional coefficients that are specified by the user. This is to limit the maximum forces and moments that can be achieved, as potential flow is a linear model and thus does not model non-linear effects such as stall. If the calculated values are higher than the maxima, the maximum sectional coefficient is used. Secondly the forces and moments need to be ordered correctly. The UVLM yields the lift, drag and pitching moment of each separate wing panel, whereas the FMT expects this for each wing section. The values for each wing panel are therefore added over the chord, such that a single value per wing section is left. These are then reordered to the same order the FMT expects, which is lift, drag and pitching moment per section instead of vectors of lift, drag and pitching moment.

4.3. Trim

Before a simulation with the FMT is started, the aircraft should be in a trimmed condition (i.e., starting accelerations as specified by the user, generally close to zero). For this reason a trim algorithm is needed. Such an algorithm is already included in the FMT [12], but it needs to be adapted to accommodate for the UVLM as the wake is incompatible with the original trim algorithm.

In a flight mechanics application trim entails that the aircraft is not accelerating along its body axis while also having no angular acceleration. This condition can be written as an objective vector $\mathbf{o}$:

$$\mathbf{o} = [\dot{u}\ \dot{v}\ \dot{w}\ \dot{p}\ \dot{q}\ \dot{r}\ \beta] = \mathbf{0} \tag{4.7}$$

It is possible to change these parameters using the controls of the aircraft, which can be grouped in the control vector $\mathbf{c}$ that includes elevators e, ailerons e, rudder r and the aircraft thrust T:

$$\mathbf{c} = [\delta_e\ \delta_a\ \delta_r\ \delta_T] \tag{4.8}$$

With flexible aircraft there is the addition of an aeroelastic trim term, meaning that the wing deflection must not undergo accelerations. With the addition of the UVLM also the wake must be in a trimmed state. Both these additions add extra complexity to the trim algorithm and increase the objective vector $\mathbf{o}$ in size.

In order to trim the aircraft with the UVLM two distinct steps are taken. First the aircraft is trimmed using quasi-steady aerodynamics. How this is performed is explained in Subsection 4.3.1. This trim state is used as input for the second step in the trim, which is trimming with the UVLM. This is detailed upon in Subsection 4.3.2.

4.3.1. Quasi-steady aerodynamic trim

In order to speed up the trim algorithm when used with the UVLM, the aircraft is first trimmed using the quasi-steady aerodynamic model. This is because the quasi-steady aerodynamic model has a lower computational cost, and can therefore be used relatively 'cheap' to find a starting point for the UVLM trim. This starting point consists of a trimmed elastic wing shape and control inputs required for the desired flight condition.

The trim algorithm used in this case is that of Kalthof [12], which is based on Jacobian trim. In this approach it is assumed that an increase in a control vector is linearly related to a change in acceleration. This allows one to define a so-called Jacobian matrix J, defined as:

$$J_i = \left(\frac{\partial \mathbf{o}}{\partial \mathbf{c}}\right)_i \tag{4.9}$$

This matrix gives the effect of a control input on the aircraft accelerations (i.e., objective vector). In the algorithm this is calculated by simulating the aircraft by using an increase and a decrease in control deflection, and then measuring the response in terms of acceleration. A finite difference method is then used to find the entry to Equation 4.9. With this Jacobian matrix known, a new control vector $\mathbf{c}$ can be determined using Equation 4.10, where $\mathbf{o}_{i+1}$ is defined as $\mathbf{o}_{des}$. For this control vector, the accelerations are then calculated by performing a simulation. If these accelerations are within the trim limit set by ϵ, the aircraft is trimmed. If not, a new iteration is started with the new control vector as a start.

$$[\mathbf{o}_{i+1} - \mathbf{o}_i] = J_i\,[\mathbf{c}_{i+1} - \mathbf{c}_i] \tag{4.10}$$

In an effort to speed up the trim, two methods are used to perform this trim with quasi-steady aerodynamics. At first, the so-called implicit trim method is used. In this method the aircraft is simulated until its flexible wing movement is damped out. Once this is the case, the Jacobian matrix is constructed.

If this implicit method does not lead to a trimmed aircraft state (meaning the wing movement does not damp out quick enough), the explicit algorithm is used. In this case the deflection velocity of the wing is added to the objective vector, in order to drive this to zero [12]. This will thus increase the size of the objective vector and the Jacobian matrix, and in turn the amount of simulations that are required.

4.3.2. UVLM trim

From the output of the quasi-steady aerodynamic trim step, the UVLM trim step can be started. This UVLM trim should yield information on the wake trailing the aircraft, including its shape and vortex strength, as well as the bound (wing) vorticity strength. This is to eliminate any effect of a starting vortex, such that a simulation can be started from a steady state. As a first step the wake is trimmed, and secondly an autopilot is used to bring the aircraft to a steady flight condition with the trimmed wake.

Trimming the wake

At this point there is no wake yet, and therefore the aircraft is simulated once in order to generate a wake of a certain length (defined in terms of wingspan b). This simulation is performed with rigid wings in order to speed up the calculation. Once a wake is available, the aircraft is simulated again, this time with flexible wings. This simulation is iterated until the vortex strength over the wing Γ_b has converged to a steady-state, defined by:

$$\frac{\partial \Gamma_b}{\partial t} < \epsilon \text{ with } \epsilon = 10^{-3} \tag{4.11}$$

During this iteration, each step is started from the previous position and orientation of the aircraft, as well as the previous wing deflection. This ensures that the wake at the new iteration is connected to the wing, such that no numerical inaccuracies arise due to discontinuities between the wing and the wake. It should be noted that having the aircraft start from the previous state can lead to an increasing deviation from the desired trim state. However, due to the fact that the aircraft has been trimmed with a different aerodynamic model this deviation from the desired trim state is limited to small excursions around the objective.

Now a steady wake is available, but the aircraft will most likely not be in a trimmed condition anymore due to differences between the quasi-steady and unsteady aerodynamic models in terms of aerodynamic forces. For this reason the aircraft needs to be trimmed again. Using the trim algorithm of Subsection 4.3.1 does not result in a quick trim solution due to the added computational time that the UVLM brings with it. It is therefore opted to use a control system to bring the aircraft to a non-accelerated state.

Trimming with autopilot

In trimming with an autopilot, the aircraft is started from the previous (quasi-steady aerodynamic) trim state with the trimmed wake trailing the wings. The aircraft is set to fly for a certain amount of time, during which several controllers change the control inputs based on the measured aircraft states and the objective for these states. In this work there will only be looked at the longitudinal aircraft dynamics, such that only three aircraft states need to be controlled. These states are the aircraft velocity $\mathbf{V}$, its flightpath angle γ and its pitch rate q. In order to have the aircraft fly straight and level, these states should reach the following condition:

$$\mathbf{o}_{des} = \begin{cases} V = V_{des} \\ \gamma = 0 \\ q = 0 \end{cases} \tag{4.12}$$

Here V_{des} is the desired velocity. If this objective is reached the aircraft is not subject to any accelerations, leading to the fact that also the wing deflection is constant. To get the aircraft to this $\mathbf{o}_{des}$ there

are two controls that can be used; the elevator and the thrust. To this end, two simple controllers are constructed to change exactly that.

Again this trim is performed in an iterative manner. The aircraft is only simulated for some predefined time, after which it is checked whether the desired state is reached. Also the wing deflection is checked for any accelerations. If the aircraft is not yet in the steady state (defined by an error margin of $\epsilon = 10^{-4}$) another simulation is performed with the end condition of the previous iteration as the starting point. This is performed until the aircraft has reached the desired state, with a constant wing deflection.

The controllers used are shown in Figure 4.8 and Figure 4.9. It should be noted that the gains used in these controllers need to be tuned for the aircraft under consideration. An illustration of the control deflections and the aircraft state is shown in Figure 4.10 for the the elevator controller. Note that these controllers are run concurrently. Finally, it should be noted that the current autopilot trim only works on the longitudinal degrees of freedom. This can be easily extended to lateral control, by adding controllers on the aileron deflection δ_a and the rudder deflection δ_r.

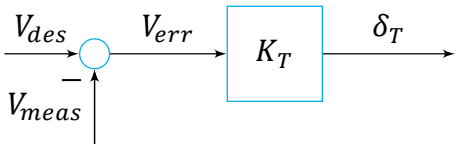

Figure 4.8: The δ_T controller, controlled by a gain K_T and working on the difference between flight velocity and desired velocity.

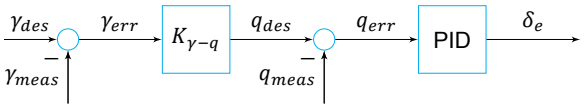

Figure 4.9: The δ_e controller, which works on driving the flightpath angle γ to zero through a change in pitch rate q that is achieved using an elevator deflection δ_e.

Thrust controller The thrust controller shown in Figure 4.8 works through a simple proportional controller, acting on $V_{err} = V_{des} - V_{meas}$. Through the relation $\delta_T = K_T V_{err}$ the thrust is changed accordingly until the aircraft reaches a trimmed condition. Mathematically this means that $V_{meas} = V_{des}$.

Elevator controller The elevator controller from Figure 4.9 is a more complicated controller compared to the thrust controller. First the error signal $\gamma_{err} = \gamma_{des} - \gamma_{meas}$ is calculated, which is subsequently put in a proportional controller to convert this signal to a desired value of the pitch rate q_{des}. This is because it is desired to have an aircraft that is not rotating ($q = 0$). This will happen if $V = \text{const.}$ and $\gamma = 0$. This desired pitch rate is compared to the actual pitch rate q_{meas}, after which the signal is sent through a PID controller. This converts the signal to an elevator deflection, after which the flight path angle is measured in the next step. This continues until the flight path angle is zero. This zero flight path results in $q_{des} = 0$ such that with one control input both γ and q can be controlled.

4.3.3. Finishing trimming

Once the autopilot has flown the aircraft to a steady state, the control deflections and wake properties required for this steady state are saved for further use. As a summary the trim algorithm is shown in flowchart form in Figure 4.11.

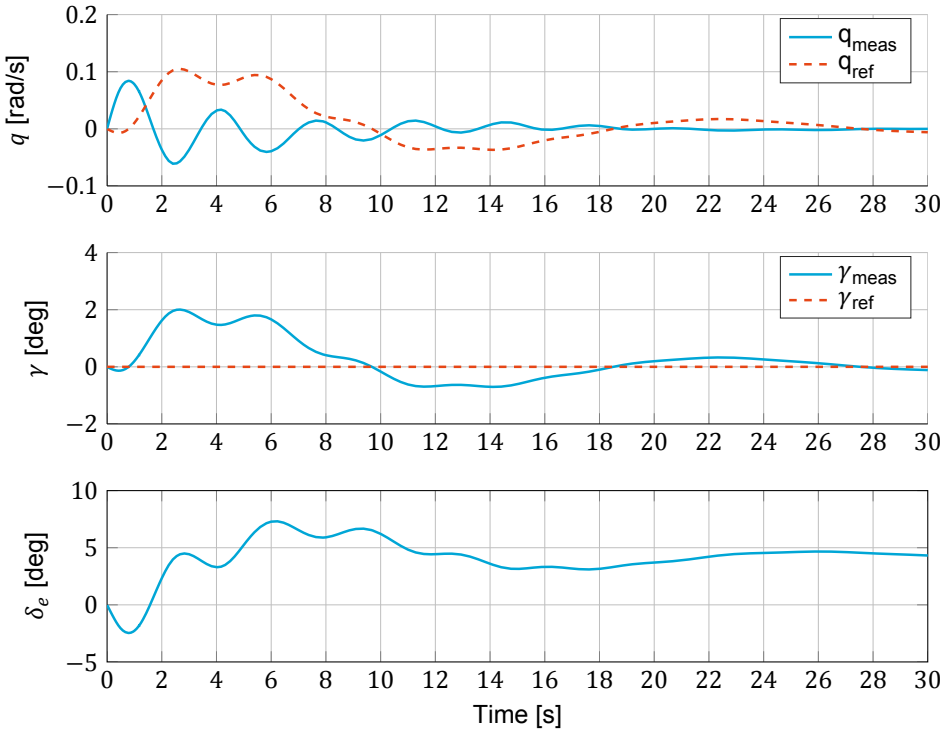

Figure 4.10: The δ_e controller trimming the aircraft to a steady state. The control parameters used are $K_{\gamma-q} = -3$, $P_e = 0.4$ and $I_e = 0.2$.

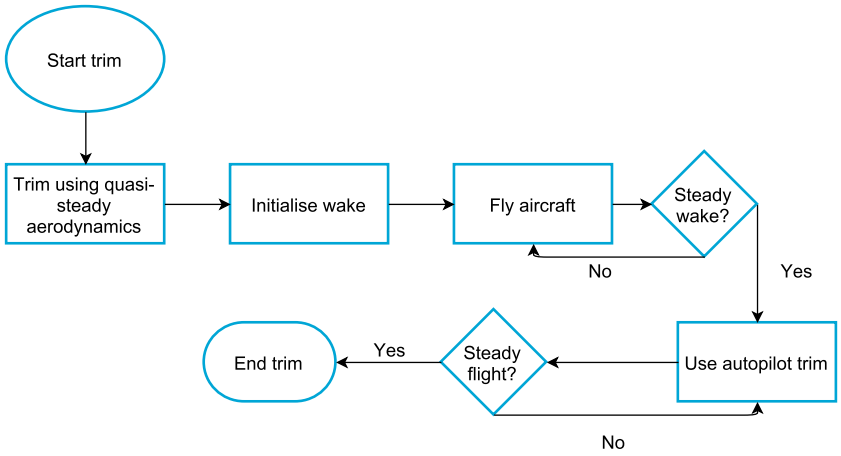

Figure 4.11: A flowchart of the trim algorithm used for the FMT and UVLM combination.

4.4. Verification

To verify the coupling between the FMT and the UVLM there will be looked at three distinct aspects. First the wing shape information is verified (Subsection 4.4.1). Secondly, the flight path information is verified to be conveyed correctly in Subsection 4.4.2. Finally, the forces stemming from the original aerodynamic model and the UVLM are compared in Subsection 4.4.3.

4.4.1. Wing shape

The first step in the verification process is to check the aerodynamic grid that is generated from the FMT wing position. This is shown in Figure 4.12. The wing itself is swept with $\Lambda_{c/4} = 25$ [deg] and has an upwards twist of 6 degrees. The aircraft is flying at an attitude defined by $\phi = 10$ [deg], $\theta = 5$ [deg], $\psi = 10$ [deg]. It can be seen that the wing follows that definition, while also the collocation points are seen to be located at the middle of the vortex rings. This shows that indeed the aerodynamic grid is constructed correctly from the information of the FMT.

Figure 4.13 shows a plot of the wing shape during a simulation as found in the UVLM, compared to the wing shape stemming from the FMT. It is seen that they match exactly, thereby verifying the workings of the wing deflection information that is passed between the UVLM and the FMT.

4.4.2. Fight path

Next to the grid generation, it needs to be checked whether the flightpath found in the UVLM is the same as the flightpath specified in the FMT.

The verification figure of this is seen in Figure 4.14, where the error in vertical (z) and horizontal (x) movement can be seen. There is no error in the horizontal part, and a very minor difference in the vertical flightpath. It should be noted that the wake roll-up calculation has been turned off for this verification, such that the wake position is only based on the flight path. Concluding, the flightpath information is verified to be shared correctly between the FMT and the UVLM.

4.4.3. Aerodynamic forces

Next to this, it needs to be verified that the forces stemming from the UVLM are comparable to those of the original quasi-steady aerodynamic model (as explained in Section 2.1). This is shown in Figure 4.15 for the root section of the right wing. Only this section is shown as all other sections show the same behaviour. These figures are generated by simulating the aircraft using the quasi-steady aerodynamic model, and using the UVLM concurrently to calculate the forces. In this way, the exact same motion and orientation is simulation with both aerodynamic models.

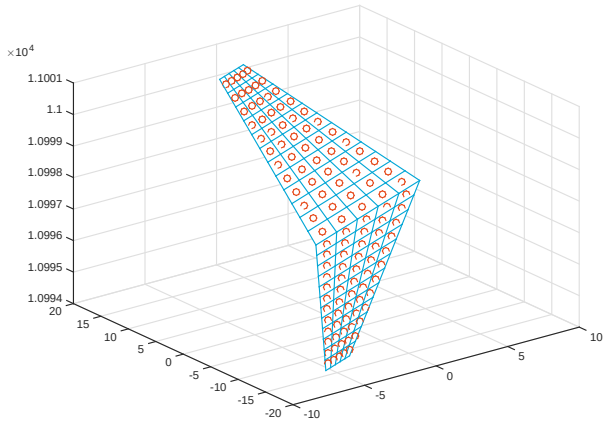

Figure 4.12: The aerodynamic grid that is generated from the wing definition in the FMT. Shown is the wing grid (blue) and the collocation points (red dots), in an attitude defined by $\phi = 10$ [deg], $\theta = 5$ [deg], $\psi = 10$ [deg].

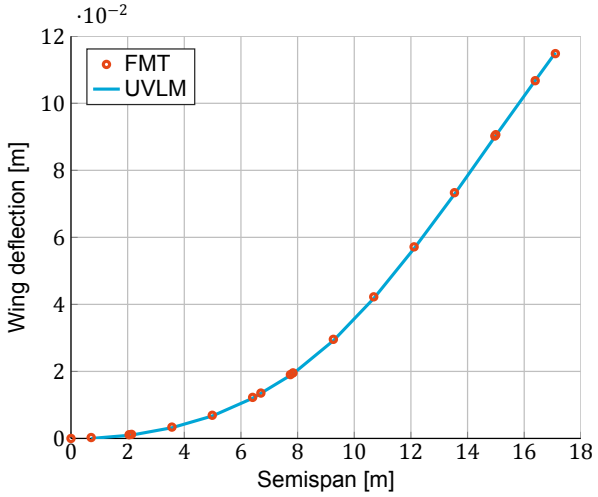

Figure 4.13: The shape of the wing as found in the FMT, and the shape of the wing as found in the UVLM.

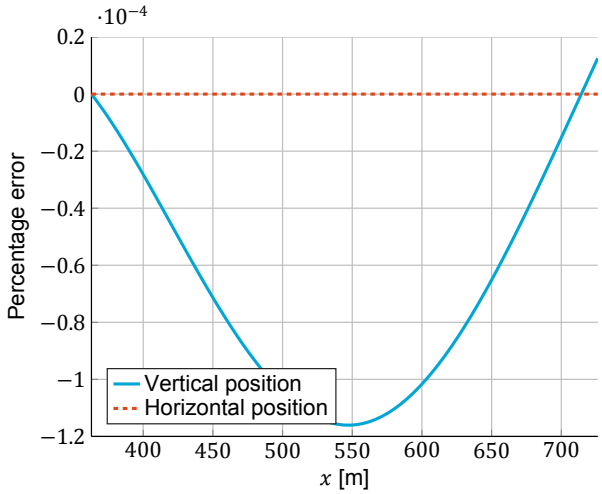

Figure 4.14: The error of the flightpath in the UVLM compared to the FMT. This is done for both the horizontal and vertical movement.

It can be seen that the lift forces of both models are comparable. It is also seen that there is a slight phase difference between the lift peaks of both models. This is expected due to the unsteady aerodynamic modelling, where it takes a longer time for the aerodynamics to reach a peak due to the time history that is embedded in the wake. Moreover, it is observed that the lift predicted by the UVLM has higher peaks than that of the original model.

As for the drag, the UVLM predicts this to be lower than the quasi-steady aerodynamic model. This is expected, as in Section 3.3 it was already shown that drag is underpredicted with this UVLM implementation. Comparing the magnitude of drag to that of lift, it is seen to be much smaller and as such does not have a large influence on the dynamics of the aircraft. It is therefore accepted to have this offset in drag, but it should be taken into account when analysing the results of simulations with the UVLM.

The final comparison is between both models' pitching moment calculation. It is seen that the UVLM predicts a much lower value of the pitching moment. As already seen in Chapter 3 the pitching moment (and its coefficient) is not predicted correctly. Due to this offset, it is expected that the elevator deflections between the models will be different to counter the moment imbalance. With this different elevator deflection, the aircraft with the UVLM will still start in a trimmed position making the offset in pitching moment prediction less of a problem for straight flight. However, the difference in pitching moment is large enough to play a significant role in the results of an aircraft flight dynamics simulation. As such,

it is of utmost importance to keep this in mind during the analysis of the results.

Finally, it should be noted that the sudden increase in all forces and moments from the UVLM at the start of the plots are due to a slight starting vortex. This occurs due to starting the aircraft simulation from a slightly different point compared to the trimmed wake solution, or using a different timestep then the one used with the trimmed wake. This will not occur when the same timestep is used, which is what will be done for the gust simulations.

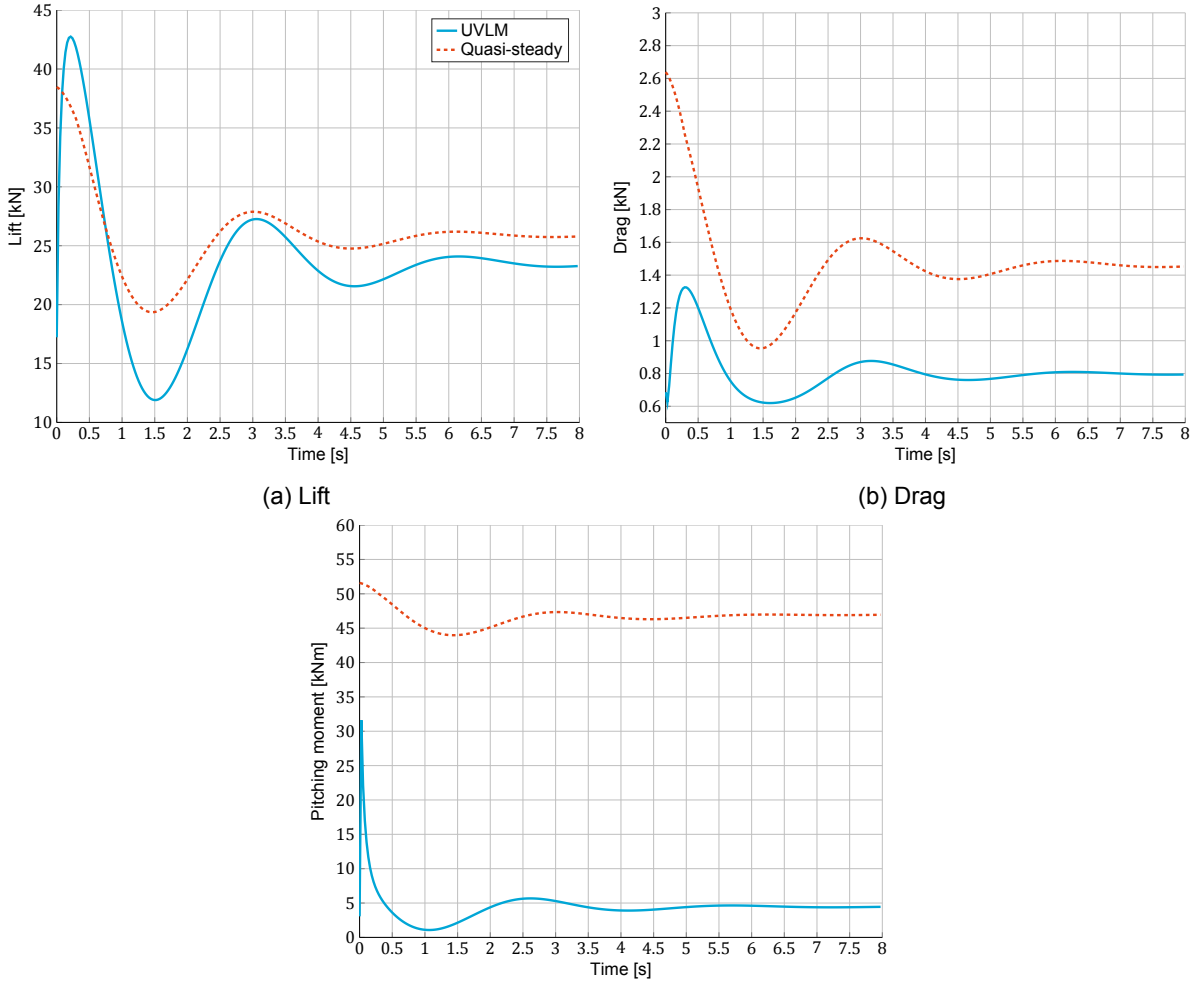

(a) Lift

(b) Drag

(c) Pitching moment

Figure 4.15: A comparison between the lift, drag and pitching moment of the UVLM and the quasi-steady aerodynamic model for the right wing root section at $\eta = 0.04$.

4.5. Summary

In this chapter the connection between the aerodynamic model and the FMT was detailed. As the FMT models its wing sections as points, some extra operations were added to convert these point sections to a calculation grid compatible with the UVLM. Also the velocities of these nodes need to be converted to be compatible with the UVLM, which has been added to the model as well. The output of the UVLM was made compatible with the force and moment definitions of the FMT, such that each spanwise section only yields one force, instead of a force per each panel in the aerodynamic grid.

Some changes to the trim algorithm present in the FMT were also made such that trimming with the wake is possible. An algorithm was designed that takes the trim of the quasi-steady aerodynamic model as a starting point, after which the wake is trimmed to a steady state. From this point on, a simple autopilot flies the aircraft to a steady state as it was found that a mathematical trim approach was

too computationally expensive compared to autopilot trimming when using the unsteady aerodynamic model. The results of trim are shown in Chapter 5.

Finally, the workings of the connection between the models was verified to work correctly. The wing coordinates (including deflections) and aircraft flightpath and movement are converted correctly to the UVLM. The forces and moments stemming from the new aerodynamic model were compared to the original aerodynamic model present in the FMT. It was found that lift agrees reasonably, while drag and pitching moment are calculated to be very different from the original model. As drag has a small influence on the aircraft dynamics, this is accepted. The pitching moment predicted by both models showed a large discrepancy, that might have a significant impact on the results of simulations performed with the model. A discrepancy in pitching moment was also seen in the validation of the aerodynamic model (Chapter 3). This discrepancy should be kept in mind when analysing the results as done in Chapter 5.

Summarising, the connection between the tools is verified to work correctly. The forces predicted by the UVLM are not the same as those predicted by the quasi-steady aerodynamic model, with the largest difference being in the pitching moment. The connection between the tools allows for running simulations, which are found in Chapter 5.

5

Results and discussion

This chapter will show the results generated during this work. First a comparison between the original, and the adapted gust model is made. This is to analyse the effect of a time-delay in the gust velocity of staggered aircraft parts. This is shown in Section 5.1. Secondly, the trim results of the simulation aircraft are analysed, as shown in Section 5.2. With the results of the gust model, and trimmed aircraft the results of the gust simulations will be shown and discussed in Section 5.3. To prove the capabilities of the tool, there will also be looked at the response after an elevator input. This is done in Section 5.4. Note that this chapter will refer to the quasi-steady aerodynamic model as QS.

Before the results are shown, a discussion on the wake is needed. While Chapter 3 mentioned that the wake size would be 4 wingspans in length, this was found to be too computationally expensive. While working fine as a standalone MATLAB program, once compiled for use with Simulink the memory usage of the code increases drastically. This leaves two options; shortening the wake or decreasing the amount of points in the wake. Decreasing the amount of points in the wake for the same wake size makes the wake calculation more numerically unstable (as the size is fixed by the timestep), so it is opted to decrease the wake size to two wingspans. To see the effect of this reduction in wake size, a small convergence study is performed, as shown in Figure 5.1. Here the value of C_L over time is shown for simulations with a different wake size. These simulations were started from a trimmed solution of the wake. As can be seen, a shorter wake results in a slight starting vortex as a completely steady state is not yet reached. Increasing the wake size drastically decreases this starting vortex. In turn this means that once the aircraft undergoes an acceleration, the larger wake will have more information on the flow history before this acceleration. This will reduce the influence of the acceleration. While a wake size of 4 wingspans yields almost no starting vortex, the wake size of 2 spans is not far off. Based on this it is expected that the effect of the shorter wake on the results is not that large, such that a wake size of 2 wingspans can be used.

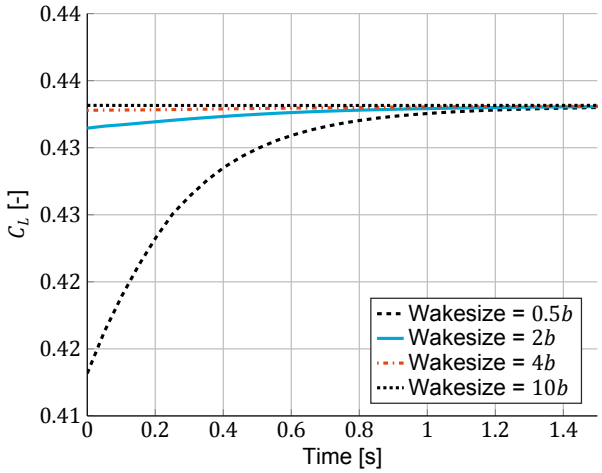

Figure 5.1: The value of C_L over time as a function of wake size.

5.1. Effect of time-delay in gust velocities

To see the effect of the time delay in the gust modelling, some simulations were performed to compare the adapted gust model with the original implementation (see also Subsection 2.2.2). The simulations were performed with a short and a long gust. The short gust has a semilength of $H = 10$ m, while the long gust has a semilength of $H = 150$ m. Both gusts have a gust velocity of $W_g = 13$ m/s, and both gusts were positioned 50 metres from the aircraft starting point. Note that these simulations were all performed with the QS aerodynamic model, such that a direct comparison between them can be made.

Figure 5.2 and Figure 5.3 show the effect of the short and long gust on the aircraft loads. It is seen that the new gust implementation predicts a longer period of higher loads. This is expected behaviour, as the aircraft undergoes the effect of the gust for a longer time in the new gust implementation. With the short gust, a more distinct behaviour can be seen. The two distinct peaks in this case are the gust hitting the wing, and secondly the gust engulfing the horizontal tail. For the longer gust this effect is less distinct, as the gust is larger than the distance between the wing and tail. Another observation is that the peak wing root bending moments are higher with the new gust model. This can be attributed to the fact that at first, only the wing is influenced by the gust instead of the whole aircraft. This causes a force concentration on the wing, whereas in the old model the whole aircraft would be moved upwards, reducing the magnitude of the wing root forces.

Looking at the flight mechanics response (Figure 5.4 and Figure 5.5) some interesting behaviour is seen. First of all, the pitch angle between the gust models shows a completely different behaviour. Using the new model with the short gust, it is seen that the aircraft pitches up at first. This pitch up is due to the gust hitting the wing of the aircraft first, such that there is no counter-balance from the tail yet. Once the gust only hits the tail, the aircraft starts pitching down again. This behaviour can also be seen in the longer gust, with the peak less distinct due to the gust hitting all parts of the aircraft at some moment in time.

From these results, it can be concluded that a time-delay gust model can lead to a very different aircraft response, both in loads and flight mechanics.

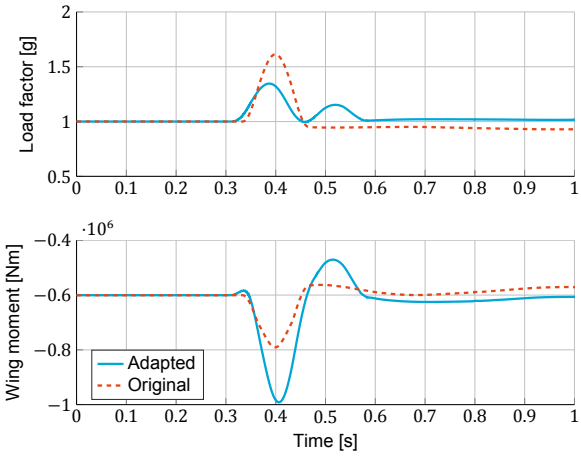

Figure 5.2: Loads of the short gust ($H = 10$ m), with the original and adapted gust implementation.

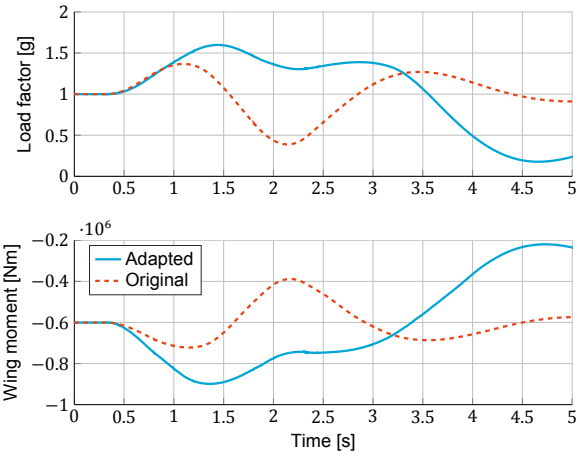

Figure 5.3: Loads of the long gust ($H = 150$ m), with the original and adapted gust implementation.

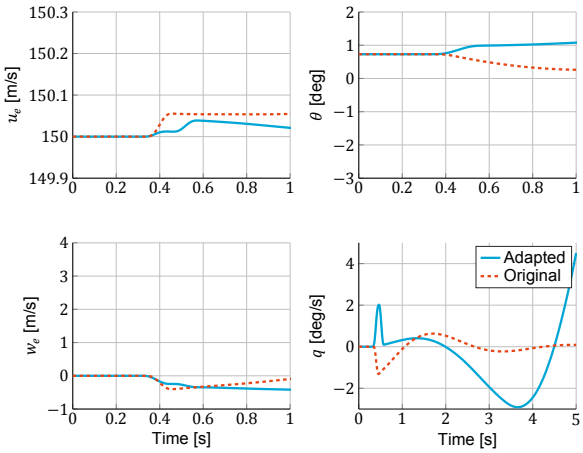

Figure 5.4: Flight mechanics response of the short gust ($H = 10$ m), with the original and adapted gust implementation.

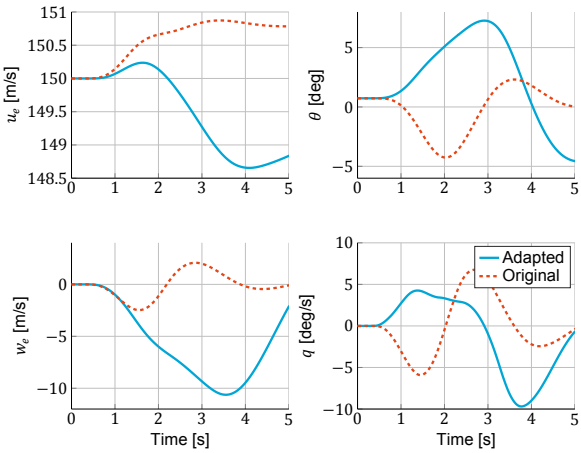

Figure 5.5: Flight mechanics response of the short gust ($H = 150$ m), with the original and adapted gust implementation.

5.2. Trim results

All simulations start from a trimmed state, meaning that only very small accelerations are present in the aircraft model (both in the wing movement and the aircraft flight mechanics). This state is achieved with a certain control vector, which is different for each aircraft and each aerodynamic model. For this reason, the control vectors used to trim the simulation cases are presented here. The target for the accelerations is $\epsilon = 10^{-3}$, meaning that small accelerations are allowed.

In Table 5.1 the control deflections required for trim are shown for all models under consideration. In the table, QS stands for quasi-steady (i.e., the original aerodynamic model). The difference between the QS model and the UVLM is shown for both the rigid wings, and the flexible wings. Note that a positive elevator deflection means a downward deflection.

Looking at the rigid aircraft, it is seen that the required elevator deflection is quite different between the two aerodynamic models. This difference led to a further investigation of elevator deflection versus flight speed. The results can be seen in Figure 5.6. This calculation was performed for the rigid wing, and shows that both the QS model and the UVLM follow the same trend of elevator deflection versus speed. There is thus an offset in required elevator deflection in both models. The reason for this is sought in the difference in pitching moment prediction between both aerodynamic models, causing an offset in the required elevator deflection for horizontal flight. Comparing the required thrust, it is observed that the UVLM required quite a bit less thrust. This can be explained by the fact that drag

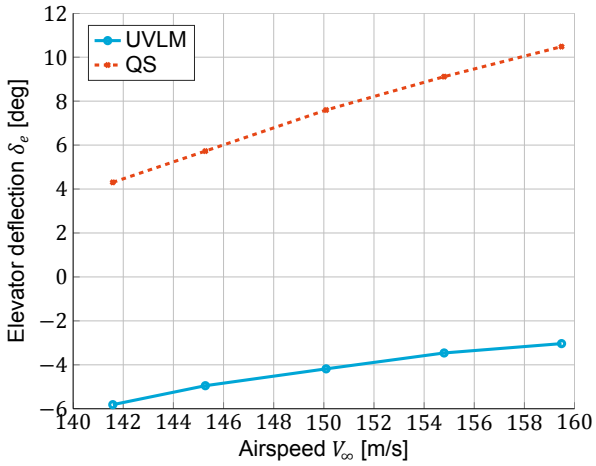

Figure 5.6: The required elevator deflection for trim versus airspeed, for the rigid wing.

is underpredicted in the UVLM. Finally, the difference in trimmed pitch angle is relatively small. This difference stems from the difference in pitching moment, leading to a different aircraft orientation for a force balance.

Moving to the flexible aircraft, it seen that there is a very small difference between the rigid and flexible wing under the quasi-steady aerodynamic model. This is expected, as the flexible wing is still relatively stiff. Comparing the rigid and flexible wing with the UVLM, the differences are also small. The comparison between both flexible wings show the same trends as the rigid wings, which is what one would expect. Again, a negative elevator deflection is required, as well as a lower thrust setting. The trimmed pitch angle is seen to be slightly higher compared to the QS model.

Table 5.1: Control deflections required for trim.

	Rigid, QS	Rigid, UVLM	Difference [%]	Flexible, QS	Flexible, UVLM	Difference [%]
δ_e [deg]	4.1391	-3.91	-194.6	4.3188	-4.313	-199.9
δ_T [kN]	43.5299	36.630	-15.85	43.5377	36.63	-15.9
θ [deg]	0.7772	1.21	56.47	0.7294	0.99	35.9

Table 5.2 shows the accelerations of the degrees of freedom after trim. It can be seen that they are well within the tolerance set on the accelerations for the QS model. Both UVLM wings are trimmed using the autopilot approach, which requires a relatively long computational time. For this reason, the trim tolerance has been increased slightly. As the intended simulations (i.e., the gusts) are of short duration, this is expected to not have a large impact on the results. Moreover, it should be noted that during this autopilot trim both aircraft deviated slightly from the intended altitude of $h = 11$ km.

Table 5.2: Accelerations after trim procedure.

	Rigid, QS	Rigid, UVLM	Flexible, QS	Flexible, UVLM
$\dot{q}$ [rad/s^2]	$-6.31 \cdot 10^{-8}$	$-3.06 \cdot 10^{-2}$	$-3.56 \cdot 10^{-11}$	$1.94 \cdot 10^{-3}$
$\dot{u}$ [m/s^2]	$-1.05 \cdot 10^{-7}$	$4.78 \cdot 10^{-3}$	$3.35 \cdot 10^{-10}$	$1.03 \cdot 10^{-2}$
$\dot{w}$ [m/s^2]	$-4.11 \cdot 10^{-8}$	$-1.05 \cdot 10^{-3}$	$4.70 \cdot 10^{-13}$	$2.51 \cdot 10^{-2}$

Finally, the wing vertical deflection in the trimmed state is compared between both aerodynamic models, and is shown in Figure 5.7. As seen, there is a slight difference in the wing tip deflections, with the UVLM resulting in a larger deflection. This is expected, as it was found in Subsection 4.4.3 that the lift predicted by the UVLM is slightly larger than that predicted by the QS model. In Figure 5.8 the wing

twist distribution is seen. It is observed that there is a larger difference between the models in this case. The UVLM leads to a downwards twist, whereas the QS aerodynamic model predicts a wavy upwards twist distribution.

To find the reason for this, a closer look is taken at the lift and pitching moment distributions on the wing. This is shown in Figure 5.9 and Figure 5.10. It can be seen that indeed the lift is predicted higher in the UVLM, leading to the higher wing deflection. The pitching moment distribution shows another picture, with the QS model predicting a larger moment than the UVLM. This causes the wing to twist downwards with the UVLM, albeit slightly. In order to explain the waviness found with the QS model, a look is taken at the position of wing attachables. The landing gear, flaps and engine are all attached in the region of the first peak. The landing gear and flap lie behind the elastic axis, thus twisting the local wing sections upwards. The engine weight does the opposite, but the engine thrust results in an upwards twist as well. Knowing that thrust is less with the UVLM, this leads to a difference in twist distribution. The second peak near the wing tip is the location of the ailerons, which are also located behind the elastic axis. This causes the wing to twist upwards. Together with the larger pitching moment, the overall effect is an upwards twist of the wing. It should be noted that the twist angles are very small, and as such are not expected to play a large role in the gust response.

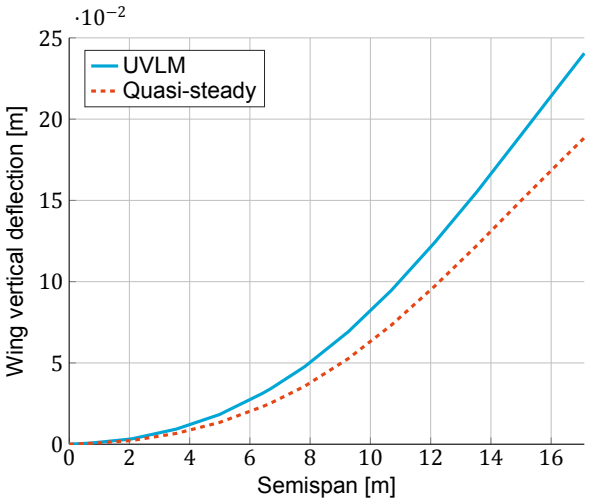

Figure 5.7: Trimmed wing vertical deflection for the quasi-steady and the unsteady aerodynamic model.

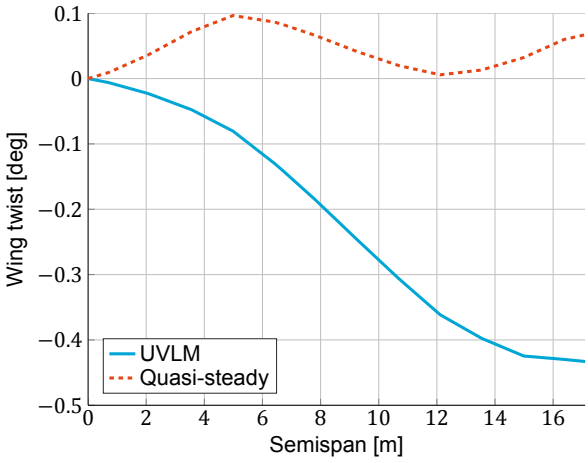

Figure 5.8: Trimmed wing twist for the quasi-steady and the unsteady aerodynamic model.

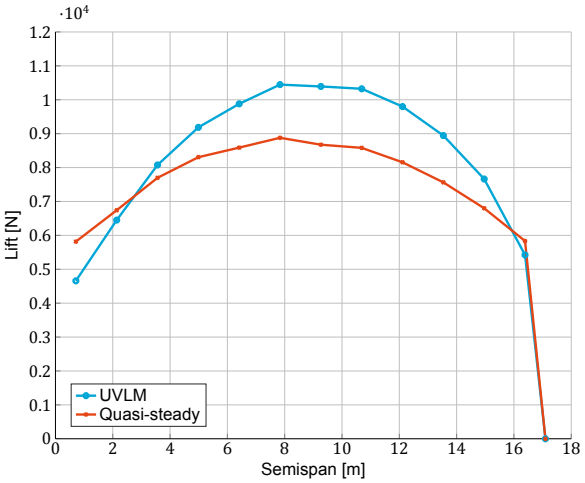

Figure 5.9: Lift distribution for the trimmed wings.

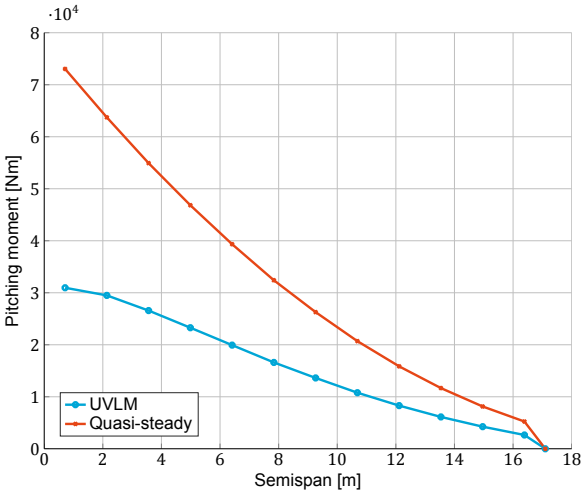

Figure 5.10: Elastic axis pitching moment distribution for the trimmed wings.

5.3. Gust response

Due to the large amount of data generated by the gust simulations, only a few of the results are shown in this chapter (though all data is used for the discussion). The figures shown here are for the shortest ($H = 5$ m) and the longest ($H = 107$ m) gust. The rest of the figures can be found in Appendix C, however some summary figures are presented here as well. The results and their discussion are separated in the loads acting on the aircraft (Subsection 5.3.1), the flight mechanics response (Subsection 5.3.2), and the wing tip deflection (Subsection 5.3.3). Note that the time scales on the plots are different, depending on the gust length.

5.3.1. Aircraft loads

Figure 5.11 and Figure 5.12 show the aircraft load factor n and the wing root bending moments for the shortest and the longest gust. During this analysis the offset in wing root bending moment between the QS model and the UVLM is not looked at, as this stems from the difference in modelling the forces. Instead, the behaviour is analysed for any differences. However, a quick overview of load factor peak as a function of gust length is shown Figure 5.13.

Starting with the load factor n, the first observation is that the UVLM predicts higher load factor peaks. This can be explained by the fact that the UVLM predicts the lift peaks to be higher as well, directly leading to a larger load factor (as $n = L/W$). More interesting is the location of these load peaks. For the short gust, it can be clearly observed that the load peaks stemming from the UVLM occur at a later stage than those stemming from the quasi-steady aerodynamic model. For the long gust, this phase shift is not as visible. This is also shown in Figure 5.14, where the phase shift of the maximum load factor is compared for different gust lengths. The rigid wing with the QS aerodynamic model is used as a baseline. It is thus seen that for shorter gusts the unsteady effects (i.e. time history of the flow) play a larger role, which can be expected because the time history embedded in the wake is much larger in comparison to the longer gust. This phase difference is seen to gradually become smaller compared to the gust period, for increasing gust length. This phase shift is only significant for the shortest gust, and mostly for the rigid wing. Overall the effect of the phase shift is less than 5%. While the UVLM shows a difference in results for the flexible and rigid wing, this is not seen as significantly for the QS model. This is attributed to the fact that the flexible wing movement has an effect on the aerodynamic forces. The history of this movement is taken into account using the UVLM, leading to a difference in results for the rigid and flexible wing. In the QS model the history of the wing movement is not used to calculate the aerodynamic forces.

It is also seen that the the load factor starts to rise earlier with the UVLM. This is due to modelling the gust hitting the complete wing geometry with the UVLM, compared to only wing section nodes located at the elastic axis location with the QS model. A difference can also be observed between the start of the peaks for the rigid and flexible wing with the UVLM. This can be attributed to a difference in flight velocity, such that the rigid wing reaches the gust at a later point in time.

Finally, looking at the behaviour of the wing root bending moment it is seen that in general the second peak is lower with flexible wings. This is due to a damping effect of the wings. For the shortest gust, this effect is not observed as the flexible wing has a larger second peak. Moreover, it is seen that the QS model predicts the wing root bending moment to move back to its steady-state value after the gust, while the UVLM predicts a slower return to the steady-state value. Again, this is due to the wake.

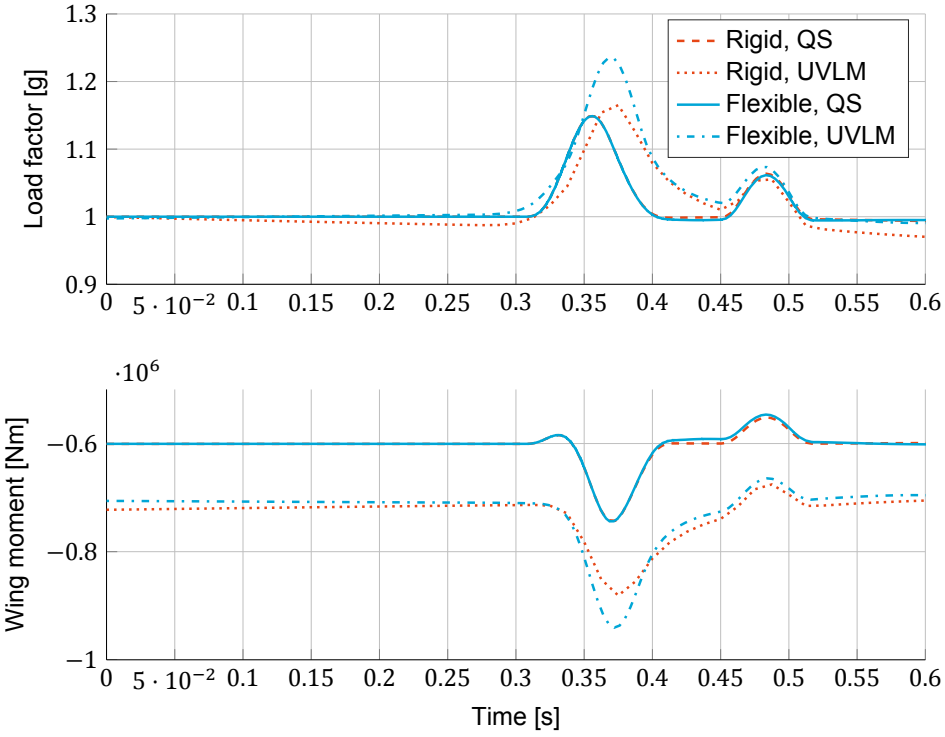

Figure 5.11: The aircraft load factor, and wing root bending moment for a gust of $H = 5$ m.

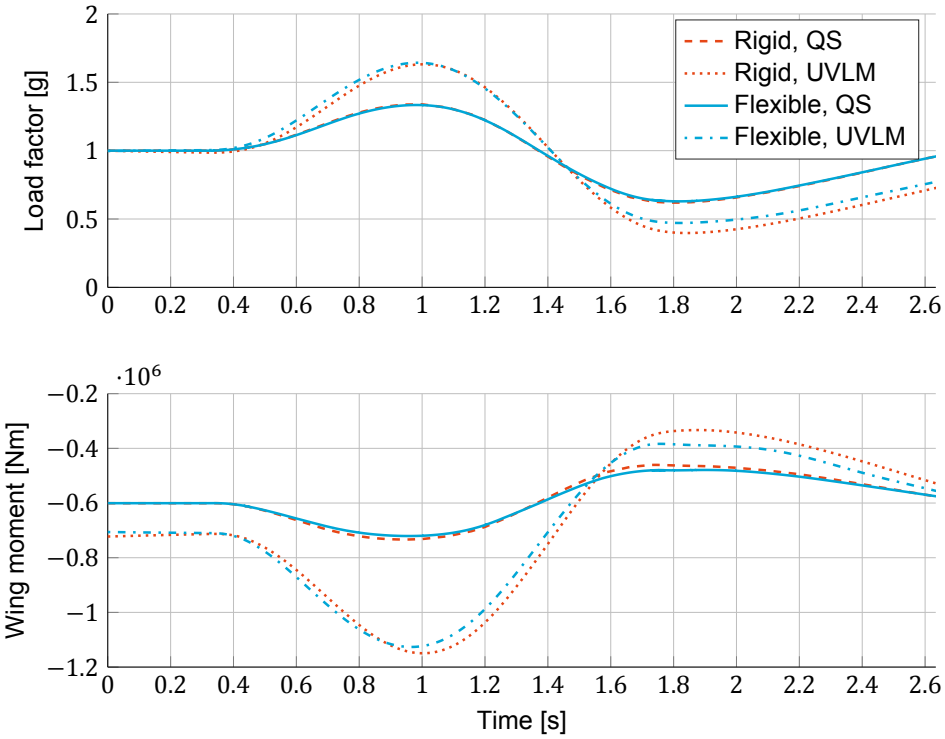

Figure 5.12: The aircraft load factor, and wing root bending moment for a gust of $H = 107$ m.

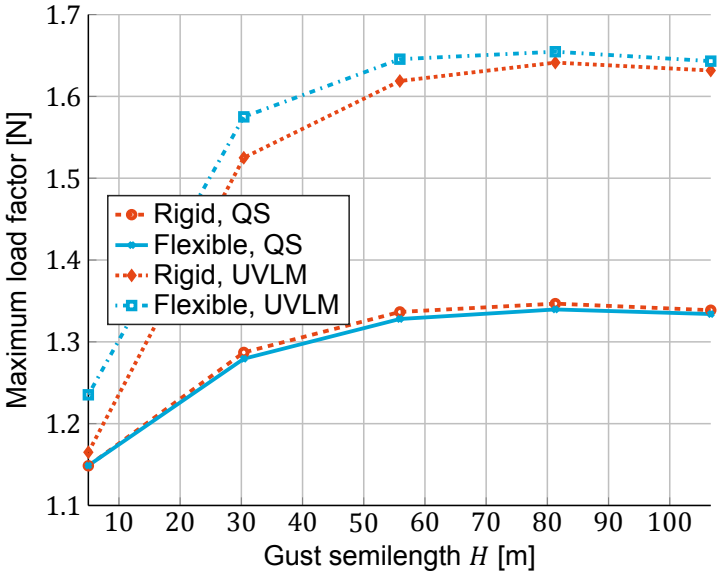

Figure 5.13: The load factor peaks as a function of gust length.

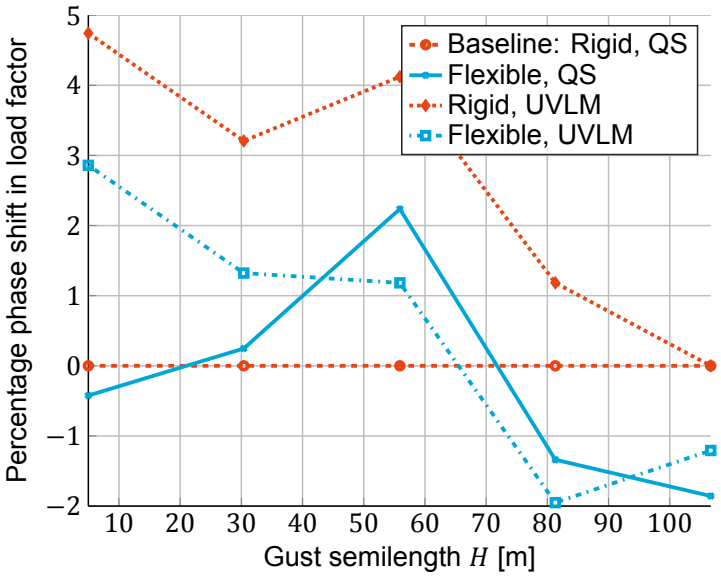

Figure 5.14: The percentage change in phase shift of the load factor peak as a function of gust length. The baseline is the rigid wing with the quasi-steady aerodynamic model.

5.3.2. Aircraft flight mechanics

The flight mechanics response (u, w, θ and q) is shown in Figure 5.15 and Figure 5.16 for the short and the long wake, respectively. It should be noted that in this case a positive w is a downwards velocity. Moreover, note that the UVLM aircraft do not start from the same point as the quasi-steady aircraft. This is due to the higher tolerance allowed for trimming with the UVLM. For this reason, the respective behaviours will be analysed instead of absolute values.

The first observation is related to pitch angle θ and pitch rate q. It is seen that in all cases the gust time-delay effect is present. First the aircraft pitches up (only the front of the wing engulfed in the gust), after which it pitches down due to the gust hitting the horizontal tail and the complete wing. It is also observed that the UVLM predicts the aircraft to pitch up earlier. This is due to modelling the gust time-delay over the complete chord, instead of at one point as is done with the QS model. Moreover, a phase shift in the response of pitch can also be observed. Again, this is due to the wake modelling slowing down the growth of lift over time. Next to the phase shift, not much difference is found between the QS model and the UVLM.

Next the vertical and horizontal velocity, as well as altitude and true airspeed are analysed (see Figure 5.17 for the longest gust; the other gusts are shown in Appendix C). The first observation is that the aircraft increases its altitude more when modelled using the UVLM. This is attributed to the fact that the UVLM predicts lift to be larger than the QS model. Another slight contribution to the altitude increase is due to modelling the complete wing in a chordwise sense using the UVLM. This leads to the aircraft being engulfed in the gust slightly longer. The altitude increase is also seen to be larger in the rigid aircraft for both models, which is expected behaviour as the flexible wings take up part of the gust energy by bending. This same behaviour can be seen for all gust lengths, but the QS model predicts the difference between the rigid and flexible wings to be much smaller. The larger increase in altitude for rigid wings is also shown in the vertical velocity, with the rigid wings achieving a larger upwards velocity due to the gusts. This directly translates into a higher altitude, and shows in both models.

Moving on the the true airspeed, and the horizontal velocity (in the inertial frame) it can be seen that both models show a very different behaviour. While the behaviour is different, the overall change in both models' velocity is about 0.2% meaning that it is insignificant in the overall aircraft response. A likely explanation for the different behaviour between both aerodynamic models is the difference in trim solution, together with the modelling of the complete wing. This causes the UVLM solution to pitch up earlier (as the wake hits the leading edge of the wing). This pitch up movement changes the direction of the forces (the horizontal contribution of thrust becomes slightly less, together with a slightly increased drag) that causes the aircraft to slow down slightly. This is not seen with the QS model, as the wing is modelled at the elastic axis, leading to a much lower pitch up tendency.

A final observation for the flight velocity and altitude is that small gusts have no observable effect on this. Only with longer gusts it is seen that the overall aircraft flight path is affected, instead of only the motion of the aircraft around its centre of gravity.

5.3.3. Wing tip deflection

For the wing tip deflection, only the two flexible aircraft are compared. Figure 5.18 and Figure 5.19 show the wing tip deflection and twist for the short and long gust, respectively. The other gusts are shown in Appendix C. It should be noted that the start position of the wing tip is different due to the different aerodynamic models, leading to different trimmed states. This offset will be taken into account when analysing the results.

The first and foremost observation that can be made is the larger amplitude of tip deflection found using the UVLM. This can be explained by the fact that the peaks in lift are predicted larger with the UVLM compared to the QS model. In the UVLM the wing tip also deflects slightly earlier than the QS model. This is due to the modelling of the gust delay of the complete wing, instead of only the spanwise sections as is done in the QS model. Looking at the behaviour of the tip deflection, it is seen that the wing tip deflects upwards after hitting the gust. After the gust, the wing tip oscillates back towards its trimmed position. This is shown for both aerodynamic models, with the UVLM leading to larger amplitudes.

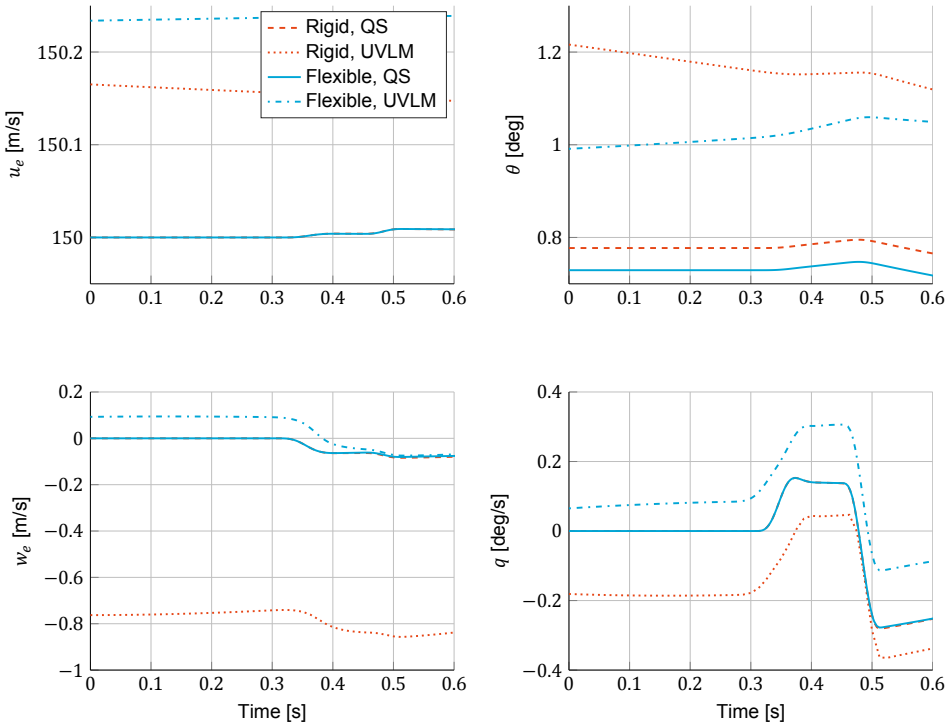

Figure 5.15: The flight dynamics response, in terms of horizontal, vertical velocity, pitch angle and pitch rate for a gust of $H = 5$ m.

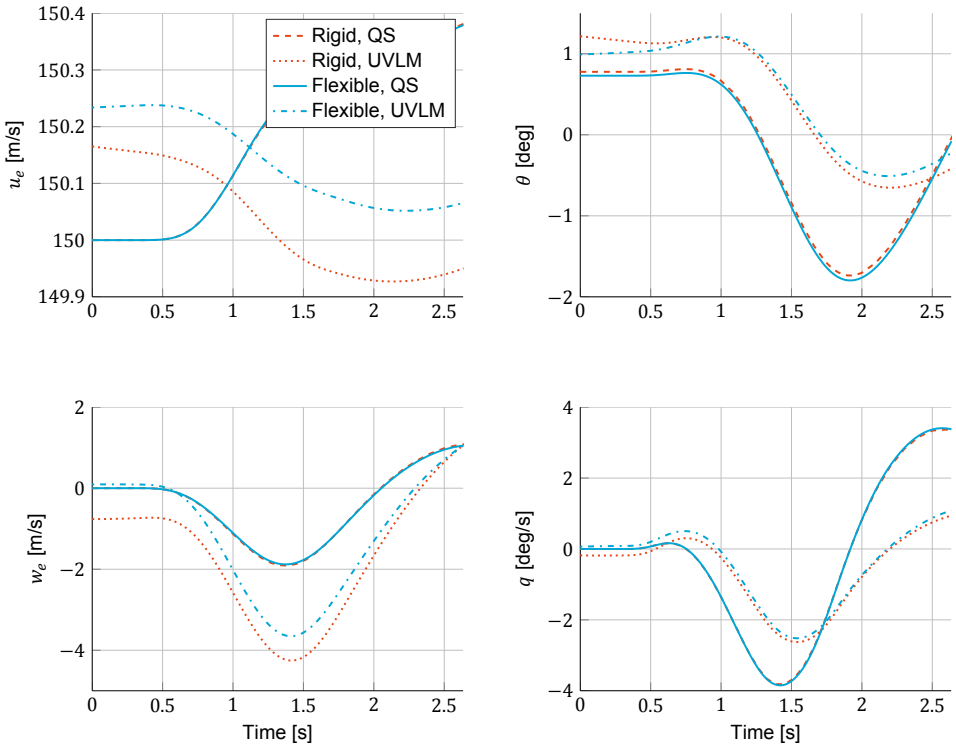

Figure 5.16: The flight dynamics response, in terms of horizontal, vertical velocity, pitch angle and pitch rate for a gust of $H = 107$ m.

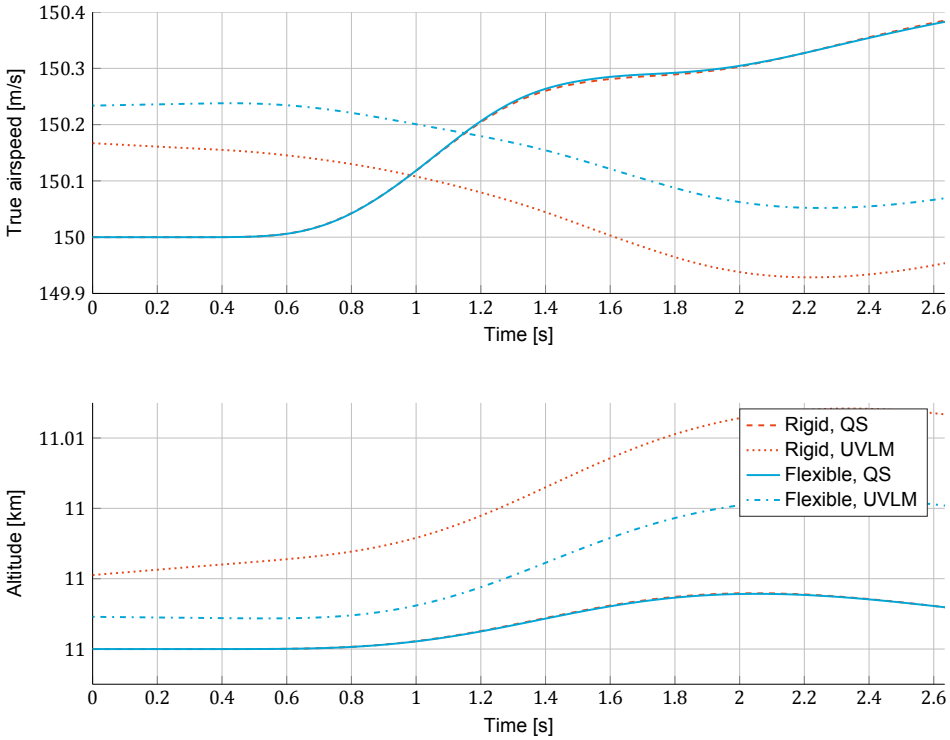

Figure 5.17: The true airspeed V_∞ and altitude h for a gust of $H = 107$ m.

Interestingly, the phase difference found in previous results is much less visible compared to these previous results. This can be explained by, again, the modelling of the complete wing. This causes the wing to be hit by the gust at an earlier point in time, offsetting the time-delay in the force response. This leads to a UVLM tip deflection behaviour that almost coincides with that of the QS model.

Moving on to the wing tip twist, the UVLM again shows a higher magnitude response. This is because aerodynamic twist happens partly because of aeroelastic twist, which is larger in the UVLM due to the larger force prediction. Moreover it is seen that once the gust hits the wing the wing twist is oriented opposite that at a later time. The time-delay effect of the gust thus influences the wing twist over time. This is mostly apparent with shorter gusts, but the effect is present for the longer gusts as well.

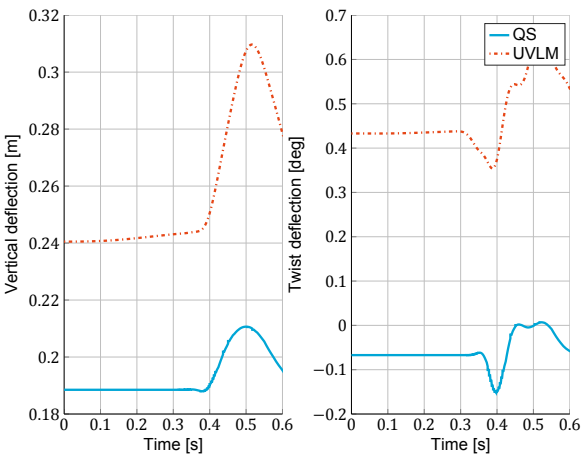

Figure 5.18: The wing tip vertical deflection and twist over time, for a gust of $H = 5$ m.

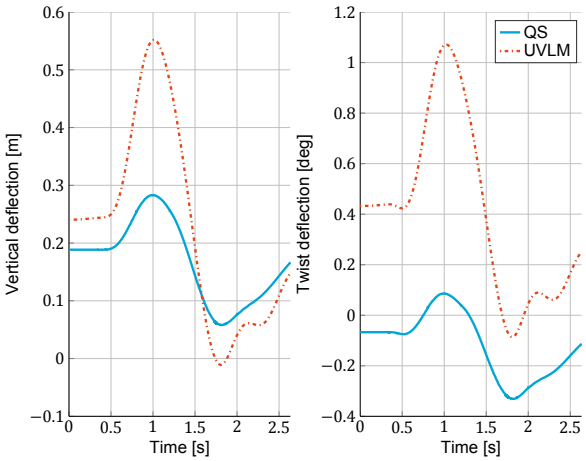

Figure 5.19: The wing tip vertical deflection and twist over time, for a gust of $H = 107$ m.

5.3.4. Summary

It was seen that modelling with the UVLM leads to larger loads and, in turn, to larger responses in terms of altitude, pitch and wing root bending moments. This larger response is attributed to the modelling difference between the QS aerodynamic model and the UVLM, and is not a function of the unsteady aerodynamics. This larger load prediction also showed in the attained altitude and vertical velocity during the gust, which was much larger with the UVLM.

What is a function of the unsteady aerodynamics is the time behaviour of the aircraft over the gust. It was seen that there is a phase shift in the loads acting on the aircraft with the UVLM. This phase shift was expected, as unsteady aerodynamics include the time-history of the flow. Due to this, the increase in aerodynamic forces is not instant, but is delayed by the wake trailing the aircraft. This causes a shift in the time for the loads to peak, with the most apparent example the shorter gusts. The phase shift was also present in the aircraft response in terms of pitch and vertical velocity. It was found that the phase shift in load factor is not more than 5% at the most critical case, so it is a small effect.

In the pitch angle and pitch rate reaction, the enhanced wing modelling of the UVLM showed. As the UVLM models the gust hitting the wing from leading edge to trailing edge, instead of only at the elastic axis, the pitch behaviour of the aircraft will change compared to the QS model. This was mostly seen in a tendency for a pitch up behaviour at the start of the gust, where parts of the wing lying in front of the center of gravity are hit. This effect is much less pronounced with the QS model. While all other parameters showed similar behaviour between the two models, the true airspeed showed a completely different behaviour between the QS model and the UVLM. While different, the actual change in velocity was not significant with it being about 0.2%.

Finally, it was seen that the rigid and flexible wings modelled with the QS model do not differ much in their respective responses. The difference between rigid and flexible wing with the UVLM is more profound. This is due to taking into account the time-history of the motion of the flexible wing with the UVLM, influencing the results over a longer period of time. In the QS model the flexible wing velocity is taken into account directly, without any history associated with the movement.

Looking at Table 5.3 it is seen that the computational times of the UVLM are much larger than those of the QS model. So much so, in fact, that the model can not be used for conceptual design where many aircraft concepts need to be analysed. This computational time is due to three things. First, the UVLM adds a large number of equations especially with a large wake. Secondly, the UVLM is used with a fixed timestep due to the wake being pre-allocated and dependent on the amount of timesteps. The fixed timestep is set based on the high frequency motions, which are only present after a disturbance. Finally, the connection of the UVLM to Simulink increases the computational time drastically compared to that of the standalone MATLAB implementation. This is due to the compilation to C through MATLAB, making the implementation slower.

Table 5.3: Computation times for the gust of length $H = 107$ m.

Case	Rigid, QS	Rigid, UVLM	Flexible, QS	Flexible, UVLM
Time [min]	0.2	88.4	0.7	275.1

5.4. Elevator pulse response

Figure 5.20 shows the response of the different aircraft after an elevator impulse of 1 second, starting at 1 second into the simulation. This simulation has been performed to showcase other capabilities of the tool, instead of just the gust response.

Right away, it is observed that there is a significant difference between the QS model and the UVLM results in terms of flight speed V_∞ and altitude h. For an explanation, one first needs to look at the pitch angle θ. Here it is seen that the UVLM predicts a lower pitch angle. This is due to the UVLM predicting a smaller absolute value of the pitching moment, such that the same elevator pulse amplitude has a stronger effect, compared to the QS model. It takes the aircraft a longer time to recover from this

Table 5.4: Period of the short period motion in seconds.

Rigid, QS	Rigid, UVLM	Difference [%]	Flexible, QS	Flexible, UVLM	Difference [%]
2.31	2.76	19.5	2.40	2.75	14.6

negative pitch angle (at around 15 seconds the pitch angle is zero again) This causes the aircraft to fly downwards for a longer time, leading to a larger trade-off between potential and kinetic energy.

Looking at pitch rate q, it is seen that the UVLM shows a phase shift. At first the downwards pitch rate is much larger with the UVLM, due to the lower prediction of pitching moment. After this first peak, a phase shift is seen in the pitch rate. Again, this is due to the time-history embedded in the wake trailing the aircraft. In Table 5.4 the period of the short period motion is shown. It can be seen that there is a difference of around 18% between the QS model and the UVLM, with the UVLM predicting a longer period. This difference is explained by the phase-shift in the aerodynamic forces, such that there is a slight delay between angle of attack change and force change, leading to a longer period.

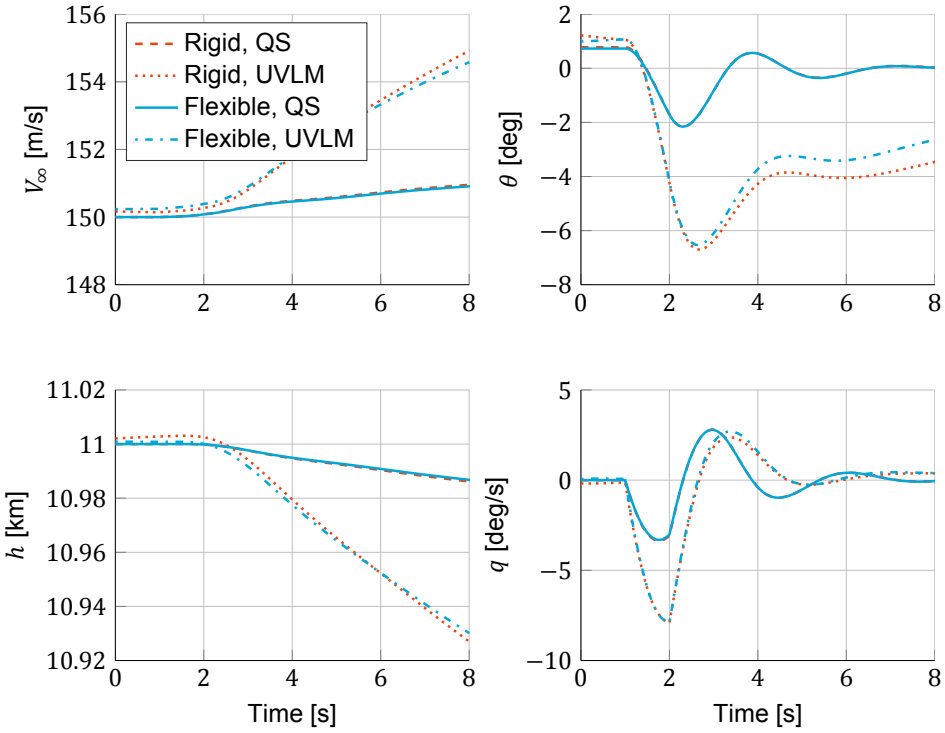

Figure 5.20: The aircraft response (in term of V_∞, h, θ and q) after an elevator impulse of 1 second.

6

Conclusions and recommendations

This chapter will summarise the work performed in this report, and draw conclusions based on this work. This is done in Section 6.1. Next to the conclusions, some recommendations for future work are presented in Section 6.2.

6.1. Conclusions

In this work the role of unsteady aerodynamics in flight mechanics of flexible aircraft is investigated. In particular the gust response of such aircraft is analysed. For this reason an unsteady aerodynamic model in the form of the unsteady vortex lattice method was constructed. This aerodynamic model has been coupled to a flexible aircraft flight mechanics toolbox to investigate the effect of unsteady aerodynamics on the flight mechanics. An updated trim algorithm was also implemented, to trim the aircraft with the unsteady aerodynamic model. This is done using a wake trim algorithm, and an autopilot trim implementation.

In order to investigate the gust response of flexible aircraft, a gust model was developed. This model is a spatial gust model, allowing the modelling of the gust time-delay effect. This means that different parts of the aircraft are hit by the gust at different times. The gust response was chosen as a case-study to assess the effect on unsteady aerodynamics on the flight mechanics of flexible aircraft. Next to this, a study on the response after an elevator pulse was performed.

In Chapter 1 a research objective was posed for the current work, which was divided into two main objectives, and one secondary objective:

- Develop a fast and accurate unsteady aerodynamic model by means of the unsteady vortex lattice method.
- Couple the aerodynamic model with the aeroelastic flight mechanics toolbox.
- Develop a discrete gust model that can model a gust acting on staggered parts of the aircraft at a different time, by means of a $1 - \cos$ gust model.

Starting with the first objective, it can be concluded that this is achieved albeit within limits. The behaviour of the model works as intended, in both steady and unsteady cases. This means that all trends predicted by the model are correct. Moreover, in the steady case the lift and induced drag are predicted correctly for low-swept wings of varying aspect ratio. Changes in taper were found to correctly change the lift distribution over the wing. However, some limitations on the applicability of the model were found. First of all, the model does not work for wings with a leading edge sweep larger than $30°$. For wings with larger sweep, the prediction of C_{L_α} is off by more than 20%, which is not acceptable. It was found that there is a steady decrease in the prediction of the lift-curve slope C_{L_α}, with increasing leading edge sweep angle. The error in C_{L_α} was found to follow a linear relation with the sweep angle, with a unit increase in sweep leading to a 2% larger error in C_{L_α}. Moreover, it was found that the induced drag is underpredicted by the model once unsteadiness is taken into account. For lower aspect ratio wings

($\mathcal{AR} < 8$), this underprediction is less than 15% but the error increases with increasing $\mathcal{AR}$. Finally, the pitching moment has a slight offset in reference location such that the location of aerodynamic center is predicted about 2% forwards of the actual location. The model was also seen to be relatively quick, with a calculation time of 3.4 minutes for a simulation of 5 seconds. This was performed with a discretisation large enough for an error of less than 1% in C_L compared to a more detailed grid. Concluding, the first objective has not been met completely in that the model is not accurate for all types of aircraft. For the conventional passenger aircraft, the objective is met. This is why the model is used as is.

Moving on to the second objective, it was found that this connection works as intended. The wing position (i.e. flightpath) and shape information (i.e. wing deflection) is correctly passed from the flight mechanics toolbox to the aerodynamic model. It was also seen that the aerodynamic model gives back the aerodynamic forces and moments at the correct position for the flight mechanics toolbox. Due to differences in the modelling of the forces with the new aerodynamic model, a proper conclusion between the magnitude of the forces of both models cannot be made. These differences were higher lift, lower drag and much lower pitching moment as predicted by the unsteady aerodynamic model. Even so, it can be said that the second objective of this thesis has been achieved as the differences in aerodynamic force do not stem from the connection between the two models.

The third objective is the gust model. This has been implemented in such a way that an aircraft can fly through a gust in space. This leads to a time-delay effect, where the gust hits the tail at a later time than parts in front of the aircraft. This was seen to be implemented correctly. It was found that this can have a profound effect on the flight dynamics of the aircraft, especially for shorter gusts. As at first only the wing is hit by the gust, there is a tendency for a pitch-up motion at first using this model. Furthermore, it was seen that the loads acting on the wing are different using this implementation, as the aircraft is under influence of the gust for a longer time compared to the original gust model. Again, it can be concluded that this objective has been met.

With this, it can be concluded that the overall research objective of this work has been met. However, it should be noted that the objective of a fast aerodynamic model does not hold anymore once the aerodynamic model is coupled to the flight mechanics toolbox. Once this is done, the computational times increase drastically compared to the original aerodynamic model. This is due to the added amount of calculations, and memory usage due to compilation to C.

Next to the research objective a research question was posed in Chapter 1. This research question was divided into several sub-questions, repeated here:

- What is the difference between unsteady and quasi-steady aerodynamics on the gust response of a structurally flexible aircraft?
    1. Do the loads differ in magnitude?
    2. Do the maxima in loads occur at different times?
    3. At what gust length do unsteady aerodynamics become important?

With the current model it was not possible to answer sub-question 1. This is because the two aerodynamic models used differ too much in their load prediction. Because of this, it was not possible to see whether changes in force magnitude were due to unsteady effects, or because of differences in the force prediction of both models.

The second question can be answered. It was seen that unsteady aerodynamics lead to a phase shift in the loads acting on the aircraft. The peak loads occur at a later point in time. Also the behaviour of the aircraft in terms of its flight mechanics showed a phase shift in the response. The reason for this phase shift is the wake that is modelled in the unsteady aerodynamic model. This keeps information on the time-history of the flow, such that a dampened aerodynamic behaviour is shown. This means that the magnitude of the aerodynamic forces take time to reach their peak values, instead of instantaneously as shown in the quasi-steady aerodynamic model. This phase-shift was found be small, with a maximum difference of 5% for the phase-shift in load factor between the models.

For the third question, it was expected that very short gusts might require unsteady aerodynamics to accurately simulate their effect on the aircraft. From the results, it was found that this is not the case. While the relative size of the phase shift in aircraft response becomes larger with smaller gust lengths, the overall effect is not large enough to require unsteady aerodynamic modelling. Taking into account

the large computational times associated with the current unsteady aerodynamic model, it becomes even more decisive to use the original quasi-steady aerodynamic model to model the gust response of the aircraft.

The answer to the overall question is thus that unsteady aerodynamics lead to a phase shift in the aircraft loads, and the aircraft response. Moreover, for wings of relatively high stiffness unsteady aerodynamics is not required in calculating the gust response, as the effect of unsteady aerodynamics are very minor. It was found that unsteady aerodynamics leads to a different response for a flexible wing, compared to a rigid wing. It is expected that this difference becomes more important once more flexible wings are considered.

While not part of the research question, another case has been studied to prove other capabilities of the current work. The effect of unsteady aerodynamics on the aircraft response after an elevator pulse has been investigated. It was found that the period of the short period increases by about 18% with unsteady aerodynamic modelling. Again, this is due to the non-direct lift increase in unsteady aerodynamics. From this, it is concluded that for high frequency motions unsteady aerodynamics is important to take into account.

To summarise, an unsteady aerodynamic model has been implemented and validated to correctly predict the lift response for low-swept wings. This model has been coupled to a flexible flight mechanics toolbox, together with a spatial gust model such that staggered parts are acted upon by a gust at different points in time. This allows to study the gust response, and flight manoeuvre response of flexible aircraft under consideration of unsteady aerodynamics. Using this work the gust response of aircraft was studied, where it was found that unsteady aerodynamics are not required to model the gust response of flexible aircraft. Results have indicated that unsteady aerodynamic modelling is more important for more flexible wings. Note that the current work allows for simulating these more flexible wings, in both longitudinal and lateral motion. Moreover, the current work allows for modelling more flexible wings as well and paves a way to perform control law design.

6.2. Recommendations

As research is an ongoing process, the work presented in this report can be improved and added to. To guide the direction for these improvements and additions, this section presents the recommendations the author deems most important. This is divided into several subjects:

- Aerodynamic model
- Connection between tools
- Decreasing computational time
- Extending modelling capabilities

Aerodynamic model

First of all, the aerodynamic model can be improved in several ways. One addition would be improving the model such that highly swept wings can be modelled accurately. This will extend the capabilities of the modelling framework. Moreover, the pitching moment calculation needs to be looked at, as the model currently predicts the aerodynamic center slightly forwards. As a starting point, the assumption of the force attachment point on the leading edge of the vortex rings should be looked at.

Another improvement to the model is a better implementation of the drag calculation. At the moment, induced drag is underpredicted. A possibile solution is to calculate drag using a Trefftz plane analysis. For this one needs to implement a plane downstream of the wing, parallel to the local freestream and then integrating the v and w component of the wake in this plane [54]. Furthermore, a different method of accounting for zero-lift drag can be added. This could be an engineering method such that the aerodynamic model itself can account for differences in geometry, instead of requiring external information. This will make the model more self-contained.

Connection between tools

Secondly the connection between the aerodynamic model and the flight mechanics toolbox can be improved. Due to the fact that the aerodynamic model is implemented as a MATLAB function, it needs to be compiled to C/C++ to work with Simulink. This brings with it several undesired traits. First, matrices need to be bounded with a maximum size, such that the compiler can allocate sufficient memory. During compiling, the compiler can not yet see the values of certain variables, such that some of the upper bounds on the matrices need to be hardcoded. This should be investigated in further detail to take out the hardcoded upper bounds. Secondly, the author has of yet not found a compiler that works with Windows with the current aerodynamic model, as all Microsoft compilers throw an error when pre-allocated matrices take up more than 4 GB of space. Some research on the compilers for Windows is thus still required. A possible solution would be to see if the aerodynamic model can be implemented using Simulink blocks, but this would require a new aerodynamic model. Another option is to look into the state-space representation of the model, as set out in [21].

Next to the compiler issues, memory usage itself leaves to be desired. While working fine as a standalone MATLAB program, once compiled to C/C++ through MATLAB the memory usage of the program increases drastically. For this reason it might be desirable to change the vortex ring calculation code to use a looped form instead of a matrix form. While this may be slower, running out of memory limits the length of the wake and the size of the aerodynamic grid.

Decreasing computational time

Another recommendation is on the computational side of the work. At present the aerodynamic model works with a fixed timestep such that all wake panels have an equal size. As seen in the results of the work, this leads to large computational times making the aerodynamic model not ideal for the conceptual design stage. It should thus be investigated whether the aerodynamic model can be made compatible with variable timestep ordinary differential equations (ODE) solvers. In this way much time can be saved as the computation can switch to larger timestep when reaching a steady state. A possible solution would be to implement a calculation to scale the vortex strength of a wake panel if this panel changes its size.

A different way in which the timesteps might be changed is moving to a different integration scheme. At the moment it is a first-order Euler integration, but higher order schemes might be more stable allowing for a larger timestep (which might result in lower computational time). This has been done before, such as a fourth-order integration method [70], or a predictor-corrector method [71].

An additional procedure of speeding up the aerodynamic model is the implementation of a better wake truncation method. As the wake influence diminishes with distance, it is possible to implement a separate method to calculate the wake influence in the far-field. This can for example be done using vortex particles [72]. Finally, it is possible to implement the UVLM more efficiently by not calculating the influence of vortex lines multiple times. As the vortex lines in spanwise direction share the same strength in finding the aerodynamic influence coefficients, it is possible to re-use the data from a calculations.

Extending modelling capabilities

The work presented here can be extended to model more of the aircraft then just the wings. Currently, the empennage and control surfaces are modelled using aerodynamic look-up tables. It is, however, possible to model these using the unsteady vortex lattice method. In this way it is also possible to model the effect of the empennage on the wing and vice versa using the aerodynamic influence coefficients. Naturally, this will increase computational time. Also, extra care should be taken that the wake of the wing does not cross that of the tail, as this can lead to discontinuities in the solution [16].

The control surfaces can be implemented in the UVLM by locally deflecting the aerodynamic calculation grid. This changes the normal vector of the local vortex rings, as well as their local angle of attack. In such a way the forces acting on these parts will change. Such a control deflection has already been implemented by Elham [11] in a steady vortex lattice method, and this implementation can be ported to the UVLM.

Another extension is to model wing/fuselage interactions. At the moment the UVLM does not know that there is a fuselage. In reality the wing does see an influence of the presence of a fuselage and this can be modelled. For example, this has been done in [73] by modelling every surface as a lifting surface, and as such giving each surface a vortex ring.

Bibliography

[1] I. E. Garrick and W. H. Reed III, *Historical Development of Aircraft Flutter,* Journal of Aircraft **18**, 897 (1981).

[2] W. R. Krüger, *A multi-body approach for modelling manoeuvring aeroelastic aircraft during preliminary design,* Proceedings of the Institution of Mechanical Engineers, Part G: Journal of Aerospace Engineering **222**, 887 (2008).

[3] M. J. Patil, D. H. Hodges, and C. E. S. Cesnik, *Nonlinear Aeroelastic Analysis of Complete Aircraft in Subsonic Flow,* Journal of Aircraft **37**, 753 (2000).

[4] A. L. da Silva, P. Paglione, and T. Yoneyama, *Conceptual Flexible Aircraft Model for Modeling, Analysis and Control Studies,* in *AIAA Atmospheric Flight Mechanics Conference*, Guidance, Navigation, and Control and Co-located Conferences No. August (American Institute of Aeronautics and Astronautics, 2010).

[5] M. Bianchin, G. Quaranta, and P. Mantegazza, *State space reduced order models for static aeroelasticity and flight mechanics of flexible aircraft,* Proceedings of the XVII Congresso Nazionale AIDAA (2003).

[6] D. K. Schmidt and D. L. Raney, *Modeling and Simulation of Flexible Flight Vehicles,* Journal of Guidance, Control, and Dynamics **24**, 539 (2001).

[7] J. Xu, *Aircraft Design With Active Load Alleviation and Natural Laminar Flow*, Ph.D. thesis, Stanford University (2012).

[8] E. Torenbeek, *Development and Application of a Comprehensive, Design-sensitive Weight Predicition Method for Wing Structures of Transport Category Aircraft*, Tech. Rep. (Delft University of Technology, Delft, 1992).

[9] G. J. Kennedy and J. R. R. A. Martins, *A parallel aerostructural optimization framework for aircraft design studies,* Structural and Multidisciplinary Optimization , 1079 (2014).

[10] J. Xu and I. Kroo, *Aircraft Design with Maneuver and Gust Load Alleviation,* in *AIAA Applied Aerodynamics Conference*, June (Honolulu, 2011) pp. 1–15.

[11] A. Elham and M. J. L. van Tooren, *Beyond Quasi-Analytical Methods for Preliminary Structural Sizing and Weight Estimation of Lifting Surfaces,* in *56th AIAA/ASCE/AHS/ASC Structures, Structural Dynamics, and Materials Conference*, AIAA SciTech No. January (American Institute of Aeronautics and Astronautics, 2015) pp. 1–19.

[12] R. L. C. Kalthof, *Multibody Dynamics Modeling of Flexible Aircraft Flight Dynamics*, Tech. Rep. (Delft University of Technology, Delft, 2014).

[13] T. Kier, *Comparison of Unsteady Aerodynamic Modelling Methodologies with Respect to Flight Loads Analysis,* in *AIAA Atmospheric Flight Mechanics Conference and Exhibit* (2005) pp. 1–14.

[14] R. Clark and E. H. Dowell, *A Modern Course in Aeroelasticity*, A Modern Course in Aeroelasticity (Springer, 2004).

[15] J. Wright and J. Cooper, *Introduction to Aircraft Aeroelasticity and Loads*, 1st ed., Aerospace Series (Wiley, 2008).

[16] J. Murua, *Flexible Aircraft Dynamics with a Geometrically-Nonlinear Description of the Unsteady Aerodynamics*, Ph.D. thesis, Imperial College London (2012).

[17] H. Wagner, *Über die Entstehung des dynamischen Auftriebes von Tragflügeln,* ZAMM-Journal of Applied Mathematics and Mechanics/Zeitschrift für Angewandte Mathematik und Mechanik **5**, 17 (1925).

[18] H. G. Küssner, *Zusammenfassender Bericht über den instationären Auftrieb von Flügeln,* Luftfahrtforschung **13**, 410 (1936).

[19] T. Theodorsen, *General Theory of Aerodynamic Instability and the Mechanism of Flutter,* NACA Tech. Report (1935).

[20] J. G. Leishman, *Challenges in Modeling the Unsteady Aerodynamics of Wind Turbines,* 21st ASME Wind Energy Symposium and the 40th AIAA Aerospace Sciences Meeting **132**, 1 (2002).

[21] J. Murua, R. Palacios, and J. M. R. Graham, *Applications of the unsteady vortex-lattice method in aircraft aeroelasticity and flight dynamics,* Progress in Aerospace Sciences **55**, 46 (2012).

[22] R. N. Yurkovich, D. D. Liu, and P.-C. Chen, *The State-of-the-Art of Unsteady Aerodynamics for High Performance Aircraft,* Proceedings of the 39th AIAA Aerospace Sciences Meeting & Exhibit (2001), doi:10.2514/6.2001-428.

[23] D. A. Peters, S. Kuranamoorthy, and W. M. Cao, *Finite State Induced Flow Models Part I : Two-Dimensional Thin Airfoil,* Journal of Aircraft **32** (1995).

[24] D. A. Peters, *Finite State Induced Flow Models Part II : Three-Dimensional Rotor Disk,* Journal of Aircraft **32**, 323 (1995).

[25] R. Palacios, J. Murua, and R. Cook, *Structural and Aerodynamic Models in Nonlinear Flight Dynamics of Very Flexible Aircraft,* AIAA Journal **48** (2010), 10.2514/1.J050513.

[26] E. Albano and W. P. Rodden, *A doublet-lattice method for calculating lift distributions on oscillating surfaces in subsonic flows.* AIAA Journal **7**, 279 (1969).

[27] T. E. Fritz and L. N. Long, *Object-Oriented Unsteady Vortex Lattice Method for Flapping Flight,* 42nd AIAA Aerospace Sciences Meeting **41**, 1275 (2004).

[28] B. a. Roccia, S. Preidikman, J. C. Massa, and D. T. Mook, *Modified Unsteady Vortex-Lattice Method to Study Flapping Wings in Hover Flight,* AIAA Journal **51**, 2628 (2013).

[29] B. K. Stanford and P. S. Beran, *Analytical Sensitivity Analysis of an Unsteady Vortex-Lattice Method for Flapping-Wing Optimization,* Journal of Aircraft **47**, 647 (2010).

[30] K. Seywald, F. Hellmundt, A. Wildschek, and F. Holzapfel, *Airworthiness Investigation of a Highly Nonplanar Flexible Wing Concept,* in *29th Congress of the International Council of the Aeronautical Sciences* (St. Petersburg, 2014) pp. 1–10.

[31] L. Cavagna, P. Masarati, and G. Quaranta, *Coupled Multibody/Computational Fluid Dynamics Simulation of Maneuvering Flexible Aircraft,* Journal of Aircraft **48**, 92 (2011).

[32] P. C. Chen, Z. Zhang, and E. Livne, *Design-Oriented Computational Fluid Dynamics-Based Unsteady Aerodynamics for Flight-Vehicle Aeroelastic Shape Optimization,* AIAA Journal , 1 (2015).

[33] J. A. Mulder, W. H. J. J. van Staveren, J. C. van der Vaart, E. de Weerdt, C. C. de Visser, A. C. in 't Veld, and E. Mooij, *Flight Dynamics*, Tech. Rep. (Delft University of Technology, Delft, 2013).

[34] G. J. J. Ruijgrok, *Elements of Airplane Performance*, 2nd ed. (VSSD, Delft, 2009).

[35] L. Meirovitch and I. Tuzcu, *Unified Theory for the Dynamics and Control of Maneuvering Flexible Aircraft,* AIAA Journal **42**, 714 (2004).

[36] R. D. Milne, *Dynamics of the deformable aeroplane* (HM Stationery Office, 1964).

[37] M. J. Patil and D. H. Hodges, *Flight Dynamics of Highly Flexible Flying Wings,* Journal of Aircraft **43**, 1790 (2006).

[38] C. M. Shearer and C. E. S. Cesnik, *Trajectory Control for Very Flexible Aircraft,* Journal of Guidance, Control, and Dynamics **31**, 340 (2008).

[39] R. J. Simpson and R. Palacios, *Numerical aspects of nonlinear flexible aircraft flight dynamics modeling,* in *54th AIAA/ASME/ASCE/AHS/ASC Structures, Structural Dynamics, and Materials Conference* (2013) pp. 1–25.

[40] M. Drela, *Integrated Simulation Model for Preliminary Aerodynamic, Structural, and Control-Law Design of Aircraft,* 40th AIAA Structures, Structural Dynamics and Materials Conference , 1644 (1999).

[41] M. R. Waszak and D. K. Schmidt, *Flight Dynamics of Aeroelastic Vehicles,* Journal of Aircraft **25**, 563 (1986).

[42] W. R. Krüger and M. Spieck, *Aeroelastic Effects in Multibody Dynamics,* Vehicle System Dynamics **41**, 383 (2004).

[43] EASA, *Certification Specifications for Large Aeroplanes CS-25*, Tech. Rep. September (European Aviation Safety Agency, 2008).

[44] T. E. Noll, J. M. Brown, M. E. Perez-davis, S. D. Ishmael, G. C. Tiffany, and M. Gaier, *Investigation of the Helios Prototype Aircraft Mishap,* Volume I Mishap Report **I**, 100 (2004).

[45] K. J. Fidkowski, F. Engelsen, K. E. Willcox, and I. M. Kroo, *Stochastic gust analysis techniques for aircraft conceptual design,* in *12th AIAA/ISSMO Multidisciplinary Analysis and Optimization Conference*, September (2008) pp. 1–16.

[46] S. J. Hulshoff, *AE4930 Aeroelasticity*, Tech. Rep. 11.1 (Delft University of Technology, Delft, 2011).

[47] J. Zeng, J. Wang, R. D. Callafon, and M. Brenner, *Suppression of the Aeroelastic/Aeroservoelastic Interaction Using Adaptive Feedback Control Instead of Notching Filters,* in *AIAA Atmospheric Flight Mechanics Conference* (Portland, 2011) pp. 1–20.

[48] E. Livne, *Integrated Aeroservoelastic Optimization: Status and Direction,* Journal of Aircraft **36**, 122 (1999).

[49] S. Haghighat, J. R. R. A. Martins, and H. H. T. Liu, *Aeroservoelastic Design Optimization of a Flexible Wing,* Journal of Aircraft **49**, 432 (2012).

[50] C. Nam, A. Chattopadhyay, and Y. Kim, *Optimal wing planform design for aeroelastic control,* AIAA Journal **38**, 1465 (2000).

[51] R. P. Harper and G. E. Cooper, *Wright Brothers Lectureship in Aeronautics: Handling Qualities and Pilot Evaluation,* in *AIAA / AHS / ASEE Aircraft Design Systems and Operations Meeting* (1984).

[52] M. Van Dyke, *An album of fluid motion*, An Album of Fluid Motion (Parabolic Press, 1982).

[53] J. D. Anderson, *Fundamentals of Aerodynamics*, Anderson series (McGraw-Hill, 2011).

[54] J. Katz and A. Plotkin, *Low-Speed Aerodynamics*, 2nd ed., Cambridge Aerospace Series (Cambridge University Press, 2001).

[55] R. D. Finck, *United States Air Force Stability and Control DATCOM*, Tech. Rep. (McDonnel Douglas Corporation, 1978).

[56] J. Roskam, *Airplane Design: Part I-VIII*, Airplane Design (DARcorporation, 1985).

[57] E. Torenbeek, *Synthesis of Subsonic Airplane Design: An Introduction to the Preliminary Design of Subsonic General Aviation and Transport Aircraft, with Emphasis on Layout, Aerodynamic Design, Propulsion and Performance* (Springer, 1982).

[58] N. P. M. Werter, R. De Breuker, and M. M. Abdalla, *Continuous-time state-space unsteady aerodynamic modelling for efficient aeroelastic load analysis,* IFASD 2015: 16th International Forum on Aeroelasticity and Structural Dynamics , 1 (2015).

[59] J. Murua, R. Palacios, and J. M. R. Graham, *Assessment of Wake-Tail Interference Effects on the Dynamics of Flexible Aircraft,* AIAA Journal **50**, 1575 (2012).

[60] J. Murua, H. Hesse, R. Palacios, and J. M. R. Graham, *Stability and Open-Loop Dynamics of Very Flexible Aircraft Including Free-Wake Effects,* in *52nd AIAA Structures, Structural Dynamics, and Materials Conference*, April (2011).

[61] I. H. Abbott and A. E. Von Doenhoff, *Theory of Wing Sections, Including a Summary of Airfoil Data*, Dover Books on Aeronautical Engineering Series (Dover Publications, 1959).

[62] R. L. Halfman, *Experimental Aerodynamic Derivatives of a Sinusoidally Oscillating Air-foil in Two-Dimensional Flow,* NACA Technical Report 1108 , 1 (1952).

[63] D. P. Raymer, *Aircraft Design: A Conceptual Approach*, AIAA education series (American Institute of Aeronautics and Astronautics, 2012).

[64] M. Karpel and Z. Sheena, *Structural Optimization for Aeroelastic Control Effectiveness,* Journal of Aircraft **26**, 493 (1989).

[65] D. E. Raveh and M. Karpel, *Structural Optimization of Flight Vehicles with Computational-Fluid-Dynamics-Based Maneuver Loads,* Journal of Aircraft **36**, 1007 (1999).

[66] A. Elham, *Weight Indexing for Multidisciplinary Design Optimization of Lifting Surfaces*, Ph.D. thesis, Delft University of Technology (2012).

[67] H. Haddadpour and R. D. Firouz-Abadi, *Evaluation of quasi-steady aerodynamic modeling for flutter prediction of aircraft wings in incompressible flow,* Thin-Walled Structures **44**, 931 (2006).

[68] H.-g. Giesseler, M. Kopf, T. Faulwasser, P. Varutti, R. Findeisen, and M. P. Control, *Gust Load Alleviation Based on Model,* in *International Forum on Aeroelasticity and Structural Dynamics* (2013) pp. 1–18.

[69] É. Roux, *Avions civils à réaction*, 1st ed. (Éditions Élodie Roux, Blagnac, 2007).

[70] S. Y. Wie, S. Lee, and D. J. Lee, *Potential Panel and Time-Marching Free-Wake-Coupling Analysis for Helicopter Rotor,* Journal of Aircraft **46**, 1030 (2009).

[71] S. A. Dovgii and A. V. Shekhovtsov, *An Improved Vortex Lattice Method for Nonstationary Problems,* Journal of Mathematical Sciences **104**, 1615 (2001).

[72] D. J. Willis, J. Peraire, and J. K. White, *A combined pFFT-multipole tree code, unsteady panel method with vortex particle wakes,* International Journal for Numerical Methods in Fluids **53**, 1399 (2007).

[73] C. R. Kaykayoglu, *Application of the vortex lattice CFD method to obtaining aerodynamic predictions about wing/fuselage/pylon/store confiiguration including store separation,* 34th AIAA Aerospace Sciences Meeting (1996).

A

UVLM Implementation

This chapter is written to serve as a reference and manual for the UVLM that has been implemented in this thesis.

A.1. The unsteady vortex lattice method

The workings of the UVLM as implemented in MATLAB are shown in flowchart form in Figure A.1.

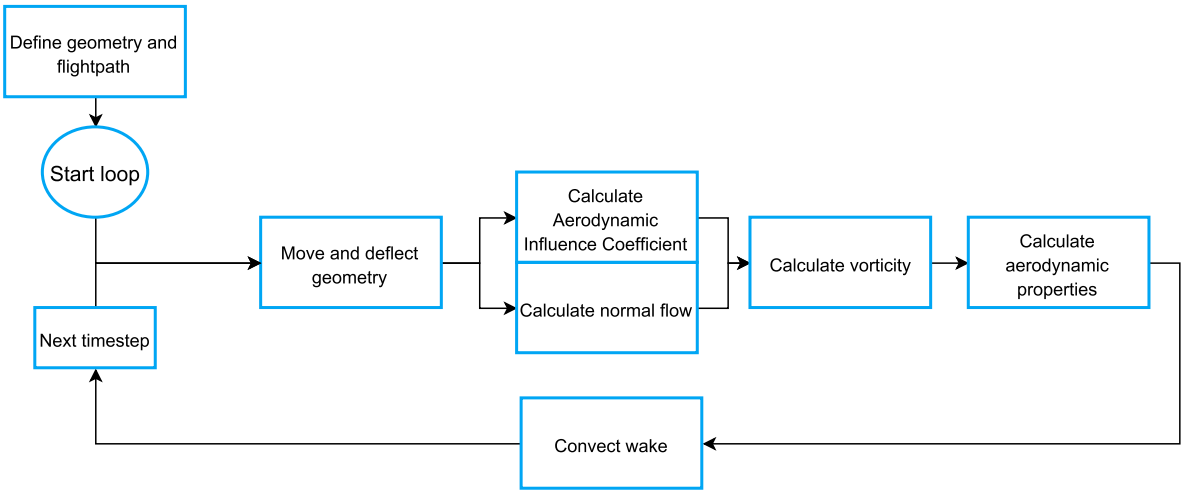

Figure A.1: Flowchart of the MATLAB implementation of the unsteady vortex lattice method.

A.1.1. Geometry and flightpath definition

In order to start the aerodynamic calculation the wing geometry needs to be defined. In the implementation this is done by means of set of cartesian coordinates for each of the wing panel corner points. These coordinates are specified in $\mathcal{E}_b$, and are transformed to the $\mathcal{E}_{eb}$ frame internally (i.e. set at the orientation angle with respect to the freestream velocity $\mathbf{V}_\infty$, such as angle of attack α).

Also the flightpath of the aircraft is to be specified, which includes both the position and the orientation of the $\mathcal{E}_b$ frame at each point in time. Moreover, the deflection of the wing within the $\mathcal{E}_b$ frame is to be either specified or taken from a structural calculation at each timestep n.

A.1.2. Calculation of vorticity

In order to get to the aerodynamic properties of the wing under consideration, first the vorticity of the flow field has to be solved. This is performed using the Biot-Savart law (Equation 3.11), repeated here for clarity:

$$\mathbf{q} = \frac{\Gamma}{4\pi} \frac{d\mathbf{l} \times \mathbf{r}}{r^3} \tag{A.1}$$

Here $\mathbf{r}$ is the vector between the point of evaluation and the mid-point of the vortex segment under consideration, while $d\mathbf{l}$ is the length of this vortex segment. Finally, Γ is the vortex strength of this vortex segment.

In order to find the influence of each wing vortex ring on each collocation point, the Biot-Savart law is evaluated for the combination of each vortex ring and each collocation point using a vorticity strength of $\Gamma = 1$ m^2/s. This gives a set of induced velocities $\mathbf{q}_{i,j}$ which, when multiplied with the normal vector of the corresponding collocation point $\mathbf{n}_{i,j}$, will give an aerodynamic influence coefficient AIC:

$$AIC_{i,j} = \mathbf{q}_{i,j} \cdot \mathbf{n}_{i,j} = (u, v, w)_{i,j} \cdot \mathbf{n}_{i,j} \tag{A.2}$$

The multiplication of this AIC with the local vortex strength value $\Gamma_{i,j}$ (still to be calculated) yields a flow velocity at the collocation point. At this point also BIC is calculated, which is the influence coefficient taking into account only the vortex lines parallel to the flight direction. This allows for calculating the induced drag at a later stage.

From the non-penetrating boundary condition present in potential flow theory, we know that the flow at the collocation point must be tangential to the surface. Since the collocation points all have a velocity (a combination of the flight velocity $\mathbf{V}_\infty$, velocity due to the wake $\mathbf{V}_w$, deformation velocity $\mathbf{V}_{def}$ and external velocity $\mathbf{V}_{ext}$) there is a condition to calculate Γ such that the local flow becomes tangential:

$$AIC_{i,j}\Gamma_{i,j} - RHS_{i,j} = 0 \tag{A.3}$$

$$RHS_{i,j} = \left(\mathbf{V}_\infty + \mathbf{V}_w + \mathbf{V}_{def} + \mathbf{V}_{ext}\right)_{i,j} \cdot \mathbf{n}_{i,j} \tag{A.4}$$

Since RHS is known (all velocities are know), as well as AIC one can readily solve for Γ. This can then be used for the calculation of the aerodynamic properties of the wing. It should be noted that these coefficients are calculated in the $\mathcal{E}_b$ frame.

A.1.3. Calculation of aerodynamic properties

With the vorticity at each collocation point known, one can calculate the pressure difference between the lower and upper surface of each collocation point. This is done by means of the unsteady Bernoulli equation, rewritten to yield lift of each panel (Equation 3.19), repeated here:

$$\Delta L_{i,j} = \rho \Delta b_{i,j} \left[\|\mathbf{V}_{m,n}\| \left(\Gamma_{i,j} - \Gamma_{i-1,j}\right) + \Delta c_{i,j} \frac{\partial}{\partial t} \left(\frac{\Gamma_{i,j} + \Gamma_{i-1,j}}{2} \right) \right] \cos \alpha_{i,j} \tag{A.5}$$

This lift depends on the panel chord- (Δc) and span-wise (Δb) lengths, and the local panel angle of attack α. This lift is calculated in each panel lift direction and thus has to be converted to the $\mathcal{E}_{eb}$ frame.

While lift is adequately predicted using the UVLM, induced drag is overpredicted as the method does not allow for leading-edge suction. This is due to the assumption of an infinitely thin wing [16]. Therefore, the induced drag is calculated differently [54]:

$$D_{i_{i,j}} = \rho \Delta b_{i,j} \left[(w_{ind} + w_{wake})_{i,j} \left(\Gamma_{i,j} - \Gamma_{i-1,j} \right) + \frac{\partial \Gamma_{i,j}}{\partial t} \Delta c_{i,j} \sin \alpha_{i,j} \right] \tag{A.6}$$

With w_{ind} the induced velocity due to the spanwise vortex lines (using BIC) and w_{wake} the induced velocity due to the wake.

Finally, the pitching moment can be calculated using the normal and tangential force, multiplied with the respective distance to the moment reference point. This moment reference point is normally the aerodynamic center position. The force attachment point is assumed at the leading edge of the respective vortex rings [16].

$$M_{i,j} = A_{i,j} z_{i,j} - N_{i,j} x_{i,j} \tag{A.7}$$

A.1.4. Solving the wake

Now that the aerodynamic loads and forces a known, the movement of the wake can be calculated. First, at each timestep a part of the wake will shed from the trailing edge of the wing (it will be located at the position of the trailing edge panels at the previous timestep). This shed wake will have the same vorticity strength as the trailing edge vortex panels at the previous timestep. After this, the vorticity will stay constant, due to the Helmholtz theorem. At each timestep, also the movement due to the aerodynamic flow field will be calculated. This is done by evaluating the Biot-Savart law for each wake vortex ring corner point, calculating the influence of both the wing and the wake itself. Also the external velocities such as gusts are added here. The development of this wake over time is illustrated in Figure A.2.

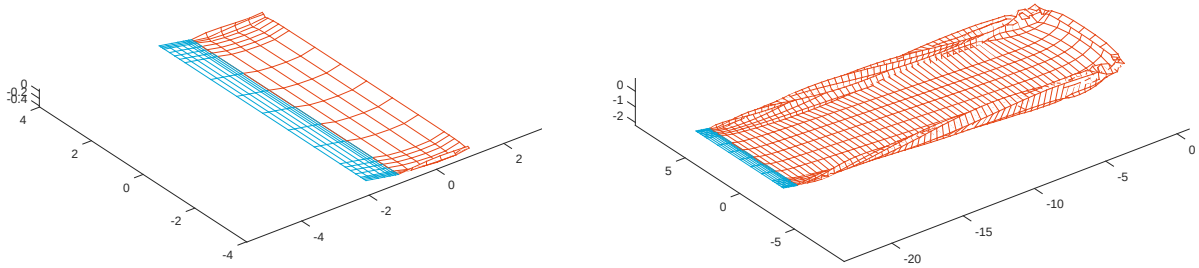

(a) Early timestep (b) Later timestep

Figure A.2: The wake propagation behind a planar, rectangular wing at an angle of attack of $\alpha = 10°$. All dimensions in meters.

A.2. User manual

This section serves as a user manual of the UVLM. It will detail on the steps required to run a calculation using the UVLM.

As a first step one needs to define the atmospheric conditions in which the calculation will take place. This is done in the `FlightParameters` struct. Secondly the flight path needs to be defined, which consists of a velocity and angular velocity for each timestep in the simulation. This is performed in the `FlightPath` struct. Moreover, the simulation parameters need to be defined which is performed using the `SimulationParameters` struct.

Naturally, a wing geometry is required for calculation of the aerodynamic parameters. This wing geometry is defined in the `GridParameter` struct, and consists of several grids: the normal wing grid,

the vortex grid and the collocation point grid. These grids can be generated using `ConstructGrids.m`.

The following tables show the parameters that should be included in each struct:

Table A.1: `FlightParameters`

Parameter	Unit	Variable name
Mach number	[-]	Mach
Altitude	[m]	altitude
GustParameters	[-]	Gust

Table A.2: `FlightPath`

Parameter	Unit	Variable name
Velocity (u, v and w for each timestep)	[m/s]	V
Angular velocity (p, q and r for each timestep)	[rad/s]	Vangle

Table A.3: `SimulationParameters`

Parameter	Unit	Variable name
Number of timesteps	[-]	n_time
Timestep	[s]	dt
Simulation time	[s]	simulation_time
GIF plot flag	[-]	plot_gif
Symmetry flag	[-]	Sym_Flag
Plot flag	[-]	plot

Once these structs are defined, it is possible to run the model. This is done using the function `UVLM`, which takes as input the previously defined structs. As output, the function returns the aerodynamic coefficients C_L, C_D and C_M. Moreover, the spanwise distribution of both lift and drag are returned. Finally, the function outputs a trim struct, that includes information on the wake. With this struct, it becomes possible to start a simulation with a wake already included such that the effect of a starting vortex is not present.

Naturally, this function can also be implemented in loops and other program flow types in order to calculate, for example, the lift-curve slope C_{L_α}. Several examples of such implementations can be found in the UVLM program folder.

Table A.4: `GridParameters`

Parameter	Unit	Variable name
Body frame wing grid (x, y, z)	[m]	Grid_B
Body frame vortex grid (x, y, z)	[m]	Vgrid_B
Body frame collocation grid (x, y, z)	[m]	Cgrid_B
Wing surface area	[m^2]	S

B

Additions to flight mechanics toolbox

During the course of this thesis, several additions to the flight mechanics toolbox have been made. This appendix will go over what has been added, and how these additions work.

B.1. Added functions

In this section the functions added to the FMT are summarised.

Trim

In order to trim the aircraft with the UVLM a new trim function has been made, consisting of several other functions. First is the main UVLM trim function: `aircraft_trim_uvlm`. This starts the trim procedure, and calls the function `uvlm_trim`. This function takes care of the trimming of the wake and also calls the autopilot trim function to get the aircraft to a steady state. This autopilot trim function is called `PID_trim`.

Finally, a function `unpack_uvlm_data` is added in order to gather the UVLM data (such as wake shape and strength) from the previous timesteps such that the trim algorithm can be used.

Aircraft builder and simulator

In order to use the FMT in conjunction with the UVLM two main FMT functions have a special UVLM version. This is the aircraft generator function `aircraft_generator_uvlm` and the aircraft simulator function `time_domain_simulation_uvlm`. In the aircraft generator function are input parameters that are required for the UVLM such as the number of chordwise panels, input for the wake shape and vorticity strength, and bound vorticity strength.

In the UVLM specific simulation function the solver is set to ODE1, with a fixed time-step such that there is a relatively constant wake panel length.

UVLM

Naturally the complete UVLM is also added in a separate folder. Several functions have also been added here to make the FMT and the UVLM compatible. These are the functions `POM2UVLM` which builds the aerodynamic grid from the wing section position and orientation, `ReorderForcesAndMoments` which reorders the aerodynamic forces in the order that the FMT expects them and the function `GetGridVelocity` that calculates the velocity of the individual grid points.

B.2. Added blocks

This section describes the blocks that are added to the FMT block library.

Spatial gust generator

The existing gust generator in the FMT is based on a time description of the gust, leading to the fact that at a certain point in time the complete aircraft sees the same gust velocity. This has been changed to a gust generator that takes as input the coordinates of the relevant aircraft and wake parts, and returns the gust velocity. The gust itself is defined in space at a certain location. This allows for modelling the time delay of an aircraft flying into a gust.

Some changes to the aircraft model are made to ensure that the positions of each aircraft part is send to the gust generator. This is done by extending the body sensors already present in these parts to also output the position in the inertial frame. These positions are send to the gust generator block, which returns a gust velocity for each wing section node (with the quasi-steady aerodynamic model) or each collocation point of the wing (with the unsteady vortex lattice method). Note that for the collocation points, several position measurement locations are added by means of hardcoded values. These should be changed accordingly, based on the amount of chordwise points n_c. This is done in the `Massless body UVLM Gust` block in the block library.

Changes to the aeroelastic nodes

Several additions and changes have been made to the aeroelastic nodes compared to the original FMT. These changes are invoked if one calls the `aircraft_generator_uvlm` script.

The first change is that the force and moment calculation block has been changed. Instead of having a look-up table for the aerodynamic forces, the UVLM is used. The aerodynamic forces are therefore passed directly to the frame conversion block using `From` tags. Secondly, each aeroelastic node has an extra sensor that is used to measure its position, orientation and motion which is used to build the aerodynamic grid needed for the UVLM.

UVLM block

Of course a UVLM block is also added. This will automatically be constructed and be put in the model once the `aircraft_generator_uvlm` script is called.

The UVLM is added to the FMT as a subsystem, in the form of a `MATLAB function` block. In this block the UVLM MATLAB code itself is included, as well certain inputs to the UVLM code. This is shown in Figure B.1.

Next to the UVLM are `DataStoreMemory` blocks that save the wake position (W_x, W_y, W_z), the wake vortex strength Γ_W (W_G), the bound vortex strength Γ_b (G), the orientation of the aircraft at the previous time-step ($\mathbf{\Omega}$), the right-hand side of Equation 3.15, a flag on whether $\partial\Gamma/\partial t < \epsilon$, with $\epsilon = 10^{-4}$ and a counter. The values stored in these memory blocks are read in by the `WakeIn` subsystem. They are subsequently updated by the UVLM after which they are stored back in memory through the `WakeOut` subsystem.

The Position, Orientation and Motion (POM) subsystem gets the POM from all wing sections using `From` tags and groups them together using a `Mux` block. These POMs are measured using a body sensor on the flexible wing sections, where it is measured at the elastic axis location. As output of the UVLM there are aerodynamic forces and moments. In the Forces and Moments subsystem, these values are separated for each flexible wing section, after which `Goto` tags pass these values to the aeroelastic blocks present in the FMT. Here the forces and moments are converted from the flexible wing frame of reference to that of the rigid wing, which is where all forces and moments are calculated. These converted forces are then send to a state-space calculation in order to update the wing position for the next time-step.

Inside the UVLM subsystem, there are more inputs for the UVLM MATLAB code. These are:

- **Simulation parameters**; number of time-steps n_t, simulation time t_{end}, the time-step dt,the current time t, a trim switch (i.e., is there a wake already) and a flag on whether the trim algorithm is run.

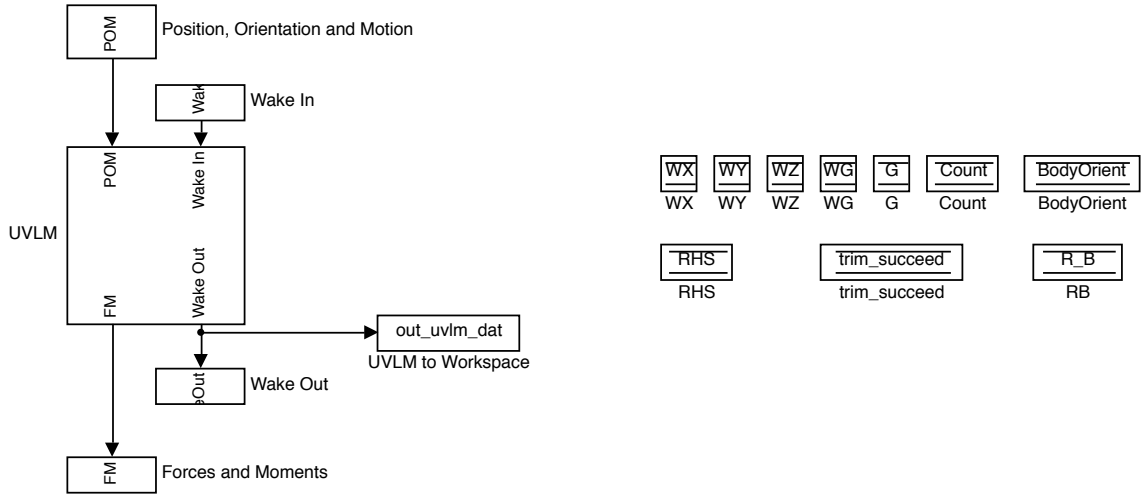

Figure B.1: The UVLM subsystem as included in the flight mechanics toolbox.

- **Atmospheric parameters**; temperature, density, pressure, speed of sound, dynamic viscosity, the aircraft position (x, y and z), the aircraft velocity (u, v and w), the aircraft rotation velocity (p, q and r), the aircraft angle of attack α_{rig}, and the rigid aircraft orientation Ω.
- **Wing input parameters**; number of spanwise sections n_s, wing semi span $b/2$, root chord c_r, tip chord c_t, wing area S, wing sweep Λ, wing sweep line Λ_{pos}, dihedral angle Γ, wing twist λ, incidence angle i, number of chordwise sections n_c, maximum values for C_l, C_d, C_m and the position vectors of the aircraft reference point $\mathbf{r}_{ac}$, the aircraft center of gravity position $\mathbf{r}_{cg}$ and the wing reference position $\mathbf{r}_{wing}$.
- **Wing section information**; outer chord of each section c_o, inner chord of each section c_i, elastic axis location of each section x_{ea} and aerodynamic center location of each section x_{ac}.
- **Gust parameters** Design gust velocity $W_{g_{ds}}$, gust semilength H, gust start position x_{gs}, minimum gust altitude $h_{g,min}$ and maximum gust altitude $h_{g,max}$.

Autopilot block

For the final trimming of the aircraft with the UVLM an autopilot block is used. This is a 2D autopilot working on the elevator and the thrust. It is added to the model is the input parameter `input_par.PID.on` is set to 1 before an aircraft model is generator (be it with `aircraft_generator` or `aircraft_generator_uvlm`).

C

Gust simulations

This appendix shows the remaining results of the gust simulations as analysed in Chapter 5.

C.1. Load factor and wing root bending moment

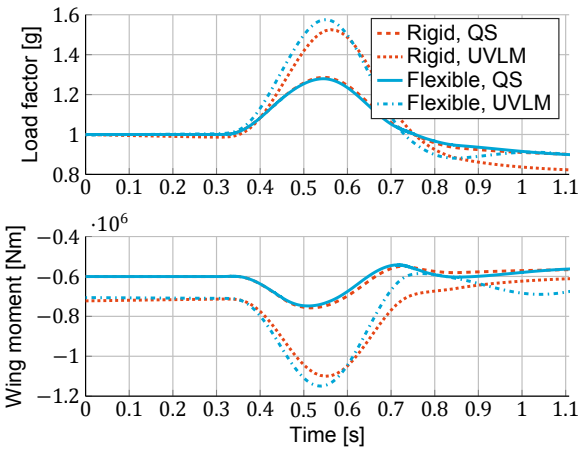

Figure C.1: The aircraft load factor, and wing root bending moment for a gust of $H = 31$ m.

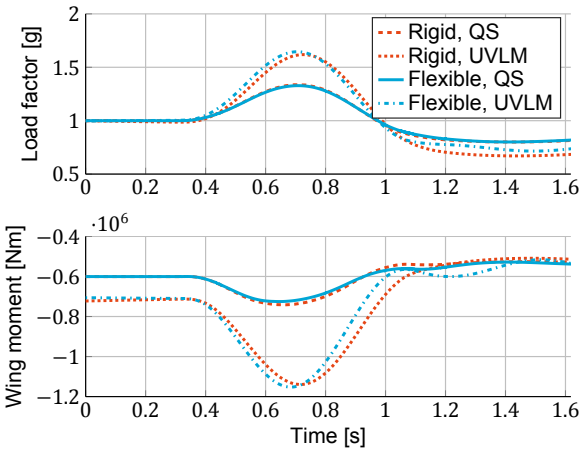

Figure C.2: The aircraft load factor, and wing root bending moment for a gust of $H = 56$ m.

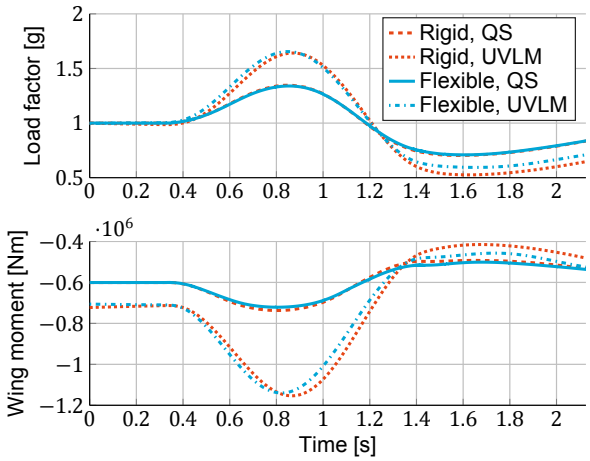

Figure C.3: The aircraft load factor, and wing root bending moment for a gust of $H = 82$ m.

C.2. Flight mechanics

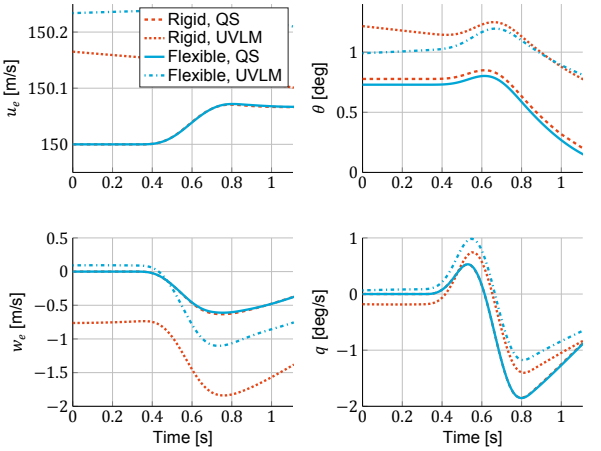

Figure C.4: The longitudinal flight mechanics parameters over time for a gust of $H = 31$ m.

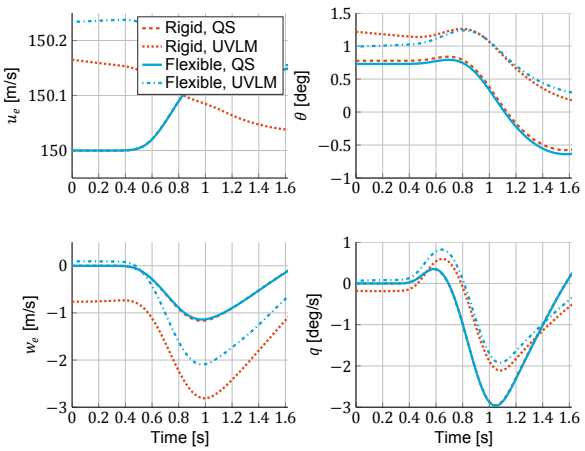

Figure C.5: The longitudinal flight mechanics parameters over time for a gust of $H = 56$ m.

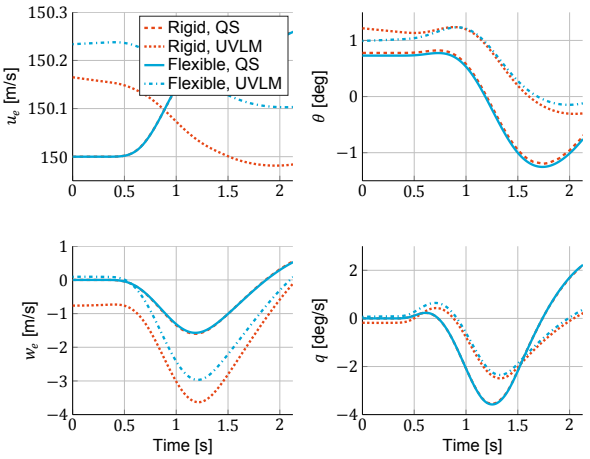

Figure C.6: The longitudinal flight mechanics parameters over time for a gust of $H = 82$ m.

C.3. Wing tip deflection

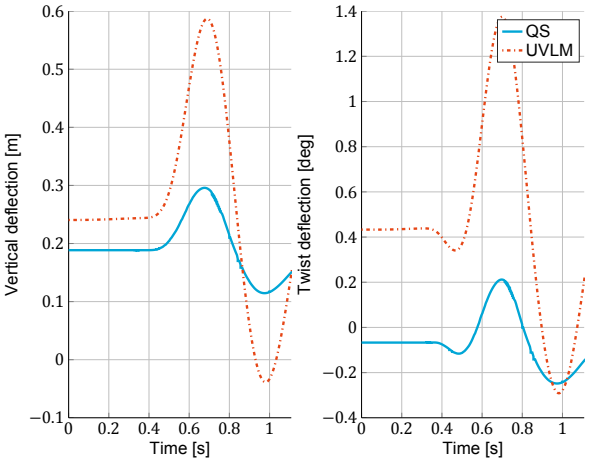

Figure C.7: The wing tip deflection and twist over time for a gust of $H = 31$ m.

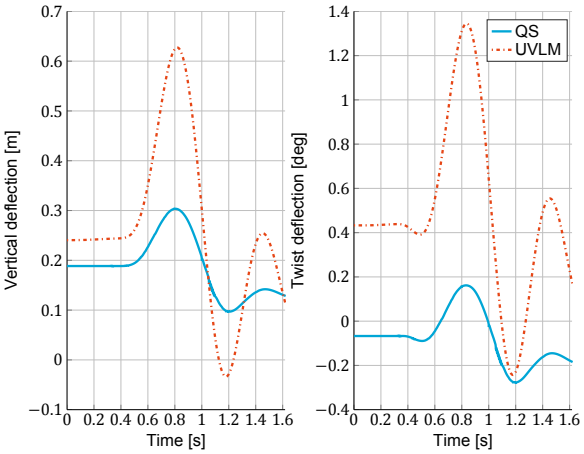

Figure C.8: The wing tip deflection and twist over time for a gust of $H = 56$ m.

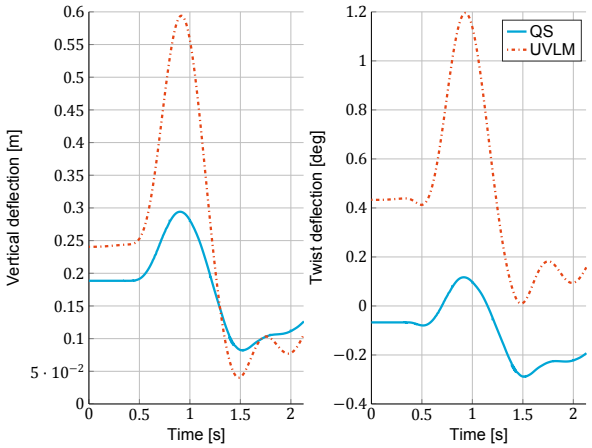

Figure C.9: The wing tip deflection and twist over time for a gust of $H = 82$ m.

C.4. Airspeed and altitude

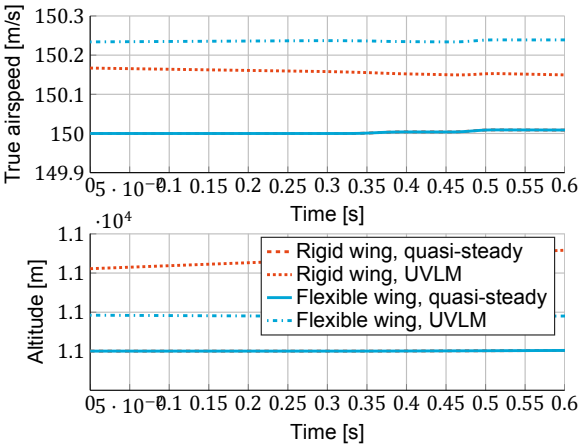

Figure C.10: The true airspeed V_∞ and altitude h for a gust of $H = 5$ m.

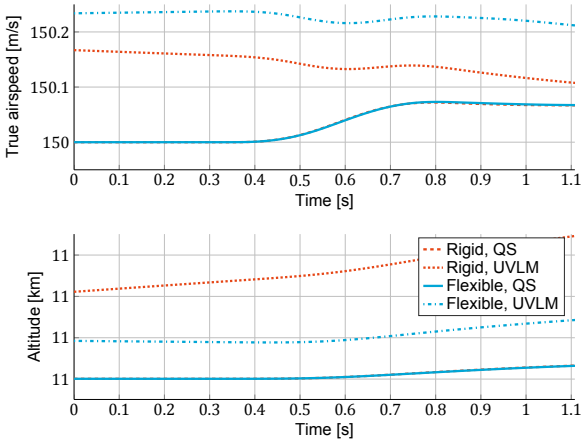

Figure C.11: The true airspeed V_∞ and altitude h for a gust of $H = 31$ m.

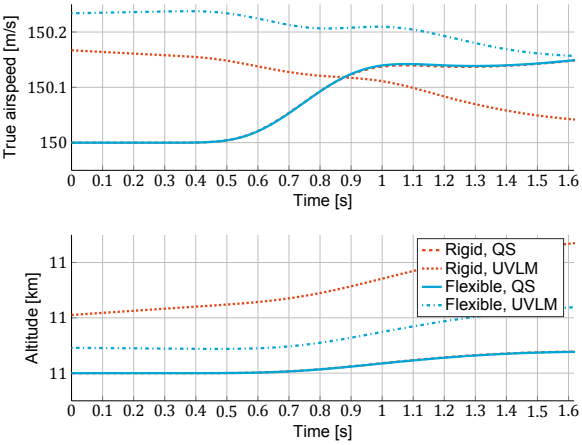

Figure C.12: The true airspeed V_∞ and altitude h for a gust of $H = 56$ m.

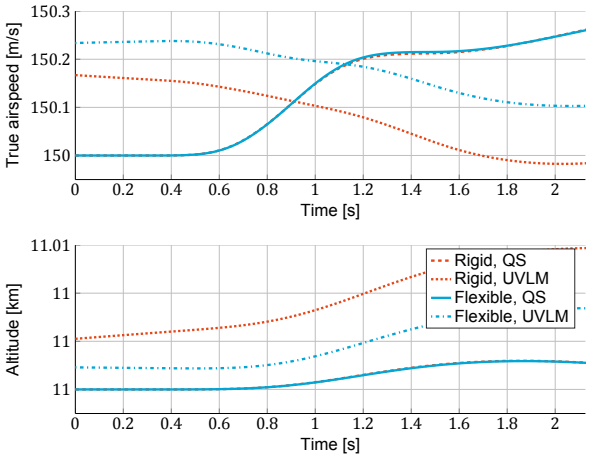

Figure C.13: The true airspeed V_∞ and altitude h for a gust of $H = 82$ m.

D

Wake shapes

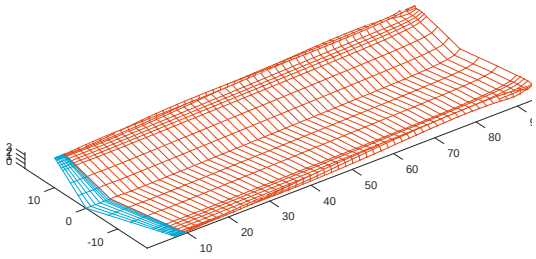

Figure D.1: The wake behind a wing flying straight and level at $\alpha = 2°$.

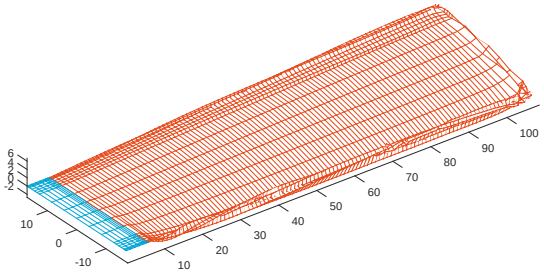

Figure D.2: The wake behind a wing rolling with $p = 10$ [deg/s].

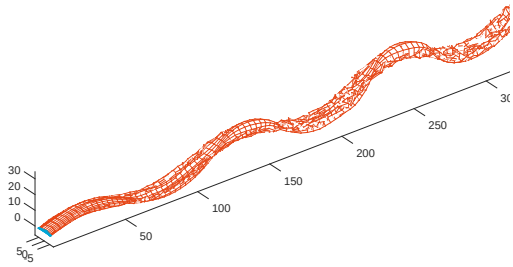

Figure D.3: The wake behind a wing plunging with $w = 10 \sin 2t$.

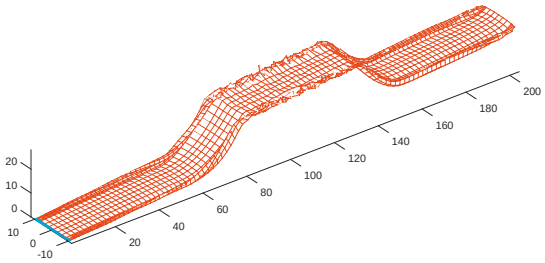

Figure D.4: The wake behind a wing undergoing a gust. The gust effect on the wake is cut off after displacing the wake 15 meters vertically.

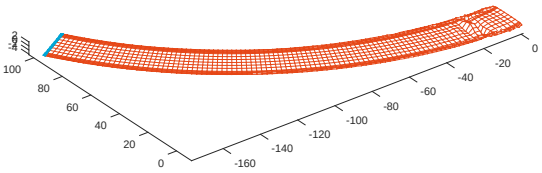

Figure D.5: The wake behind a wing yawing with $r = 10$ [deg/s], at $\alpha = 2°$.